ISSN: 1949-243X (Print), 1947-3818 (Online) Volume 2, Number 1, February 2010

Energy and Power Engineering

www.scirp.org/journal/epe

Scientific Research

Journal Editorial Board

ISSN: 1949-243X (Print) ISSN: 1947-3818 (Online)

http://www.scirp.org/journal/epe

Energy and Power Engineering, 2010, 1-72
http://www.scirp.org/journal/epe

Table of Contents

Energy and Power Engineering (EPE)

Journal Information

SUBSCRIPTIONS

Energy and Power Engineering (Online at Scientific Research Publishing, www.SciRP.org) is published quarterly by Scientific Research Publishing, Inc., USA.

E-mail: service@scirp.org

Subscription rates: Volume 2 2010

Print: $50 per copy.

Electronic: free, available on www.SciRP.org.

To subscribe, please contact Journals Subscriptions Department, E-mail: service@scirp.org

Sample copies: If you are interested in subscribing, you may obtain a free sample copy by contacting Scientific Research Publishing, Inc. at the above address.

SERVICES

Advertisements

Advertisement Sales Department, E-mail: service@scirp.org

Reprints (minimum quantity 100 copies)

Reprints Co-ordinator, Scientific Research Publishing, Inc., USA.

E-mail: service@scirp.org

COPYRIGHT

PRODUCTION INFORMATION

For manuscripts that have been accepted for publication, please contact:

E-mail: epe@scirp.org

Energy and Power Engineering, **2010, 1-5**
doi:10.4236/epe.2010.21001 Published Online February 2010 (http://www.scirp.org/journal/epe)

A Tabu Search Algorithm for Fast Restoration of Large Area Breakdown in Distribution Systems

Jian LIU, Hongli CHENG, Xiaojun SHI, Jingqiu XU
School of Electrical Engineering, Xi'an University of Science and Technology, Xi'an, China
Email: *edliu@bylink.com.cn, Chhl@xust.edu.cn*

Abstract: To restore the distribution systems in emergency states with the minimum load shedding, a novel Tabu search approach is put forward. The set of tripped switches is used as candidate solution. Some virtual tripped nodes are defined at the ends of the terminal nodes and by the source nodes. The neighborhood searching is committed by moving a tripped switch to the adjacent node of its upper stream and down stream, respectively. A Tabu list is formed for the tripped switches. The index is to energize as much as possible loads with as less as possible operated times. The electrical limitations and the voltage criterions are used as constrictions. The global aspiration criterion is adopted. An example is given, which shows that the proposed approach is feasible and can deal with complicated indexes.

Keywords: distribution systems, restoration, large area break down, load shedding, Tabu search

1. Introduction

Although many achievements have been made on fault isolation and restoration, most of them are for fault on a certain feeder section [1–5].

More serious faults, such as failure on a HV transmission line, a main transformer or a bus, may also occur and sometimes cause large area break down in the distribution systems.

Moreover, in some contingent situations of main transformer over loaded, bulk loads need to be transferred to the adjacent substations and sometimes load shedding is necessary, which is quit similar to the restoration process of large area break down.

A fast restoration approach of large area break down based on numerical optimization is put forward in [6]. Although it is smart, it can only deal with the simple index of the minimum load shedding.

In the practice, some other considerations are also needed to be included, such as the times of switching operation, losses, etc.

Tabu search is a promising evolutionary algorithm, which can deal with complicated indexes and constraints. It has been successfully applied into the distribution network reconfiguration [7].

But the conventional Tabu search based network reconfiguration approaches are not suitable to solve the problem of large area break down restoration with a few load shedding, because the numbers of tripped switches before and after reconfiguration must be equal.

In this paper, a novel Tabu search based approach is proposed to solve above problems.

2. Basic Principles

2.1 Construction of Solutions

In the Tabu search based distribution network reconfiguration, the set of tripped switches can be used as candidate solution.

The initial solution $\boldsymbol{s}^{(0)}$ based on the current topology of the distribution network is

$$\boldsymbol{s}^{(0)} = [s_1^{(0)}, s_2^{(0)}, ..., s_M^{(0)}] \tag{1}$$

where, $s_i^{(0)}$ is the sequence number of the i-th tripped switch of the current operation mode, M is the number of the tripped switches.

A candidate solution of the k-th iteration $\boldsymbol{s}^{(k)}$ is

$$\boldsymbol{s}^{(k)} = [s_1^{(k)}, s_2^{(k)}, ..., s_N^{(k)}] \tag{2}$$

If some loads are shed, we have

$$N > M \tag{3}$$

2.2 Virtual Tripped Nodes

In order to meet the requirement of $N>M$, we should define virtual tripped switches, which are shown in Figure 1.

The initial positions of virtual tripped switches are at the end of terminal nodes and behind the source nodes. The total number of virtual tripped switches is the summation of the number of terminal nodes and the number of the source nodes.

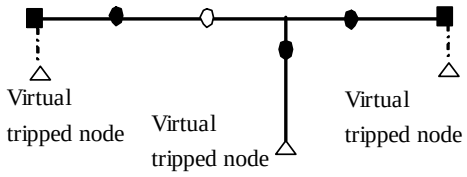

Figure 1. Illustration of virtual tripped switch-nodes

Actual tripped switches and virtual tripped switches are all called tripped switches. With the help of the virtual tripped switches, the Tabu search based distribution network reconfiguration approach can deal with the network reconfiguration problem with load shedding.

In the initial positions, the virtual tripped switches have no influence on the feeder as shown in Figure 1. But when their positions are shifted, some loads may be shed, which are shown in Figures 2(a), (d), (e) and (f). In Figure 2, the reenergized feeder sections are labeled with dotted lines.

2.3 Neighborhood Searching

In the iteration of Tabu search, the neighborhood searching is committed, in which, each tripped switch is moved to the adjacent node of its upper stream or down stream while the other switches keep their states not changed. Therefore, the candidate solution set is formed.

Assuming that the selected solution of the k-th iteration is shown in Figure 1, its candidate solutions of the k+1-th iteration produced by the neighborhood searching are shown in Figure 2.

The arrows in Figure 2 indicate the shifting direction of a certain tripped switch.

In each iteration, the best solution in the candidate solution set without being tabooed is taken as $\boldsymbol{s}^{(k+1)}$ and the corresponding newly tripped switch is taken into the Tabu list.

The global aspiration criterion is adopted, *i.e.*, once the best candidate in the candidate solution set is superior than the *'best so far'* solution, it is taken as $\boldsymbol{s}^{(k+1)}$ and the new *'best so far'* solution, no matter whether it is in tabooed state.

Above process is committed repeatedly until the stop criterion of no more improvement or reaching the maximum iteration times is satisfied.

2.4 Fitness Function

Complicated fitness functions, *i.e.*, indexes, can be used. As an example, a typical fitness function is

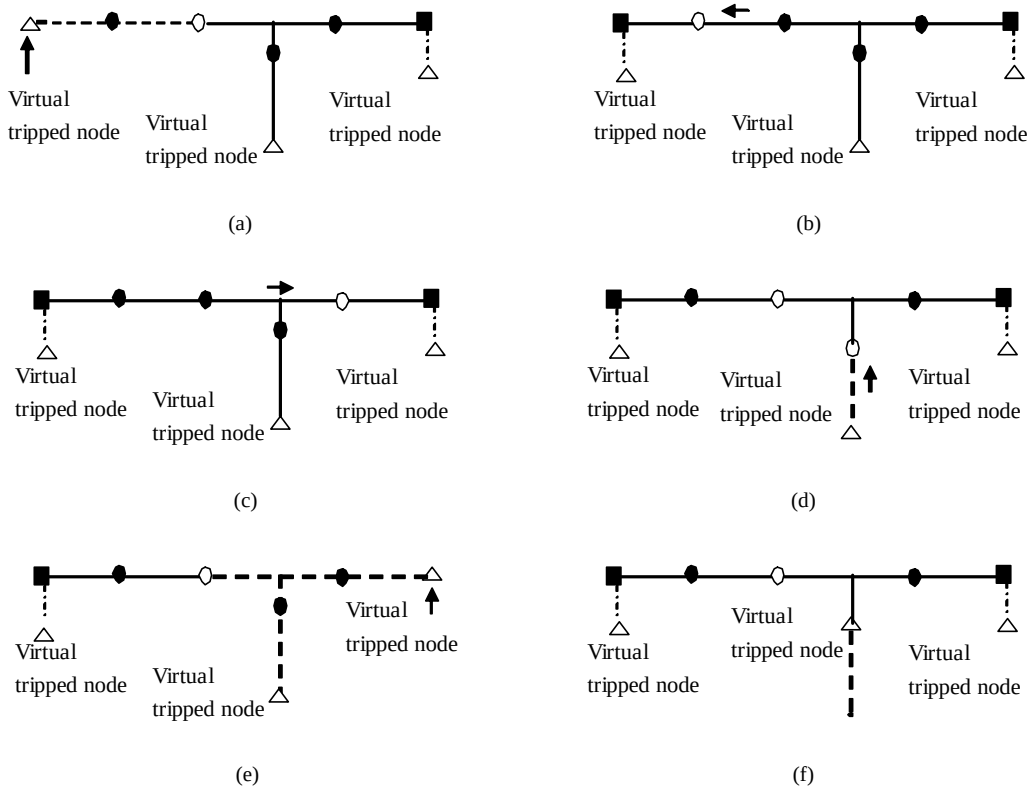

Figure 2. The candidate solutions

$$Max \quad f = \frac{\beta_1 \frac{\sum_{i\in\gamma} p_i}{P_\Sigma} - \beta_2 \frac{\Delta P}{\sum_{i\in\gamma} p_i}}{1+\beta_3 T} \tag{4}$$

where, P_Σ is the total load within the investigating area, γ is the set of energized sections after reconfiguration, $\sum_{i\in\gamma} p_i$ is the summation of the energized loads after reconfiguration, ΔP is the total line losses, T is the times of switching operation, β_1, β_2 and β_3 are weighted values.

The index of (4) indicates that it is encouraged to energize as much as possible loads with as less as possible operating times and line losses.

In most emergency states, the main task is to restore loads as much as possible without considering the line losses. But the difference of importance of various loads should be described in the index. Thus, the fitness function becomes

$$Max \quad f = \frac{\sum_{i\in\gamma} k_i p_i}{1+\beta_3 T} \tag{5}$$

where, k_i is the weight of the importance of the *i*-th load.

2.5 Constraints

Typical constraints are as follows:

-Topology constraints, *i.e.*, no loop exists.

-The times of switching operation should not exceed the maximum value allowed.

-Constraints of electrical limitations, *i.e.*, $I_i \le I_{i,\max}$ where, $I_{i,\max}$ is the current limitation of the *i*-th branch.

-Voltage constraints, *i.e.*, each node voltage is within the range of voltage criterions.

-Other constraints such as locking the switches connected to the malfunctioned buses and keep the switches in reparation in tripped states, etc.

2.6 Initial Solution

In contingent situations of main transformer over loaded, the current network topology can be used as the initial solution.

In emergency states due to faults, the steps to form the initial solution are as follows:

Step 1: Isolate of the deenergized buses by tripping all the switches connected to the corresponding buses and lock them in the tripped states, therefore, some feeder sections are deenergized.

Step 2: Close the loop switches (if exist) connecting the deenergized feeder sections to the healthy parts of the distribution network. If there are more than one restoration path for a certain deenergized feeder section, choose any one of them.

Step 3: Take the obtained topology as the initial solution.

2.6 Tabu Length and Stop Criterion

The ability of escaping from the local optimal points is improved with the Tabu length grows larger. But a larger Tabu length may hamper the convergence. As for a small-scale distribution network, it is possible to face the situation of no feasible candidate solution with a too large Tabu length. Therefore, the selection of Tabu length may be in accordance with the number of nodes of the distribution network. In most cases, it ranges from three to five.

The Tabu search based optimization process will terminate if the best solution remains the same within several successive iterations or the times of iteration reaches its maximum value set before hand.

2.7 Discussions

The optimal topology obtained by the above approach may contain redundant switching operations. As for the obtained optimal topology, if a certain switch is in tripped state and its adjacent feeder sections are all deenergized, the tripping operation of the switch is redundant and should be eliminated from the switching schedule.

The following measures may improve the efficiency of the proposed approach:

-Never locate any virtual tripped switch at the end of the feeder sections without sectionalizing switches.

-Only the feeders suffering from the failed apparatus and their corresponding connected parts [8] (In [8], a connected part is defined as a feeder group, in which, the load may be transferred from one feeder to the other) are included in the process of Tabu search.

-The Tabu search based optimization processes are performed in each connected part, respectively.

3. Case Study

The approach described in Section 2 will now be illustrated with results for Case Study based on a realistic distribution network shown in Figure 3.

There are two HV transmission line paths and three substations, such as, Sb.A, Sb.B and Sb.C and six main transformers labeled from No.1 Tr. to No.6 Tr. The voltage of primary distribution system is 10kV. There are six 10kV buses, such as B75, B79, B80, B84, B85 and B89.

The solid circles and the hollow indicate the closed and tripped switches, respectively. The numbers besides the circles are the sequence number of the corresponding nodes.

Assuming that the power factors of the loads are of the same value, the loads can be measured in Ampere. The

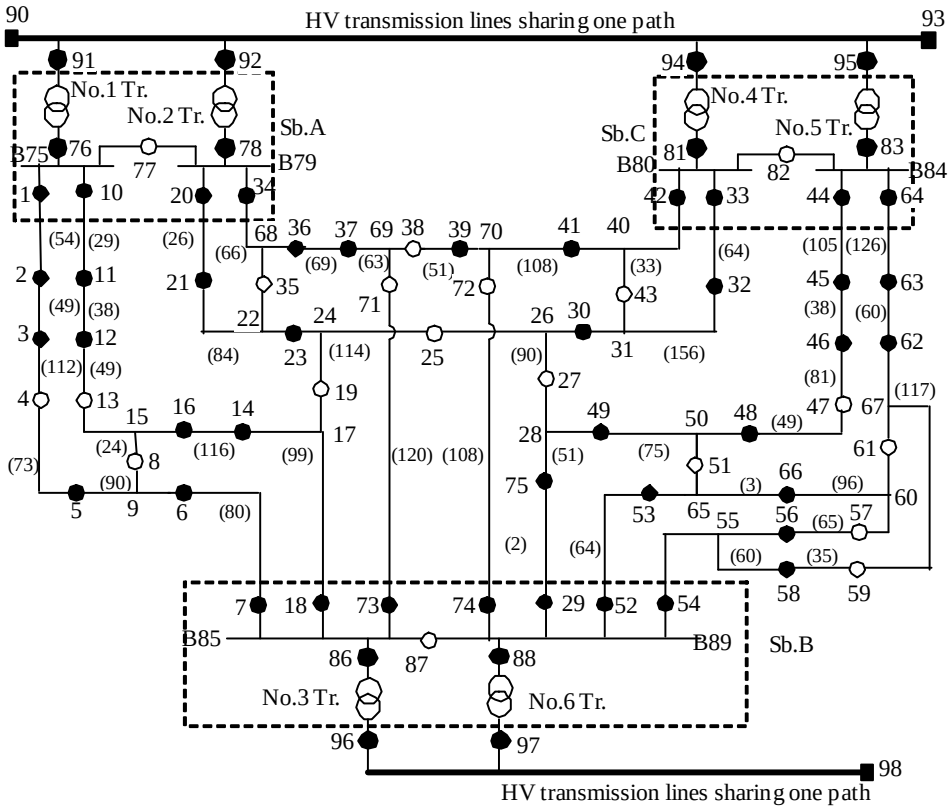

Figure 3. The candidate solutions

numerals in brackets illustrate the amount of loads supplied by the corresponding feeder sections. It can be seen from Figure 3 that the amount of loads is 2992(A) in the normal situation.

The electrical limitation of each main transformer and each bus is 1400(A). The electrical limitation of each feeder is 400(A).

The index is as the form of (5). The Tabu length is set a value of three.

Assuming that B89 fails and both B85 and B89 fail, the restoration schemes produced by the proposed approach are shown in Table 1 and Table 2, respectively.

It can be seen from Table 1 and Table 2 that the times of switching operation may be reduced by increasing the value of β_3 with a little decreasing of the amount of the energized loads, which shows the advantage of the proposed approach than [6].

Table 1. Restoration scheme in case of B89 fails

Switches tripped and locked out for isolation	β_3	Energized loads after restoration	Switching operation	Switching times
29,52,54,74,87	0.0	2768A	switches to trip: 49,53,66 switches to close: 27,47,51,61,72	8
	0.0015	2763A	switches to trip: 66,75 switches to close: 47,61,72	5

4. Conclusions

1) The way of defining virtual tripped nodes at the end of terminal nodes and by the source nodes is feasible to solve the problem of network reconfiguration with load shedding.

2) Complicated index containing small load shedding, less times of switching operation, lower losses , etc, may be dealt with in the proposed approach.

3) Based on the Distribution Automation System (DAS), the proposed approach is a powerful tool to realize fast restoration of large area break down of distribution systems. It is also useful for bulk loads transferring due to overload of transformers and reparation works.

5. Acknowledgement

The authors acknowledge the support of Mr. Zhu Y. Z., Mr. Xue H., Mr. Zhu Y. S. and Mr. Yuan B. for their disinterested support. The authors also esteem the Xi'an Power Supplying Company taking the lead in applying the proposed approach.

REFERENCES

[1] L. Seung-jae, L. Seng-ii and A. Bok-Shin, "Service res-

toration of primary distribution systems based on fuzzy evaluation of multi-criteria [J]," IEEE Transaction on Power Systems, Vol. 13, No. 3, pp. 1156–1163. 1998

[2] S. Curcic, C. S. Ozveren, and K. L. Lo, "Computer based strategy for the restoration problem in electric power distribution systems [J]," IEE Proceedings-Generation, Transmission, Distribution, Vol. 144, No. 5, pp. 389–398, 1997.

[3] J. Nahman and G. Strbac, "A new algorithm for service restoration in large-scale urban distribution systems," Electric Power System Research [J], No. 29, pp. 181–192, 1994.

[4] A. Augugliaro, L. Dusonchet, and E. Riva Sansevvrino, "Multi-objective service restoration in distribution networks using an evolutionary approach and fuzzy sets [J]," Electric Power and Energy Systems, No. 22, pp. 103–110, 2000.

[5] A. Pahwa, "Role of distribution automation in restoration of distribution systems after emergencies [C]," Proceedings of the IEEE Power Engineering Society Transmission and Distribution Conference, No. 1, pp. 737–738, 2007.

[6] J. Liu, J. Q. Xu, and H. L. Cheng, "Fast restoration of large area breakdown for power distribution systems [J]," Frontiers of Electrical and Electronic Engineering in China, No. 2, 2006.

[7] G. J. Chen, K. K. Li, and G. Q. Tang, "A Tabu search approach to distribution network reconfiguration for loss reduction [J]," Proceedings of the CSEE, Vol. 22, No. 10, pp. 28–33 (Ch), 2002.

[8] J. Liu, P. X. Bi, and H. P. Dong, "Simplified Analysis and Optimization for Complicated Distribution Systems [M]," China Electric Power Press, Beijing 2002.

Energy and Power Engineering, **2010, 6-9**
doi:10.4236/epe.2010.21002 Published Online February 2010 (http://www.scirp.org/journal/epe)

Gamma Ray Shielding from Saudi White Sand

Hefne JAMEEL, Al-Dayel OMAR, Al-horayess OKLA, Bagazi ALI, Al-Ajyan TURKI
King Abdulaziz City for Science and Technology, Riyadh, Kingdom of Saudi Arabia
Email: *oaldayel@kacst.edu.sa*

Abstract: This study is a comparison of gamma ray linear attenuation coefficient of two typs of shielding materials made of Saudi white and red sand. Each shield was consisted of one part of cement two parts of sand in addition to water. Different thicknesses were tested. The concentrations of all elements in each shield material were determined by Inductively Coupled Plasma Mass Spectrometer (ICP-MS). The results obtained from the ICP-MS were used in MCNP4B (Monte Carlo N-Particle Transport Computer Code System) [1] to calculate the attenuation coefficient. The theoretical (MCNP4B) and the experimental calculations were found to be in a good agreement. In the casw of the largest thickness used, 28cm, the gamma ray intensity passing through the white sand shield was approximately half of the intensity obtained through the red sand shield. The average linear attenuation coefficients were found to be 0.17cm^{-1} and 0.15cm^{-1} for white and red sand shields respectively. The study shows that white sand is better for attenuating gamma ray compared to the red sand.

Keywords: white & red sand, MCNP4B, ICP-MS, gamma ray, attenuation coefficient

1. Introduction

Gamma shielding is more effectively performed by materials with high atomic mass number and high density [2]. One such material is lead [3], which has a disadvantage of its low melting point. Iron is used for higher and lower energies. Iron is selected based on structural, temperature, and economic considerations. Water can be used but it is a poor absorber of gamma radiation, thus large amounts are required**.** Concrete is a good gamma attenuator as a general shield material. Concrete is strong, inexpensive, and adaptable to different types of construction.

The major objective of this work is to compare the gamma ray shields made of Saudi red and white sand. Saudi Arabia has a huge amount of these two kinds of sand. The white sand concrete is much better in all characteristics than the red one. An extensive study has documented that the white sand blocks is harder than red sand blocks [4].

It is one of our national issues to look into the possible improvement in gamma attenuation by using the white sand concrete to extend the commercial values of this kind of sand.

2. Shielding Preparation

Two kinds of shielding materials made of Saudi white and red sand. Each shield was consisted in two parts of sand to one parts of cement in addition to water. In order to obtain good workability and allow development of the maximum strength possible, the shielding ingredients must be thoroughly mixed. The mixing was done by machine. A typical mixer (a paddle mixer with tilting drum) was used. Mixing time was around five minutes. A shorter mixing time may result in nonuniformity, poor workability, low water retention and less desired air content. A too long mixing time may adversely affect the air content of shield made with air-entraining cement [5]. A 30x30 cm molds were made of plastic with different heights (thicknesses). Different thicknesses were made 4, 8 and 16cm. Using these three shielding, different thicknesses were tested 4, 8, 12(4+8), 16, 20(4+16), 24(8+16) and 28(4+8+16) cm.

3. Experiment Setup

The experiment was arranged as shown in Figure 1, where the studying shield was mounted in the middle of distance between the gamma source and the detector. The gamma radiation emitted from the source (^{137}Cs with activity around 102 mCi) was collimated using lead blocks so that the radiation beam was guided to the detector through about 55cm^2 windows in the lead shield.

The distances between the source, the detector and the studying shield were selected so that the dead time of the detector was in the range of 0.52 to 3.58%.

The attenuation coefficient was calculated using the relation:

$$I = I_0 e^{-\mu x}$$

where: I is the measured attenuated gamma ray intensity, I_o is measured initial intensity (no studying shield), μ is attenuation coefficient factor and x is the shield thickness.

The gamma ray spectrum was acquired for a real time of 420 sec for each measurement which was reasonably enough to obtain a good pulse height distribution. Counts under the peak (0.661 Mev) spectrum area were used to calculate the attenuation coefficient factor of both studying shields (see Table 1).

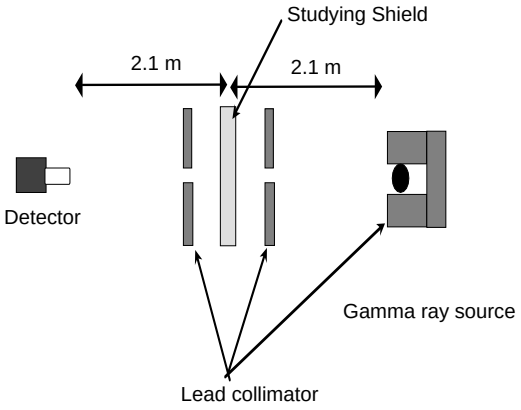

Figure 1. Experiment setup

Table 1. The counts rate obtained from the experiment

RED Shield				
Thick. (cm)	Area under the peak (R1)	Area under the peak (R2)	Average (R1+R2)/2	Coeff
0	244757	245089	244923	
4	136996	136771	136883.5	0.145
8	74181	74230	74205.5	0.1493
12	41793	41728	41760.5	0.1474
16	22764	22307	22535.5	0.1491
20	12592	12643	12617.5	0.1483
24	6846	6893	6869.5	0.1489
28	3857	3824	3840.5	0.1484
Attenuation Coefficient Average				0.1481
White Shield				
0	244757	245089	244923	
4	121246	120933	121089.5	0.1761
8	65292	65431	65361.5	0.1651
12	32166	32318	32242	0.169
16	17249	17144	17196.5	0.1660
20	8526	8602	8564	0.1677
24	4463	4464	4463.5	0.1669
28	2157	2277	2217	0.1680
Attenuation Coefficient Average				0.1685

4. Theoretically

A simulation of the experiment was done using MCNP4B. The geometry was described as shown in Figure 1. The source was described as a point source ^{137}Cs with one energy 0.661 Mev. The source was assumed as an isotropic. Point detectors were used to find out the gamma intensity at the detector window.

Samples from the studying shield were tested to measure the densities (see Table 2), and to find out the concentrations of the elements in the studying shield materials. ICP-MS was used to find the concentrations of the elements in the white and red shield materials.

5. Use of ICP-MS for Elemental Determination of the Studying Shield

Accurately weighed portion (0.2–0.3g) of the dried sample was transferred to a TEFLON digestion tube (120mL) and 10.0 mL of the acid mixture (HNO_3/HF/HCl, 3:1:1) was introduced. The tube was sealed and the sample was digested inside a microwave oven (Milestone ETHOS 1600) following a heating program shown in Table 3. After being cooled to ambient temperature, the tube was opened; the inside of the lid was rinsed with distilled and de-ionized water (DIW) and the mixture heated on a hotplate (120℃) for 30 min. to drive off HF and HCl. The resulting digest was filtered in a graduated plastic tube using 1% HNO_3 for washing and made up to 30.0mL mark. For ICP-MS measurement the clear digest so obtained was diluted 10 times incorporating 10 μgL^{-1} solution of ^{103}Rh. In general, samples were prepared in a batch of six including a blank (HNO_3/HF/HCl) digest [6–8].

Table 2. Density measurements for both shields materials

Red		
Weight gm	Volume cm^3	Density g/ cm^3
15.6493	8	1.9561625
11.7517	6	1.958616667
19.7258	10	1.97258
Average		1.962453056
White		
Weight gm	Volume cm^3	Density g/ cm^3
18.3513	8.5	2.158976471
12.1144	6	2.019066667
11.1688	5	2.23376
Average		2.137267712

Table 3. Microwave heating program used for dissolution of the concrete samples

Step	1	2	3	4
Power (W)	250	400	650	250
Time (min)	10	10	10	10

High purity water (DIW) (Specific resistivity 18 MΩ. cm^{-1}) obtained from a Millipore Milli-Q water purification system was used throughout the work. HNO_3, HF and HCl used for sample digestion were of Suprapure® grade with certified impurity contents were purchased from Merck, Germany. A multi-element standard (Merck -VI) containing 30 elements with certified concentration values or laboratory made multi-element standard (6-elements) was used as the external standard during ICP-MS measurements. The Standard Reference Material (SRM), IAEA-SOIL-7 was purchased from the International Atomic Energy Agency, Vienna. It was used for quality assurance conformation.

The analysis is performed by a Perkin-Elmer Sciex Instruments multi-element ICP-MS spectrometer, type ELAN6100, equipped with a standard torch, cross flow nebulizer and Ni sampler and skimmer cones.

The ELAN provides a unique semi quantitative method called Total Quant. This technique enables one to determine the concentration of up to 81 elements in a sample in a single measurement. Determination can be performed without using a series of standards, the use of standards is recommended to adjust the ELAN for improved accuracy. Calibration is achieved using just a few elements distributed throughout the mass range of interest. The calibration process is used to update internal response data that correlates measured ion intensities to the concentrations of elements in a solution. In this work a multi elements standards supplied by Perkin-Elmer was used to calibrate the system. The semi quantitative analysis results of the white shield and the read shield are shown in Table 4.

The moisture content of the white sand shield and the read sand shield was measured using moisture analyzer MA50 system from Sartorius. It was found to be 2.4% and 1.95% respectively.

6. Results and Discussion

The MCNP4B was run for enough time to approach an error less than 5%. A waiting factor, which equal to one, was used in the MCNP4B. The output of MCNP4B and the results from the measurements were shown in Table 5. Figure 2 shows the count rate vies shielding thickness for both types of shielding made from red and white sand, experimentally and theoretically.

The attenuation coefficient for the two kinds of shielding were calculated and then plotted as a function of the shield thickness for each case. (See Figure 3).

The results show a clear improvement in the gamma attenuation coefficient in the case of white sand.

During the preparation of the shield it was observed that water is floated on the surface of the red shield mold. Also from the moisture measurements, it was found that

Table 4. Elemental composition of red sand shield and white sand shield

Ele.	White shield %	Red shield %	Ele	White shield %	Red shield %
C	0.002	0.003	Cr	0.002	0.001
Na	0.0467	0.053	Mn	0.008	0.007
Mg	0.094	0.087	Fe	0.329	0.316
Al	0.239	0.12	Sr	0.025	0.017
S	0.101	0.056	Ba	0.003	0.003
K	0.173	0.221	Ce	3.344	1.006
Ca	4.33	2.179	H	0.371	0.317
Ti	0.002	0.001	O	49.88	52.17
V	0.003	0.002	Si	41.05	43.44

Table 5. The attenuation coefficients for both red and white shield

Thick. (cm)	Peak area	MCNP4B	Attenuation	
			Meas.	MCNP
Red				
0	244923	1.96E-07		
4	136883.5	1.04E-07	0.1455	0.1596
8	74205.5	5.52E-08	0.1493	0.1584
12	41760.5	2.95E-08	0.1474	0.1579
16	22535.5	1.59E-08	0.1491	0.1572
20	12617.5	8.50E-09	0.1483	0.1569
24	6869.5	4.62E-09	0.1489	0.1562
28	3840.5	2.50E-09	0.1484	0.1558
Ave.			0.1481	0.1574
White				
0	244923	1.96E-07		
4	121089.5	9.81E-08	0.1761	0.1733
8	65361.5	4.97E-08	0.1651	0.1717
12	32242	2.52E-08	0.169	0.1709
16	17196.5	1.29E-08	0.166	0.1703
20	8564	6.55E-09	0.1677	0.1699
24	4463.5	3.43E-09	0.1669	0.1687
28	2217	1.74E-09	0.168	0.1688
Ave.			0.1684	0.1705

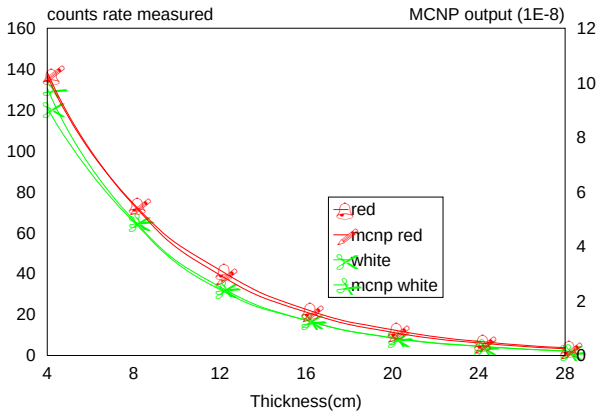

Figure 2. The obtained count rates experimentally and theoretically.

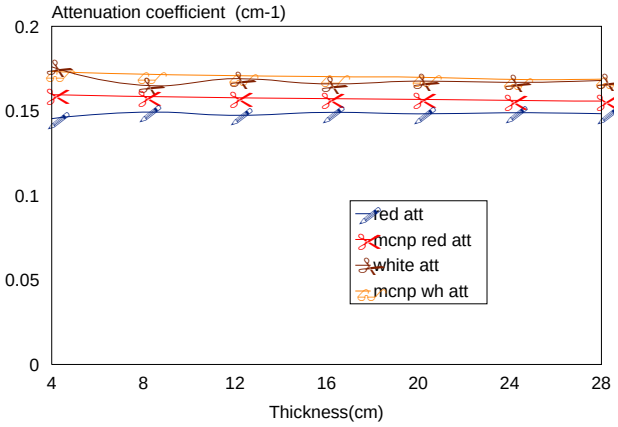

Figure 3. The calculated attenuation coefficients experimentally and theoretically

the white sand shield is higher than the red sand shield on moisture contents; this mean water was absorbed more in the white sand than in the red sand. More water causes the increasing of the reaction between the cement and the sand, and reducing the temperature, which reduce the amount of cracking inside the shield [5]. This causes the shield solidity. This may explain the improvement of the gamma attenuation coefficient of the white shield [9].

The theoretical (MCNP) and the experimental calculation were found to be in good agreement. At the largest thickness, 28cm, the gamma ray intensity passing through the white sand shield was approximately half of the intensity obtained in the case of the red sand shield. The average linear attenuation coefficient for the shield made of white sand is $0.17cm^{-1}$ and that from red sand is $0.15cm^{-1}$.

7. Conclusions

The study concludes that white sand is better for attenuating gamma ray compared to the red sand especially for large thickness.

The theoretical (MCNP) and the experimental calculation were in good agreement with each other.

We recommended using the white sand in the concrete shield to attenuate gamma ray.

REFERENCES

[1] RSICC Computer Code Collection, "CCC-660 Monte Carlo N-Particle Transport code system".

[2] R. Nunez-Lagos and A. Virto, Applied Radiation and Isotopes, Vol. 47, No. 9–10, pp. 1011, 1996.

[3] G. Braoudakis, *et al*., Nuclear Instruments and Methods, Vol. A, No. 403, pp. 449, 1998.

[4] M. Amin, O. Alharby, A. Alabdulaly, A. Alsary, S. Alsid, and M. Edres, "The properties and application of white sand in Riyadh area, report," KACST, 1997.

[5] R. C. Smith, T. L. Honkala, and C. K. Andres, Masonry: Materials Design Construction, 1979.

[6] R. Faciani, E. Novare, M. Marchesini ,and M. Gucciardi, "Multi-element analysis of soil and sediment by ICP- MS after a microwave assisted digestion method," J. Anal. At. Spectroscopy, No. 15, pp. 561–565, 2000.

[7] V. Balaram, "Characterization of trace elements in environmental samples by ICP-MS," AT. Spectroscopy, No. 14, pp. 174–179, 1993.

[8] J. Szakova, P. Tlustos, J. Balik, D. Pavlikova, and V. Vanek, "The sequential analytical procedure as a tool for evaluation of As, Cd and Zn mobility in soil," Fresenius, Journal of Analytical Chemistry, No. 363, pp. 594–595 1999.

[9] A. El-Sayed, "Calculation of cross-section for fast neutrons and gamma-rays in concrete shields," Journal Annals of Nuclear Energy, Vol. 29, No. 16, 1977–1988, 2002.

Energy and Power Engineering, 2010, 10-17
doi:10.4236/epe.2010.21003 Published Online February 2010 (http://www.scirp.org/journal/epe)

Three-Level Five-Phase Space Vector PWM Inverter for a Two Five-Phase Series Connected Induction Machine Drive

N. R. ABJADI[1], J. SOLTANI[2], J. ASKARI[2], Gh. R. Arab MARKADEH[1]
[1]*Department of Engineering, Shahrekord University, Shahrekord, Iran*
[2]*Department of Electrical and Computer Engineering, Isfahan University of Technology, Isfahan, Iran*
Email: *navidabjadi@yahoo.com*

Abstract: This paper describes the decoupled torque and flux control of a two series connected five-phase Induction Machine (IM) drive that is supplied by a three-level five phase SVPWM inverter, using a well known phase transposition in the series connection. At the first, the decoupled torque and flux controller is developed based on variable-structure control (VSC). Then, a sliding-mode (SM) flux observer in employed to estimate the stator flux; that uses a two reference frames which result in eliminating the speed adaptation. Moreover simple control strategy is introduced for three-level SVPWM voltage source inverter (VSI) that can be easily implemented in practice for a two-series five phase IM drive. Finally, the effectiveness and capability of the proposed control method is verified by computer simulation.

Keywords: multiphase systems, multilevel VSI, sliding mode control

1. Introduction

In electrical drive applications, three-phase drives are widely used for their convenience. However, high-phase number drives possess several advantages over conventional three-phase drives such as: reducing the amplitude and increasing the frequency of torque pulsations, reducing the rotor harmonic currents, reducing the current per phase without increasing the voltage per phase, and lowering the dc-link current harmonics and higher reliability. By increasing the number of phases, it is also possible to increase the torque per rms ampere for the same volume machine [1].

Multi-phase machines have found wide applications in transport, textile manufacturing and aerospace since few years [2–14]. The recent research works on multi-phase machines can be categorized into multi-phase pulse width modulation (PWM) techniques for multi-phase machines [2–14], harmonic injection to produce more torque and to achieve better stability [5], fault tolerant issues of multi-phase motor drives [6], series/parallel connected multi-phase machines [7–14].

Applications involving high power may require multiphase systems, in order to reduce stress on the switching devices. There are two approaches to supplying high power systems; one approach is the use of multilevel inverters supplying three-phase machines and the other approach is multileg inverters supplying multiphase machines. Much more work has been done on multilevel inverters. It is interesting to note the similarity in switching schemes between the two approaches: for the multilevel inverter the additional switching devices increase the number of voltage levels, while for the multileg inverter, the additional number of switching devices increases the number of phases [15].

In [16], Kelly *et al*. also verified that an n-phase space vector PWM (SVPWM) scheme can be described in terms of the applying times of available switching vectors on the basis of the space vector concept. However, the paper only focuses on how to realize a sinusoidal phase voltage. As is widely known, most multiphase motors are designed to have the nonsinusoidal back-EMF voltage.

Hamid A. Toliyat have made much research on control method and running performance aim at five-phase drive [1], but their subject investigated is the system feeding with two level inverter. Another research work has been done in [17] on a multiphase two level nonsinusoidal SVPWM.

The power rating of the converter should meet the required level for the machine and driven load. However, the converter ratings can not be increased over a certain range due to the limitation on the power rating of semiconductor devices. One solution to this problem is

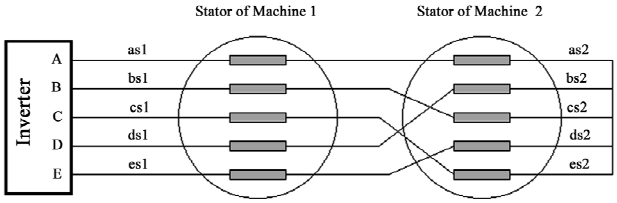

Figure 1. Two five-phase machine drive supplied by a single inverter

using multi-level inverter where switches of reduced rating are employed to develop high power level converters. The advent of inverter fed motor drives also removed the limits of the number of motor phases. This fact made it possible to design machine with more than three phases and brought about the increasing investigation and applications of multi-phase motor drives [18,19].

In [20], Qingguo Song, introduced a method to supply a single five-phase permanent magnetism synchronous motor (PMSM) with a three level SVPWM VSI. But the method is not capable to control more series connected multiphase machines or producing nonsinusoidal voltages.

Space-vector modulation (SVM) is an advanced technique for the generation of output voltages or currents in inverters based on the spatial visualization of their variables. In the conventional approach of this technique, the inverter is understood as a whole, allowing full control over the switching sequences of the switches and achieving maximum use of the dc-link voltage.

The five-phase induction motor drives have many more space voltage vectors than the three-phase induction motor drives. The increased number of vectors allows the generation of a more elaborate switching vector table in which the selection of the voltage vectors is made based on the real-time values of the stator flux and torque variations.

In this paper, a five-phase 3 level SVPWM algorithm is developed to control a two series IM drive system. Recognizing the VSC merits and the advantages of using the SVM, this paper presents a VSC-DTC solution for series-connected induction motor drives. Direct torque and flux control is achieved by means of VSC.

2. Description and Modeling of the Drive System

The drive consists of two five-phase squirrel cage induction machines. Referring to Figure 1 the five-phase stator windings of the two machines are connected in series, with an appropriate phase transposition [19]. The two-motor drive system is supplied from a single five-phase VSI.

From Figure 1 the relationship between voltage and currents are given as:

$$\begin{aligned} v_A &= v_{as1} + v_{as2} & i_A &= i_{as1} = i_{as2} \\ v_B &= v_{bs1} + v_{cs2} & i_B &= i_{bs1} = i_{cs2} \\ v_C &= v_{cs1} + v_{es2} & i_C &= i_{cs1} = i_{es2} \\ v_D &= v_{ds1} + v_{bs2} & i_D &= i_{ds1} = i_{bs2} \\ v_E &= v_{es1} + v_{ds2} & i_E &= i_{es1} = i_{ds2} \end{aligned} \quad (1)$$

Each machine is supposed to have its own parameters. Using the decoupling Clark's transformation, the original phase variables are correlated to new ($\alpha-\beta$) variable as $f_{\alpha\beta} = C f_{abcde}$, where C is the power-invariant transformation matrix:

$$C = \sqrt{\frac{2}{5}} \begin{matrix} \alpha \\ \beta \\ x \\ y \\ 0 \end{matrix} \begin{bmatrix} 1 & \cos\alpha & \cos 2\alpha & \cos 3\alpha & \cos 4\alpha \\ 0 & \sin\alpha & \sin 2\alpha & \sin 3\alpha & \sin 4\alpha \\ 1 & \cos 2\alpha & \cos 4\alpha & \cos 6\alpha & \cos 8\alpha \\ 0 & \sin 2\alpha & \sin 4\alpha & \sin 6\alpha & \sin 8\alpha \\ 1/\sqrt{2} & 1/\sqrt{2} & 1/\sqrt{2} & 1/\sqrt{2} & 1/\sqrt{2} \end{bmatrix} \quad (2)$$

The (α, β) and (x, y) voltages and currents of the five-phase VSI are obtained as:

$$\begin{bmatrix} v_\alpha^{INV} \\ v_\beta^{INV} \\ v_x^{INV} \\ v_y^{INV} \\ v_0^{INV} \end{bmatrix} = C \begin{bmatrix} v_A \\ v_B \\ v_C \\ v_D \\ v_E \end{bmatrix} = C \begin{bmatrix} v_{as1} + v_{as2} \\ v_{bs1} + v_{cs2} \\ v_{cs1} + v_{es2} \\ v_{ds1} + v_{bs2} \\ v_{es1} + v_{ds2} \end{bmatrix} = \begin{bmatrix} v_{\alpha s1} + v_{xs2} \\ v_{\beta s1} - v_{ys2} \\ v_{xs1} + v_{\alpha s2} \\ v_{ys1} + v_{\beta s2} \\ 0 \end{bmatrix} \quad (3)$$

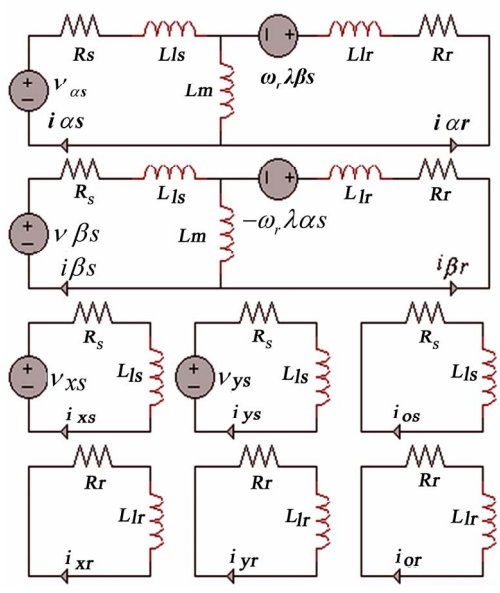

Figure 2. Five-phase IM equivalent circuits of one machine

$$\begin{aligned} i_{\alpha}^{INV} &= i_{\alpha s1} = i_{xs2} \\ i_{\beta}^{INV} &= i_{\beta s1} = -i_{ys2} \\ i_{x}^{INV} &= i_{xs1} = i_{\alpha s2} \\ i_{y}^{INV} &= i_{ys1} = i_{\beta s2} \end{aligned} \tag{4}$$

The torque equations of the two series-connected machines are given as follow

$$T_{ek} = P_k L_{mk}(i_{\alpha rk} i_{\beta sk} - i_{\beta rk} i_{\alpha sk}) \tag{5}$$

here k=1,2 and P_k are pole pairs.

From these equations and (4), one can note that the torque production currents of the first motor ($i_{\alpha s1}, i_{\beta s1}$) are equal to none producing torque currents of the second motor (i_{xs2}, i_{ys2}). As a result, the two motors can be controlled independently through a single VSI.

The stator voltage equations of each machine are

$$\begin{aligned} v_{\alpha sk} &= R_{sk} i_{\alpha sk} + \frac{d}{dt}(L_{sk} i_{\alpha sk} + L_{mk} i_{\alpha rk}) \\ v_{\beta sk} &= R_{sk} i_{\beta sk} + \frac{d}{dt}(L_{sk} i_{\beta sk} + L_{mk} i_{\beta rk}) \\ v_{xsk} &= R_{sk} i_{xsk} + \frac{d}{dt}(L_{lsk} i_{xsk}) \\ v_{ysk} &= R_{sk} i_{ysk} + \frac{d}{dt}(L_{lsk} i_{ysk}) \end{aligned} \tag{6}$$

where k=1,2.

The rotor voltage equations of each machine are

$$\begin{aligned} 0 &= R_{rk} i_{\alpha rk} + \omega_{r1}(L_{rk} i_{\beta rk} + L_{mk} i_{\beta sk}) + \\ &\quad \frac{d}{dt}(L_{rk} i_{\alpha rk} + L_{mk} i_{\alpha sk}) \\ 0 &= R_{rk} i_{\beta rk} - \omega_{rk}(L_{rk} i_{\alpha rk} + L_{mk} i_{\alpha sk}) + \\ &\quad \frac{d}{dt}(L_{rk} i_{\beta rk} + L_{mk} i_{\beta sk}) \end{aligned} \tag{7}$$

where k=1,2.

In Figure 2 the five-phase IM equivalent circuits of one machine is shown.

3. Sliding-Mode Controller

Block diagram of the variable-structure direct torque controlled drive (VSC-DTC) under consideration is shown in Figure 3. As can be seen from this figure, for each motor the control quantities are the stator flux magnitude and torque.

A reference stator voltage, $v_s^* = v_{ds}^* + j v_{qs}^*$, is obtained at the output of the VSC, where v_{ds}^* is generated by the flux control law and v_{qs}^* by the torque control law. The

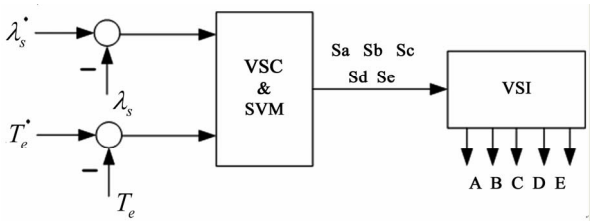

Figure 3. Block diagram of the VSC-DTC

control law is of the "Relays with constant gains" type [21],

$$v_{ds}^* = (K_{P\lambda} + K_{I\lambda}\frac{1}{s})\mathrm{sgn}(S_d) \tag{8}$$

$$v_{qs}^* = (K_{PT} + K_{IT}\frac{1}{s})\mathrm{sgn}(S_q) + \hat{\omega}_{\lambda_s}\hat{\lambda}_s \tag{9}$$

where $s=d/dt$, sgn is the signum function, $K_{P\lambda}$, $K_{I\lambda}$, K_{PT} and K_{IT} are the PI controller gains, $S = S_d + jS_q$ is the sliding surface, and superscript " ^ " stands for estimated quantities. In order to accelerate the voltage response during speed transients, the torque control law contains a feedforward compensation for the dynamic electromotive force (EMF). The PI controllers help to reduce the chattering associated with VSC and define the system's behavior when it is not in the sliding mode (during the reaching phase). The sliding surface is designed so as to enforce SM operation with first-order dynamics,

$$S = S_d + jS_q = e_{\lambda_s} + c_{\lambda_s} s e_{\lambda_s} + j(e_{T_e} + c_{T_e} s e_{T_e}) \tag{10}$$

where $e_{\lambda_s} = \lambda_s^* - \hat{\lambda}_s$ and $e_{T_e} = T_e^* - \hat{T}_e$; c_{λ_s} and c_{T_e} are design constants.

In the sliding mode, the control law (8) and (9) restrict the system state onto the surface , and its behavior is exclusively governed by $S = 0$ [21].

4. Sliding-Mode Observer

In [21,22], an inherently sensorless SM observer has been developed. It uses two reference frames allows eliminating the speed adaptation. This feature is significant in drives that do not need the speed estimation for control (torque-controlled drives) and it is expected to produce better results than conventional observers.

An SM observer for IM is

$$\frac{d}{dt}\hat{\underline{\lambda}}_s = -R_s \underline{i}_s - j\omega_e \hat{\underline{\lambda}}_s + \underline{v}_s + K_1 \mathrm{sgn}(\underline{i}_s - \hat{\underline{i}}_s) \tag{11}$$

$$\begin{aligned} \frac{d}{dt}\hat{\underline{\lambda}}_r = &-\frac{L_m}{L_s T_r \sigma}\hat{\underline{\lambda}}_s - (\frac{1}{T_r \sigma} + j(\omega_e - \omega_r))\hat{\underline{\lambda}}_r + \\ &K_2 \mathrm{sgn}(\underline{i}_s - \hat{\underline{i}}_s) \end{aligned} \tag{12}$$

$$\underline{i}_s = \frac{L_r \hat{\underline{\lambda}}_s - L_m \hat{\underline{\lambda}}_r}{L_\sigma^2} \tag{13}$$

In order to eliminate the rotor speed adaptation, the stator Equation (11) is implemented in stator reference

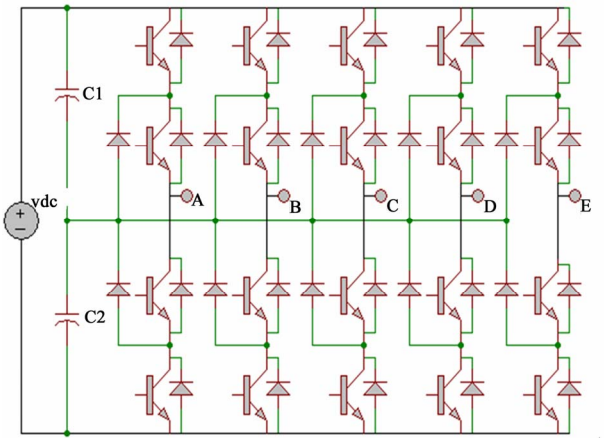

Figure 4. Scheme of a five-phase three-level inverter

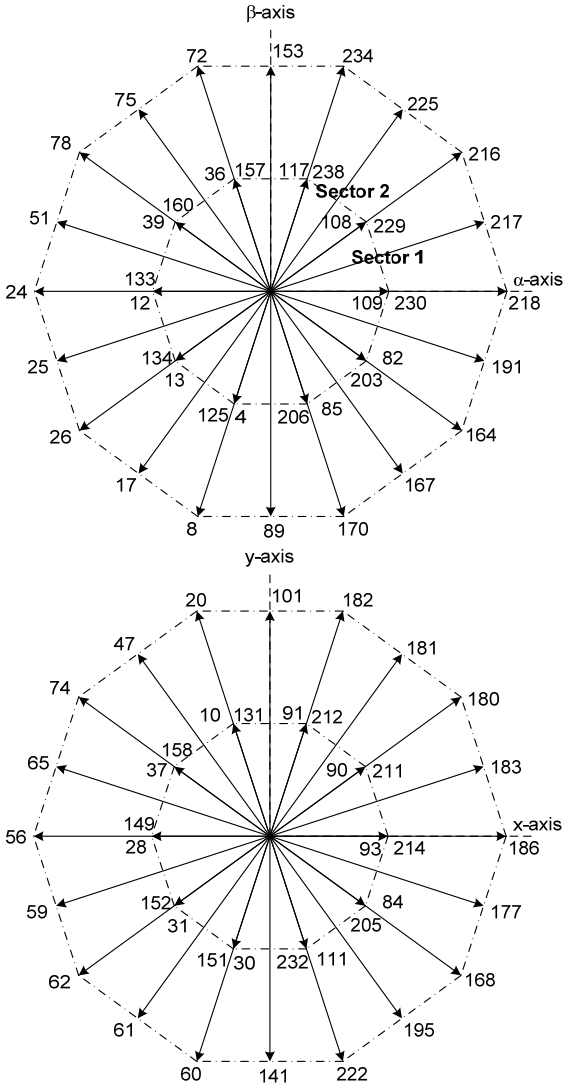

Figure 5. The switching vectors on α-β and x-y planes

frame, and the rotor Equation (12) is implemented in rotor flux frame (superscript " *r* "), which rotates with rotor flux speed, ω_{λ_r}

$$\frac{d}{dt}\hat{\underline{\lambda}}_s = -R_s\underline{i}_s + \underline{v}_s + K_1\,\mathrm{sgn}(\underline{i}_s - \hat{\underline{i}}_s) \tag{14}$$

$$\frac{d}{dt}\hat{\underline{\lambda}}_r^r = -\frac{L_m}{L_s T_r \sigma}\hat{\underline{\lambda}}_s^r - \left(\frac{1}{T_r\sigma} + j(\omega_{\lambda_r} - \omega_r)\right)\hat{\underline{\lambda}}_r^r + K_2\,\mathrm{sgn}(\underline{i}_s^r - \hat{\underline{i}}_s^r) \tag{15}$$

Taking into consideration that the rotor flux is aligned with the reference frame, the rotor model (15) turns out to be simple:

$$\frac{d}{dt}\hat{\lambda}_{dr}^r = \frac{L_m}{L_s T_r \sigma}\hat{\lambda}_{ds}^r - \frac{1}{T_r\sigma}\hat{\lambda}_{dr}^r + \Re e(K_2\,\mathrm{sgn}(\underline{i}_s^r - \hat{\underline{i}}_s^r)) \tag{16}$$

$$\hat{\lambda}_{qr}^r = 0 \tag{17}$$

It can be shown that the observer is stable if its gains are large enough [21].

5. Three Level Space Vector Pwm

In [20], a technique of vector space control of three-level voltage source inverter fed five-phase machines was presented.

Using the same idea described in [20], in this paper a SVPWM voltage source is developed which is capable of supplying the two motor drive system with different rotor speeds. The SVPWM scheme is designed to generate an arbitrary reference voltage space vector which constitutes the motors main frequencies ω_1 and ω_2.

Figure 4 shows the scheme of a five-phase three-level inverter. There are $243(3^5)$ voltage vectors; the magnitude and distributing of voltage vectors are far more complex than five-phase two-level inverter. However, not all of vectors are suitable to vector synthesizing.

Consider voltage vectors with magnitude $V_L = 0.6472V_{DC}$, $V_M = 0.6156V_{DC}$, $V_S = 0.3236V_{DC}$ and zero voltage vectors as efficient working vectors. There are 43 efficient vectors in each plane, including 30 non-zero vectors, 10 redundant and 3 zero vectors, as shown in Figure 5.

The decimal numbers in Figure 5 denote the switching modes. When each decimal number is converted to a five digit number in base 3, the 2's in this number indicate that the two upper switches in the corresponding switching arms are "on" and the 1's in this number indicate that the two middle switches are "on", while the 0's indicate the "on" state of the lower switches. The MSB (most significant bit) of the number represents the switching state of phase a, the second MSB for phase b, and so on. As shown in Figure 5, selected working voltage vectors equally divide the decagon into ten sections 1, 2, ..., 10.

From the average vector concept during one sampling

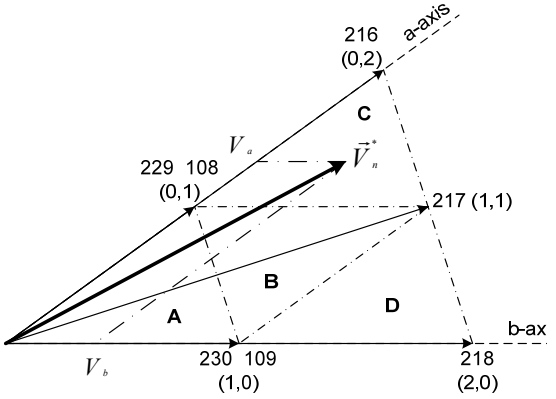

Figure 6. Reference vector and switching vectors in section 1 of α-β plane

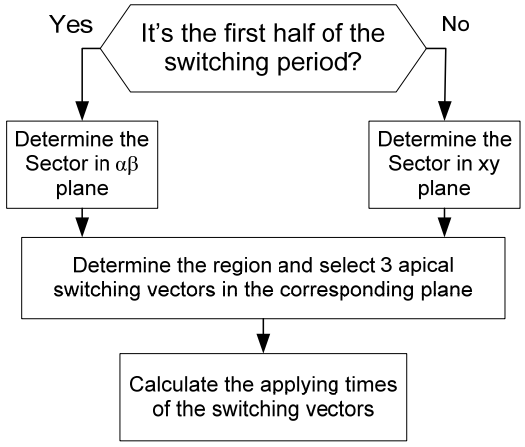

Figure 7. Flowchart to realize reference voltage vectors

period, the reference voltage vectors on the α-β and x-y planes can be realized by adjusting the applying times of 3 vectors. Figure 6 shows each section can be divided into four smaller triangle regions, and the reference voltage vector is formed by three apical voltage vectors in this triangle [20]. For example if the reference vector is between vectors 218 and 216 in α-β plane (sector 1), and moreover it is located in region C, as shown in Figure 6, the active switching vectors are 217, 216, 108 (or 229).

To control 2 series-connected motor, in half of each switching period, the α-β reference vector, in α-β plane, is used as the reference vector and in half other, the x-y reference vector, in x-y plane, is used to determine the switching vectors. This strategy can be repeated in all of the sectors and shown in flowchart of Figure 7. It is worthwhile to note using the switching vectors for example in α-β plane, by above suggested method, the x-y components are negligible and vice versa. In this way, both α-β reference vector and x-y reference vector are realized.

It is better to normalize vectors by $V_S = 0.3236 V_{DC}$, then each switching vector coordinate becomes integer as shown in Figure 6.

From Figure 6, the coordinates of reference vector are obtained as follow

$$V_a = (\mathrm{c}tg\theta - ctg36^\circ)\sin\theta V_n^* \tag{18}$$

$$V_b = \frac{\sin\theta}{\sin 36^\circ} V_n^* \tag{19}$$

where θ is the angle between reference vector and a-axis in each section. The space vector PWM strategy is accomplished by the following equations

$$\begin{cases} V_{Ea}T_E + V_{Fa}T_F + V_{Ga}T_G = V_a T_s \\ V_{Eb}T_E + V_{Fb}T_F + V_{Gb}T_G = V_b T_s \\ T_E + T_F + T_G = T_s \end{cases} \tag{20}$$

where T_E, T_F and T_G are the apical switching vectors in each triangle region; and T_s is half of the switching period.

For simplicity the switching times for all of the regions are calculated in Table 1.

6. Simulation Results

The proposed control scheme is implemented in a block diagram shown in Figure 8. In this figure, only control of IM1 is illustrated (some subscripts are omitted for the sake of brevity), the same can be applied to IM2.

Notice that the SM controller and observer gains are obtained by trial and errors. Similarly the coefficients of sp eed PI controller are obtained as $k_p = 10$, $k_i = 1.1$.

Simulation results are obtained for a two different five-phase squirrel cage IM with parameters shown in Table 2.

The IMs speeds and stator fluxes control results are obtained and shown in Figure 9(a) and Figure 9(b) respectively. These results obtained for an exponential reference rotor speed from zero to 80 rad/s for machine 1 and an exponential reference rotor speed from zero to 40 rad/s for machine 2. The amplitudes of stator fluxes are

Table 1. Calculation of switching times in each region

Region A: $V\begin{cases}(V_{Ea},V_{Eb})=(0,0)\\(V_{Fa},V_{Fb})=(1,0)\\(V_{Ga},V_{Gb})=(0,1)\end{cases}\Rightarrow\begin{cases}T_F=V_aT_s\\T_G=V_bT_s\\T_E=T_s-T_F-T_G\end{cases}$

Region B: $\begin{cases}(V_{Ea},V_{Eb})=(0,1)\\(V_{Fa},V_{Fb})=(1,0)\\(V_{Ga},V_{Gb})=(1,1)\end{cases}\Rightarrow\begin{cases}T_E=(1-V_a)T_s\\T_F=(1-V_b)T_s\\T_G=T_s-T_E-T_F\end{cases}$

Region C: $\begin{cases}(V_{Ea},V_{Eb})=(0,1)\\(V_{Fa},V_{Fb})=(1,1)\\(V_{Ga},V_{Gb})=(0,2)\end{cases}\Rightarrow\begin{cases}T_E=(2-V_a-V_b)T_s\\T_F=V_aT_s\\T_G=T_s-T_E-T_F\end{cases}$

Region D: $\begin{cases}(V_{Ea},V_{Eb})=(1,0)\\(V_{Fa},V_{Fb})=(2,0)\\(V_{Ga},V_{Gb})=(1,1)\end{cases}\Rightarrow\begin{cases}T_E=(2-V_a-V_b)T_s\\T_G=V_bT_s\\T_F=T_s-T_E-T_G\end{cases}$

Table 2. Im parameters

Machine 1 [23]:			
Pn1	3hp	f	50Hz
P_1	3	R_{s1}	0.78 Ω
R_{r1}	0.66 Ω	L_{s1}	33.15mH
L_{r1}	33.15mH	L_{m1}	29.7mH
Machine 2 [19]:			
Pn2	7.5hp	f	50Hz
P_2	2	R_{s2}	10 Ω
R_{r2}	6.3 Ω	L_{s2}	460mH
L_{r1}	460mH	L_{m2}	420mH

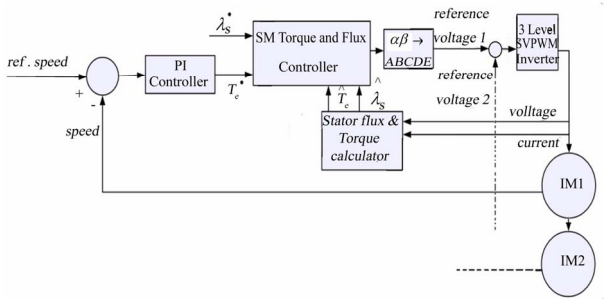

Figure 8. Drive system block diagram

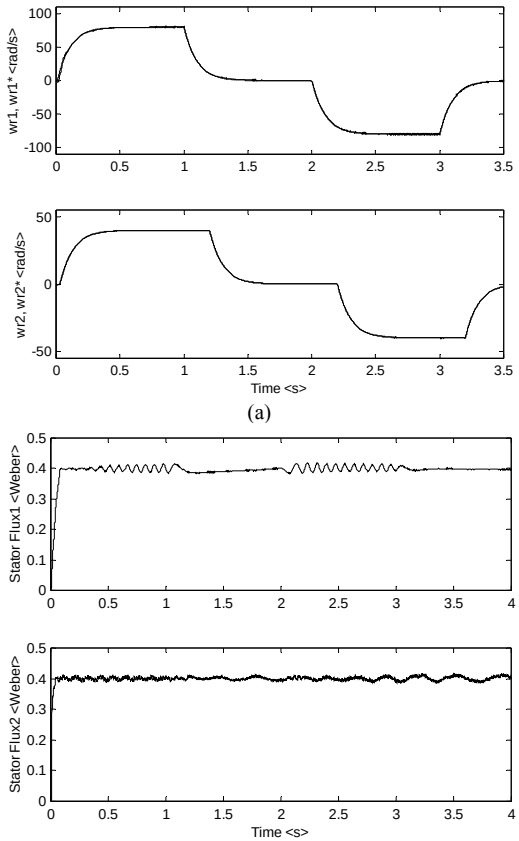

(a)

(b)

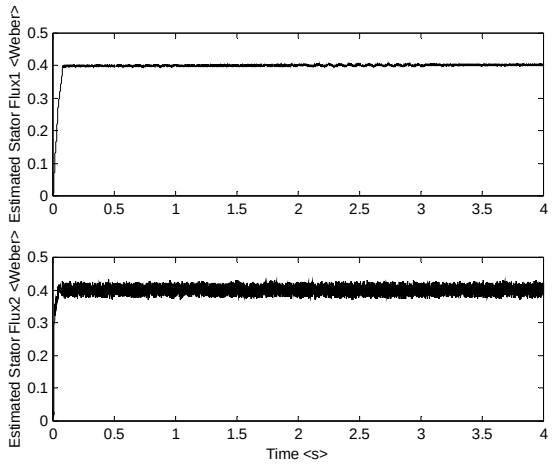

(c)

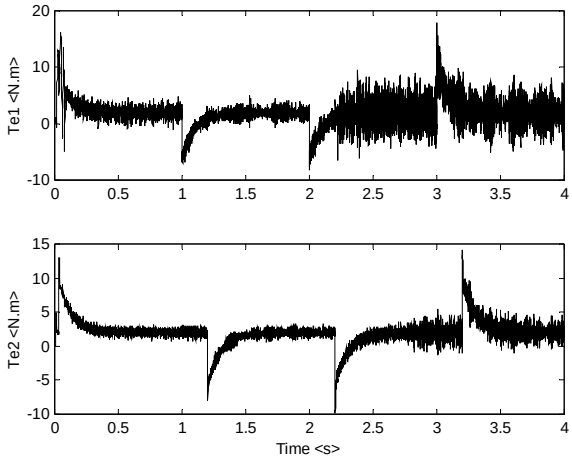

(d)

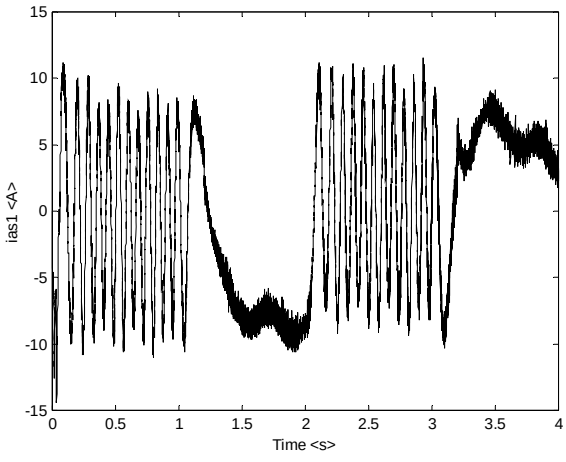

(e)

Figure 9. a) Rotor speeds; b) Stator fluxes; c) Estimated stator fluxes; d) Motors torques; e) Motors phase 'a' currents

kept constant (0.4 Wb for both IMs).

The speeds and fluxes track their references with a good dynamics. It is evident from these Figs. that the flux of the IM2 remains unaffected during the transient of the speed of IM1 and vice versa, moreover the speeds are also almost unaffected. These results verify the ability of the proposed control and SVPWM technique during speed start up and speed reversal.

In addition, the motors stator flux estimated results are shown in Figure 9(c).

Finally the torque and phase a current of IMs are shown in Figures 9(d) and 9(e) respectively. The inverter phase 'a' current (i_{as1}) includes two frequencies to run both IMs.

7. Conclusions

This paper has discussed a two five-phase series-connected IM drive which is supplied by a 3 level five-phase SPWM VSI.

An SM controller is used that is capable of controlling the stator flux and torque of each motor separately.

The proposed controller in this paper is capable to track the speed reference and the flux reference in spite of motor resistances mismatching. In addition, the transient dynamic of the motors stator fluxes and torques is precisely regulated by the design of SM controller. Moreover an algorithm is suggested to produce α-β and x-y voltage components with a 3 level SVPWM VSI.

The effectiveness and validity of the proposed control method is verified by simulation results.

REFERENCES

[1] H. A. Toliyat, "Analysis and simulation of five-phase variable-speed induction motor drives under asymmetrical connections," IEEE Transactions on Power Electronics, Vol. 13, No. 4, pp. 748–756, July 1998.

[2] D. Dujic, G. Grandi, M. Jones, and E. Levi, "A space vector PWM scheme for multifrequency output voltage generation with multiphase voltage-source inverters," IEEE Transactions on Industrial Electronics, Vol. 55, No. 5, pp. 1943–1955, May 2008.

[3] E. Levi, D. Dujic, M. Jones, and G. Grandi, "Analytical determination of DC-Bus utilization limits in multiphase VSI supplied AC drives," IEEE Transactions on Energy Conversion, Vol. 23 No. 2, pp. 433–443, June 2008.

[4] V. Oleschuk, F. Profumo, and A. Tenconi, "Analysis of operation of symmetrical dual three-phase converters with hybrid schemes of synchronised PWM," International Review of Electrical Engineering (IREE), Vol. 2, No. 6, December 2007.

[5] M. J. Duran, F. Salas, and M. R. Arahal, "Bifurcation analysis of five-phase induction motor drives with third harmonic injection," IEEE Transactions on Industrial Electronics, Vol. 55, No. 5, pp. 2006–2014, May 2008.

[6] R. Kianinezhad, B. Nahid-Mobarakeh, L. Baghli, F. Betin, and G.-A. Capolino, "Modeling and control of six-phase symmetrical induction machine under fault condition due to open phases," IEEE Transactions on Industrial Electronics, Vol. 55, No. 5, pp. 1966–1977, May 2008.

[7] N. R. Abjadi, J. Soltani, and J. Askari, "Nonlinear sliding-mode control of a multi-motors web winding system without tension sensor," IEEE International Conference on Industrial Technology (ICIT 2008), pp. 1–6, April 21–24, 2008.

[8] E. Levi, S. N. Vukosavic, and M. Jones, "Vector control schemes for series-connected six-phase two-motor drive systems," IEE Proceedings-Electronics Power Applications, Vol. 152, No. 2, pp. 226–238, March 2005.

[9] M. Jones, S. N. Vukosavic, E. Levi, and A. Iqbal, "A six-phase series-connected two-motor drive with decouple-ed dynamic control," IEEE Transactions on Industrial Applications, Vol. 41, No. 4, pp. 1056–1066, July–August 2005.

[10] K. K. Mohapatra, R. S. Kanchan, M. R. Baiju, P. N. Tekwani, and K. Gopakumar, "Independent field-oriented control of two split-phase induction motors from a single six-phase inverter," IEEE Transactions on Industrial Electronics, Vol. 52, No. 5, pp. 1372–1382, October 2005.

[11] M. Jones, S. N. Vukosavic, and E. Levi, "Parallel-connected multiphase multidrive systems with single inverter supply," IEEE Transactions on Industrial Electronics, Vol. 56, No. 6, pp. 2047–2057, June 2009.

[12] E. Levi, M. Jones, S. N. Vukosavic, and H. A. Toliyat, "A five-phase two-machine vector controlled induction motor drive supplied from a single inverter," EPE Journal, Vol. 14, No. 3, pp. 38–48, August 2004.

[13] K. K. Mohapatra, M. R. Baiju, and K. Gopakumar, "Independent speed control of two six-phase induction motors using a single six-phase inverter," EPE Journal, Vol. 14, No. 3, pp. 49–62, June–August 2004.

[14] M. Jones, E. Levi, and A. lqbal, "A five-phase series-connected two-motor drive with current control in the rotating reference," 35th Annual IEEE Power Electronics Specialists Conference, Aochen, Gemany, pp. 3278–3284, 2004.

[15] J. W. Kelly, E. G. Strangas, and J. M. Miller, "Multiphase space vector pulse width modulation," IEEE Transactions on Energy Conversion, Vol. 18, No. 2, pp. 259–264, June 2003.

[16] J. W. Kelly, E. G. Strangas, and J. M. Miller, "Multiphase inverter analysis," Proceedings of IEEE International Electric Machines Drives Conference (IEMDC), pp. 147–155, 2001.

[17] H.-M. Ryu, J.-H. Kim, and S.-K. Sul, "Analysis of multiphase space vector pulse-width modulation based on multiple d-q spaces concept," IEEE Transactions on Power Electronics, Vol. 20, No. 6, pp. 1364–1371, November 2005.

[18] L. Parsa, "On advantages of multi-phase machines," 32nd Annual Conference of IEEE Industrial Electronics Society (IECON), pp. 1574–1579, 2005.

[19] E. Levi, A. Iqbal, S. N. Vukosavic, and H. A. Toliyat, "Modeling and control of a five-phase series-connected two-motor drive," The 29th Annual Conference of the IEEE Industrial Electronics Society (IECON), Vol. 1, pp. 208–2132, 003.

[20] Q. Song, X. Zhang, F. Yu, and C. Zhang, "Research on space vector PWM of five-phase three-level inverter," Proceedings of the Eighth International Conference on Electrical Machines and Systems, ICEMS, Vol. 2, pp. 1418–1421, 2005..

[21] C. Lascu, I. Boldea, and Frede Blaabjerg, "Direct torque control of sensorless induction motor drives: A sliding-mode approach," IEEE Transactions on Industrial Applications, Vol. 40, No. 2, pp. 582–590, March–April 2004.

[22] C. Lascu and G.-D. Andreescu, "Sliding-mode observer and improved integrator with DC-Offset compensation for flux estimation in sensorless-controlled induction motors," IEEE Transactions on Industrial Electronics, Vol. 53, No. 3, pp. 785–794, June 2006.

[23] K. N. Pavithran, R. Parimelalagan, and M. R. Krishnamurthy," Studies on inverter-fed five-phase induction motor drive," IEEE Transactions on Power Electronics, Vol. 3, No. 2, pp. 224–235, April 1988.

Energy and Power Engineering, 2010, 18-24
doi:10.4236/epe.2010.21004 Published Online February 2010 (http://www.scirp.org/journal/epe)

Cr^{+3} Distribution in Al_1 and Al_2 Sites of Alexandrite ($BeAl_2O_4$: Cr^{3+}) Induced by Annealing, Investigated by Optical Spectroscopy

Neilo M. TRINDADE[1], Rosa M. F. SCALVI[2], Luis V. A. SCALVI[2*]
[1]*Programa de Pós-Graduação em Ciência e Tecnologia de Materiais* (*POSMAT*)*-FC, UNESP, C. P.* 473, *Bauru, SP, Brazil*
[2]*Physics Department-FC-State University of São Paulo—UNESP, CP* 473, *CEP* 17033-360, *Bauru, SP, Brazil*
Email: *scalvi@fc.unesp.br*

Abstract: In order to investigate optical properties of alexandrite, the present work deals with the influence of thermal annealing on optical absorption and luminescence spectra of natural samples. The exposure time to heat treatment at 1000°C is taken into account. Possible migration of Cr^{3+} ions from Al_1 (inversion site) to Al_2 (reflection site) is detected. Sample composition is obtained through Scanning Electron Microscopy (SEM) measurements and points to a rearrangement of Cr^{+3} and Fe^{3+} ions in the alexandrite crystalline structure, under thermal annealing influence. This feature may be used to control the optical properties of natural alexandrite, which can be associated to the observed laser emission effect.

Keywords: A. oxides, D. optical properties, D. defects

1. Introduction

Alexandrite is a rather rare and precious mineral and the interest on its production goes from gemological to laser technology. Alexandrite structure is of chrysoberyl type with the incorporation of chrome in its lattice, according to the chemical formula: $BeAl_2O_4$:Cr^{3+}. This material became technologically important from 1974, when its utilization as an active media for laser action became known, through the utilization in a synthetic form [1]. Alexandrite emission can be tuned in the range 700-800nm [2]. There is a great interest for the alexandrite laser in the present days since it has been vastly used for medical purposes, presenting superior performance compared to other lasers [3–5]. The combination of the chromIum doping and chrysoberyl matrix leads to very favorable properties. The alexandrite crystal is mechanically rigid and presents a fair thermal conduction. The alexandrite laser is able to resist to higher repetition rates, and emit a higher average output power, when compared to other Cr^{3+} lasers [6]. Although its utilization has been widely spread, the laser effect, which is related to its optical properties, is not completely understood. This issue has motivated very recent research on this subject [7]. Besides, Brazil is one of the largest producers of natural alexandrite, which possess a high gemological value, related to the alexandrite effect. This effect means a color change from green, under exposition to sunlight, to red, on illumination by an incandescent lamp [8].

The alexandrite unit cell can be visualized as approximately hexagonal close packed (hcp) and composed of four molecules, with eight Al^{3+} ions, occupying distorted octahedral sites, and four Be^{2+} ions, located at tetrahedral distorted sites, besides oxygen ions located in plans perpendicular to c axis [9]. Distortions from a precise hcp structure of oxygen ions originate two sites of distinct symmetries: one is called Al_1, located at an inversion site and the other is called Al_2, located at a reflection site [10]. Both Al sites are octahedrally coordinated. The Al_2 coordination octahedron has a larger Al-O average bond length (1.938 Å) when compared to the Al_1 octahedron (1.890 Å) resulting in a larger polyhedral volume [7]. It is known that Al_2, due to its larger size, is preferentially occupied by the Cr^{3+} ions and it is the main responsible for the optical properties of alexandrite [11]. A recently reported work [8] shows the importance of the doping with chromium ions in alexandrite, and claims that the saturation of the green and the red color is virtually determined only by the relative amount of chromium ions replacing aluminum in Al_1 and Al_2 sites. Besides, the color depends on the relative concentration of other impurities, such as titanium and iron [8].

In order to investigate optical properties of this material, the optical absorption technique has demonstrated as very appropriate to analysis of the impurities effect [12]. Previous published data [13] show that spectroscopic properties of Cr^{3+} ion in alexandrite are similar to

Table 1. Composition of natural alexandrite obtained through EDS analysis for two samples

Composition (wt%)		
Element	*Sample I*	*Sample II*
C	0.74	1.54
Na	0.14	-
Mg	0.07	0.30
Al	76.45	77.47
Si	13.33	8.74
Cl	0.10	0.55
K	0.37	1.37
Ca	0.15	0.90
Ti	0.12	0.24
Cr	0.09	0.17
Fe	0.44	1.93

Table 2. Compositional analysis, particularly for Fe and Cr of natural alexandrite obtained by WDS

Sample	Wt%Cr	Wt%Fe
I	0.13	0.61
II	0.41	0.37

Cr^{3+} ion effect in other oxide hosts with octahedral symmetry such as Al_2O_3 and $YAlO_3$. In all of them, the spectra present two well defined lines $^4A_{2g} \leftrightarrow {}^2E_g$ (R lines) and two wide absorption bands. However, the intensity and relative position of the lines related to these transitions depend on the host nature [14]. In the case of alexandrite, these wide bands are associated with the transition from ground state $^4A_{2g}$ to excited states $^4T_{2g}$ (band A, centered at 590nm) and $^4T_{1g}$ (band B, centered at 420 nm). These A and B bands are attributed to Cr^{3+} and Fe^{3+} ions, which may be present in the two sites of distinct symmetries. A third band has been reported [15], and has been related either to a charge transfer transition or to a transition terminating in one of highest levels of the $3d^3$ configuration, such as the $^4T_{1g}$ levels [16,17]. This band is generally called C, located in the UV region, being hardly observed in the optical absorption spectra, because this range is strongly influenced by Fe^{3+} traces [18].

In this paper, we present results of optical absorption measurements on natural alexandrite samples, along with results obtained for a synthetic sample, for comparison. These data allow identifying an Ultraviolet (UV) band, besides broad bands in the visible (VIS) range. The influence of thermal annealing at 1000°C is taken into account. Previous results of X-Ray Diffraction (XRD) and Energy Dispersive Spectroscopy (EDS) corroborate to the obtained conclusions.

2. Experimental

All the natural samples used in this paper come from the same mine, in the Minas Gerais state, Brazil. The synthetic sample was grown by the Czochralski method, and has been initiated by a high-quality crystalline seed. This sample has been described elsewhere [19]. Optical absorption measurements were carried out in the range 200 to 700nm (UV-VIS), using a spectrophotometer Cary 1G of Varian. For absorption data obtained at 77K, a liquid nitrogen cryostat was used, which was placed close to the spectrophotometer excitation slit. Luminescence data was obtained through excitation with an Argon laser from Spectra Physics, model 2017, with main excitation energy of 2.51eV. The laser beam excites the sample located inside a He closed-cycle Janis Research cryostat, model CS-150, which uses a Cryogenics compressor, model 8200. The emitted light is acquired by a Jobin Yvon T6400 spectrophotometer and the signal is detected by CCD (Charge Coupled Device) also from Jobin Yvon.

Thermal annealing was accomplished by varying time, with the temperature fixed at 1000°C, under room pressure conditions. Natural alexandrite samples were annealed according to the following procedure: the oven temperature was raised until 1000°C with 20°C/min of rate and kept at this temperature by the desired time. The cooling down is done using the same temperature rate. Samples were submitted to consecutive annealing whereas the optical absorption spectra are recorded between each annealing.

Chemical composition of these samples was measured by EDS (Energy Dispersive Spectroscopy) and WDS (Wavelength Dispersive Spectroscopy), particularly Al, Cr and Fe concentration. Table 1 presents composition obtained through EDS from the analysis of two natural alexandrite samples coming from the same source, and Table 2 presents the compositional analysis, particularly for Fe and Cr present in these samples, obtained by WDS. The Fe composition is very relevant in the alexandrite sample, because a high amount of this impurity may mask the identification of optical absorption bands attributed to Cr^{3+} in the host matrix. As can be verified in Tables 1 and 2, Fe has higher concentration compared to Cr in natural alexandrite. EDS analysis was performed in order to determine the presence of the most concentrated elements in the material and these results are semiquantitative, since the oxygen determination is not reliable and beryllium is not detected by this technique. On the other hand, the Fe and Cr composition determined by WDS are practically quantitative, since it is possible to determine the oxygen concentration. Results are as expected since natural materials present several types of

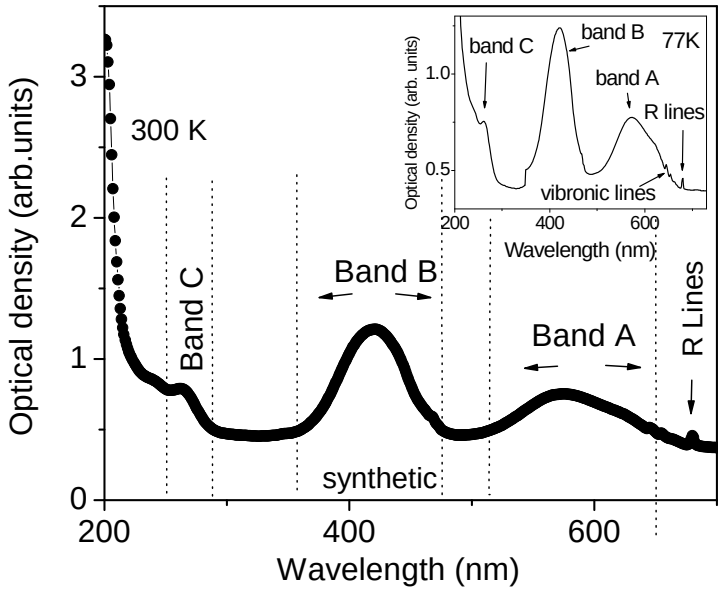

Figure 1. Optical absorption spectra of synthetic alexandrite samples, measured at room temperature (300K). Inset-optical absorption spectra of synthetic alexandrite, measured at liquid nitrogen temperature (77K).

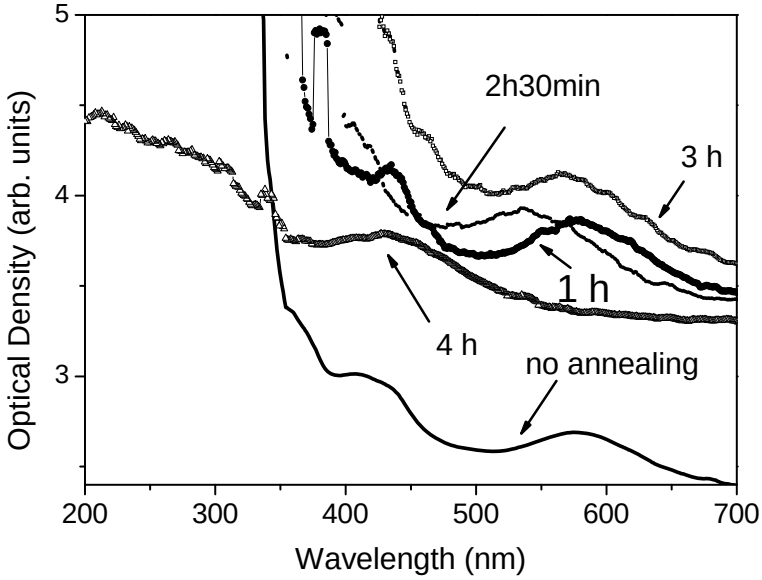

Figure 2. Optical absorption spectra of natural alexandrite as function of consecutive annealing

impurities incorporated in the original stone. Moreover, these data confirm that the presence of Fe in these samples is high, surmounting the presence of Cr in the material.

3. Results and Discussion

Figure 1 shows optical absorption spectra for synthetic alexandrite, measured at 300K. The inset in Figure 1 represents the absorption spectra for the same synthetic sample, measured at 77K. Bands A and B are clearly identified. Band C is also identified, which becomes possible due to the absence of iron in the synthetic sample composition. The lines R in alexandrite are attributed to Cr^{3+} located at Al_2 sites on a reflection plane (lines R_1 and R_2), and show up precisely at same wavelength either in the emission as well as in the absorption spectra, at 680.4 and 678.5nm, respectively [20]. The lines R are responsible by optical properties of alexandrite.

Band A represents overlapping of two absorption bands of Cr^{3+} ions in two distinct sites Al_1 and Al_2. Band B represents Cr^{3+} and Fe^{3+} also incorporated at different

sites. Relevant parameters for the synthetic sample are obtained from Figure 1, such as band wavelength position, absorption coefficient and the full width a half maximum ($\Delta\lambda$), and are presented in Table 3. As can be verified, the results of optical absorption at room temperature and at liquid nitrogen temperature, in synthetic alexandrite, show agreement in the position of absorption bands, absorption coefficients and $\Delta\lambda$, with no significant variations. This sample is used as a reference in this paper, due to its outstanding optical quality. The measurement carried out at 77 K (inset of Figure 1) shows clearly the vibronic transition lines at 645, 654 and 663 nm [21].

The influence of consecutive thermal annealing on optical absorption bands of natural alexandrite is shown in Figure 2. The analysis of variation in the spectra allows investigation of the possible migration of Cr^{3+} between Al_1 and Al_2 sites. Relevant parameters for this material, such as $\Delta\lambda$ and absorption coefficient are obtained from Figure 2, and are presented in Table 4.

With the help of Tables 3 and 4, bands A and B of natural alexandrite samples without thermal annealing and the bands due to synthetic sample, recorded at room temperature, can be compared. It is easily verified that their central position (λ) shows a short shift. A larger difference occurs between their absorption coefficients, where the synthetic sample presents lower values than the natural alexandrite. Natural sample shows an absorption coefficient 12 times higher for band A and 5 times higher for band B compared to the values of corresponding bands for the synthetic sample. That can be explained by the Cr concentration, which is higher for natural material and also due to the Fe concentration, which is present only in the natural samples. This is in good agreement with the lower optical density and higher transparency of synthetic sample.

Concerning the natural sample, the absorption spectra present large bands centered about 580 and 585nm (band A) and 425 and 435 nm (band B), besides the R lines, close to 680nm. Thermal annealing causes a consecutive and discrete increase in the optical absorption coefficients and a broadened band, which must be related to the increase of Cr^{3+} population in sites Al_1 and Al_2. This statement is reinforced by decomposition of this band, as shown in Figure 3. Band A vanishes with thermal annealing during 4 h, when the noise in the UV starts to disappear and band C begins to gain shape. This band had previously been found only with 5h of thermal annealing [21]. It shows that thermal treatment is an efficient method of refining the optical absorption data. Then, the emerging of band C can be related to the disappearing of band A. It is known that band A is an absorption band from Cr^{3+} ions in sites Al_1 and Al_2 and band C is also related with presence of Cr^{3+} [15]. Then, one may conclude that thermal annealing leads to diffusion of Cr^{3+} through the alexandrite lattice. An increase of absorption coefficient of band B is taking place, presenting a maximum with 2h of annealing time, vanishing with 2 and a half hours and showing up back, but with lower absorption coefficient with 4 h of thermal treatment. These modifications indicate migrations of Cr^{3+} and/or Fe^{3+} ions throughout the materials structure, revealed by the variation of $\Delta\lambda$. The lines R, either can be observed in a sole line, or separated in two lines, called R_1 and R_2. The line R_1 is located around 680- 682nm and R_2 around 678-680nm.

The analysis of optical absorption bands behavior of natural alexandrite sample submitted to thermal annealing can be done by comparing with synthetic sample (Figure 1). In our approach, the band A is decomposed in two Gaussian curves, in order to estimate the relative amount of Cr^{3+} ions between Al_1 and Al_2 sites [14] and the migration caused by thermal annealing. The data fitting for the synthetic sample, shown in Figure 3, leads to the best fitting of band A, when a regression of two Gaussian curves is used. Band A corresponds to overlapping of optical absorption bands from Cr^{3+} located in sites Al_1 and Al_2, as already mentioned. Al_2 is larger than Al_1, and then, it is preferentially occupied by Cr^{3+} ions. There is a dependency on color shift and other optical properties with Cr^{3+} distribution among these sites,

Table 3. Parameters obtained from optical Absorption data for synthetic alexandrite, at 300 and 77 K. λ means the position of maxima. α is the optical absorption coefficient and Δλ is full width a half maximum

T (K)	Optical Absorption bands – Synthetic sample									Absorption Lines of Cr^{3+}
	Band A (Cr^{3+})			Band B (Cr^{3+}, Fe^{3+})			Band C (Cr^{3+})			
	λ (nm)	α (cm^{-1})	Δλ (nm)	λ (nm)	α (cm^{-1})	Δλ (nm)	λ (nm)	α (cm^{-1})	Δλ (nm)	λ (nm)
300	583	0.31	91.5	420	0.75	59.5	267	0.11	16.8	680
77	582	0.32	90	419	0.76	56.6	265	0.11	15.8	680

Table 4. Parameters obtained from optical Absorption data (UV-Vis) for natural alexandrite sample after thermal annealing. λ means the position of maxima. α is the optical absorption coefficient and Δλ is full width a half maximum

	Absorption bands of natural alexandrite									Absorption
	Banda A (Cr^{3+})			Banda B (Cr^{3+}, Fe^{3+})			Banda C (Cr^{3+})			Lines of Cr^{3+}
	λ (nm)	α (cm^{-1})	Δλ (nm)	λ (nm)	α (cm^{-1})	Δλ (nm)	λ (nm)	α (cm^{-1})	Δλ (nm)	λ (nm)
STT	585	3.71	85	426	3.9	47.8	-	-	-	680
TT1000ºC/ 1h	585	5.76	93.8	429	4.36	46.2	-	-	-	680 and 682
TT1000ºC/ 1h 30min	583	4.24	84	428	6.08	48.9	-	-	-	679
TT1000ºC/ 2h	585	5.71	89.7	432	8.11	46.9	-	-	-	679 and 681
TT1000ºC/ 2h30min	563	4.9	89.64	-	-	-	-	-	-	-
TT1000ºC/ 3h	577	7.2	96.98	-	-	-	-	-	-	-
TT1000ºC/ 4h	-	-	-	429	1.8	57.67	276	6.4	57.4	680

which was determined by Electron Paramagnetic Resonance (EPR) [11,22], and indicates that Cr^{3+} in $BeAl_2O_4$ enters in a average ration of 75% in Al_2 and 25% in Al_1, either in natural sample as well as synthetic alexandrite sample. Based on this ratio, the analysis of Figure 3 was performed and the results are shown in Table 5. With the help of Figures 1 and 2, it may be concluded from Table 5 that in the synthetic sample, we have the 1:3 ratio in agreement with previous mentioned reported data [11, 22]. The addition of two Gaussian curves leads to a perfect fitting of the experimental curve. Then, they can be used to the analysis of the absorption band of natural sample. In this case, the fitting by Gaussian curves is hard to be done, which is caused by the experimental noise. In the cases where a data fitting of band A became possible, it was observed that an increase of thermal annealing time leads to decrease of Cr^{3+} in Al_1 sites and thus, an increase in the occupation of Al_2 sites. Besides, there is an increase of the Gaussian curves area, which

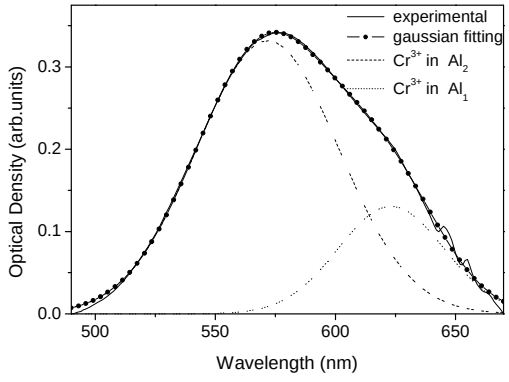

Figure 3. Decomposition of band A of optical absorption spectra in two Gaussian curves for synthetic alexandrite

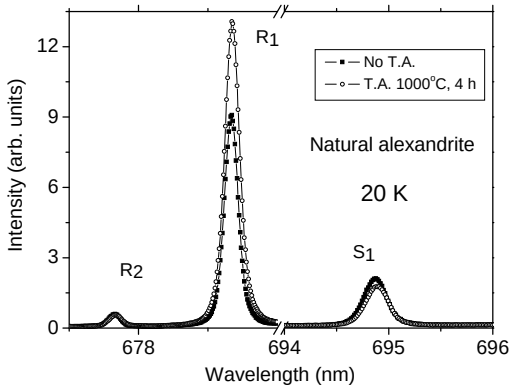

Figure 4. Photoluminescence spectra of natural alexandrite, measured ate 20 K, before any thermal annealing and after the final annealing at 1000ºC, 4 hour

Table 5. Analysis of bands A, B and C of natural and synthetic alexandrite samples, obtained from decomposition of optical absorption bands

	Band A		Average total area (a. u.)		
Thermal annealing temperature/time	Al_1(%)	Al_2(%)	Band A	Band B	Band C
STT	33.5	66.5	15.7	20.4	-
1000ºC/5min	22.1	77.9	24.2	15.4	-
1000ºC/15min	14.5	85.5	24.7	17.5	-
1000ºC/30min	15	85	28.1	44.8	-
1000ºC/2h	-	-	29.0	79.3	-
1000ºC/2h30min	18.2	81.8	35.6	-	-
1000ºC/3h	4.8	95.2	41.4	-	-
1000ºC/4h	-	-	-	14.1	35.7
Synthetic sample	22.7	77.3	31.8	50.4	3.1

means an increase of Cr^{3+} concentration, responsible for the optical absorption in the sample. Cr^{3+} ions in Al_2 sites are responsible for laser emission, which are characterized by electric dipole transitions of high-probability,

whereas Cr^{3+} ions in Al_1 do not contribute significantly to the optical absorption. The excitation of Cr^{3+} located in Al_1 ions are magnetic dipole transitions, and do not participate in the laser emission process. Besides, this transition contributes for decreasing the excitation energy of Cr^{3+} in Al_2 [23].

As expected from the absorption coefficient data, the area under band B also increases until 2 h of annealing time, however band B vanishes for longer times, as already mentioned. This band shows up again with 4 h of annealing along with band C. On the other hand, band A resists to the thermal annealing, vanishing only with 4 h of annealing time, when band C shows up. In summary, the analysis of bands A, B and C leads to the conclusion that bands A and B present increased area with longer thermal treatment.

In alexandrite luminescence spectra, the Cr^{+3} lines, due to the ion located in the reflection site, are the R_1 and R_2 lines and the lines due to Cr^{3+} located in the inversion site are S_1 and S_2. As previously mentioned, the R lines show up precisely at the same wavelength, 680.4 nm and 678.5 nm, either in the absorption spectra as well as in the emission spectra. Lines S_1 and S_2 show up at 695.8 and 689.9 nm, respectively in the emission spectra and as narrow lines at 655.7 nm, 649,3 nm and 645.2 nm in the absorption spectra [16]. In order to assure the hypothesis of ion migration, photoluminescence measurements on natural samples were carried out at low temperature (20K), before any thermal annealing and after the last annealing (1000°C, 4 hour). This measurement temperature was chosen in order to have a very well defined spectrum, not influenced by phonon emission. These results are shown in Figure 4, where lines R_1, R_2 and S_1 are easily observed, whereas S_2 line is not observed. The most relevant information for this work is that the R_1 line has its intensity increased by the thermal annealing, whereas S_1 presents lower intensity. This behavior reinforces the possibility of ion migration from the inversion site, Al_1, to the reflection site, Al_2, in good agreement with our absorption data fitting procedure.

Previously reported X-ray diffraction data for alexandrite sample before and after thermal annealing [24] show that the characteristic peaks occur at the same positions. Thermal annealing does not cause modifications on alexandrite structure, which is a very interesting result, since our main goal is to study its optical properties related to Al_1 and Al_2 occupation by Cr^{3+} ions, and the variations on optical properties induced by thermal annealing.

4. Conclusions

We summarize the conclusions that we have drawn in this paper as follows: thermal annealing has allowed the observation of meaningful variation on the optical absorption bands of natural alexandrite in the visible and ultraviolet ranges. Depending on time of thermal annealing at 1000°C the bands A, B and C have its shape completely changed. The annealing favors the presence of Cr^{3+} in Al_2 sites, which was verified by alteration in the specific areas of the decomposed absorption bands and variation of relative emission intensity. This may also explains why, unlike other tunable lasers, alexandrite lasers emit with fair efficiency even at room temperature. Chemical composition shows that the iron concentration is high in the natural alexandrite, which does not ruin the conclusion on Cr^{3+} optical absorption properties drawn in this paper, because although the Fe ions present strong influence in the ultraviolet range, the analyzed bands related to Cr ions are in the visible range.

5. Acknowledgements

Authors thank the financial support of Brazilian agencies: FAPESP, CNPq, FUNDUNESP and CAPES. We also thank Prof. Lígia O. Ruggiero and Prof. Américo Sheitiro Tabata for the use of the equipments and Prof. Tomaz Catunda for the use of the synthetic sample.

REFERENCES

[1] J. C. Walling, O. G. Peterson, H. P. Jenssen, R. C. Morris, and E. W. O´Dell, "Tunable alexandrite lasers," IEEE Journal of Quantum Electronics, Vol. QE-16, pp. 1302–1314, 1980.

[2] J. C. Walling, D. F. Heller, H. Samelson, D. J. Harter, A. J. A. Pete, and R. C. Morris, "Tunable alexandrite lasers: development and performance," IEEE Journal of Quantum Electronics, Vol. QE-21, pp 1568–1581, 1985.

[3] L. Li, T. Kono, W. F. Groff, H.M. Chan, Y. Kitazawa, and N. J. Nozaki, "Comparison study of a long-pulse pulsed dye laser and a long-pulse pulsed alexandrite laser in the treatment of port wine stains," Journal of Cosmetic and Laser Therapy, Vol. 10, pp. 1472–1476, 2008.

[4] N. Bouzari, H. Tabatabai, Z. Abbasi, and A. Frios, "Laser hair removal: Comparison of long-pulsed Nd: YAG, 'Long-pulsed alexandrite, and long-pulsed Diode Lasers'," Dermatologic Surgery, Vol. 30, pp. 498–502, 2008.

[5] M. Landthaler and U. Hohenleutner, "Laser therapy of vascular lesions photodermatology," Photoimmunology & Photomedicine, Vol. 22, pp. 324–332, 2006.

[6] S. C. Collins, T. D. Wilkerson, V. B. Wickwar, D. Rees, J. C. Walling, and D. F. Heller, "The alexandrite ring laser: A spectrally narrow lidar light source for atmospheric fluorescence and absorption observations in Advances in atmospheric remote sensing with Lidar," Edited by A. Ansmann, R. Neuber, P. Rairoux, and U. Wandinger, Springer Verlag, Berlin, pp. 577–580, 1997.

[7] S. U. Weber, M. Grodzicki, W. Lottermoser, G. J. Redhammer, G. Tippelt, J. Ponahlo, and G. Amthauer, "Fe Mossbauer spectroscopy, X-ray single-crystal diffrac-

tometry, and electronic structure calculations on natural alexandrite," Physics and Chemistry of Minerals, Vol. 34, pp. 507–515, 2007.

[8] V. I. Solomonov, S. G. Mikhailov, and A. I. Lipchak, "Impurity luminescence of alexandrite crystals," Journal of Applied Physics, Vol. 69, pp. 423–429, 2002.

[9] R. M. F. Scalvi, M. S. Li, and L. V. A. Scalvi, "Thermal annealing-induced electric dipole relaxation in natural alexandrite," Physics and Chemistry Minerals, Vol. 31, pp. 733–737, 2005.

[10] C. F. Cline, R. C. Morris, M. Dutoit, and P. J. Harget, "Physical properties of $BeAl_2O_4$ single crystals," Journal of Materials Science, Vol. 14, pp. 941–944, 1979.

[11] G. V. Bukin, A. V. Eliseev, V. N. Matrosov, V. P. Solntsev, E. I. Kharchenko, and E. G. Tsvetjov, "The growth and examination of optical properties of gem alexandrite," Proceedings of the XI IMA Meeting, Novosibirsk, pp. 317–328, 1980.

[12] J. A. Hernandez, W. K. Cory, and J. O. Rubio, "A non destructive method for determining the Eu^{2+} concentration in the alkali chlorides," Japanese Journal of Applied Physics, Vol. 18, pp. 533–538, 1979.

[13] M. J. Weber and T. E. Varitimos, "Optical spectra and relaxation of Cr^{3+} ion in $YAlO_3$," Journal of Applied Physics, Vol. 45, pp. 810–816, 1974.

[14] J. Xu, K. Shi, G. Xiong, and X. Xu, "The vibrational relaxation processes in $BeAl_2O_4$:Cr^{3+}", Journal of Luminescence, Vol. 40 & 41, pp. 611–612, 1988.

[15] A. E. Underhill and D. E. Billing, "Calculation of the Racah parameter B for Nickel (II) and cobalt (II) compounds," Nature, Vol. 210, pp. 834–835, 1966.

[16] R. C. Powell, L. Xi, X. Gang, and G. J. Quarles, "Spectroscopic properties of alexandrite crystals," Physical Review B, Vol. 32, pp. 2788–2797, 1985.

[17] A. B. Suchocki, G. D. Gilliland, R. C. Powell, and J. M Bowen, "Spectroscopy properties of alexandrite crystals II," Journal of Luminescence, Vol. 37, pp. 29–37, 1987.

[18] F. Hassan and A. El-Rakhawy, "Chromium III centers in synthetic alexandrite," American Mineralogist, Vol. 59, pp. 159–165, 1974.

[19] S. K. Pan and X. G. Wang, "Growth of laser crystal alexandrite," Crystal Research and Technology, Vol. 29, pp. k31–k35, 1994.

[20] P. Fabeni, G. P. Pazzi, and L. Salvini, "Impurity centers for tunable lasers in the ultraviolet and visible regions," Journal of Physics and Chemistry of Solids, Vol. 52, pp. 299–317, 1991.

[21] R. M. F. Scalvi, M. S. Li, and L. V. A. Scalvi, "Annealing effects on optical properties of natural alexandrite," Journal of Physics: Condensed Matter, Vol. 15, pp. 7437–7443, 2003.

[22] H. Rager, A. Bakhshand-Khiri, and K. Schmetze, "Investigation of the intracrystalline Cr^{3+} distribution in natural and synthetic alexandrites," N. Jb. Miner. Mh, Vol. 2 , pp. 545–557, 1998.

[23] B. K. Sevast'yanov, "Excited-state absorption spectroscopy of crystal dopede with Cr^{3+}, Ti^{3+}, and Nd^{3+} ions, review," Crystallography Reports, Vol. 48, pp. 989–1011, 2003.

[24] R. M. F. Scalvi, L. O. Ruggiero, and M. S. Li, "Influence of annealing on X-Ray diffraction of natural alexandrite," Powder Diffraction, Vol. 17, pp. 135–138, 2002.

Energy and Power Engineering, **2010, 25-30**
doi:10.4236/epe.2010.21005 Published Online February 2010 (http://www.scirp.org/journal/epe)

Research of Supercapacitor Voltage Equalization Strategy on Rubber-Tyred Gantry Crane Energy Saving System

Chunhe CHANG[1], Jiangping YANG[1], Yu LI[2], Zhongni ZHU[1]
[1]*Air Force Radar Academy, AFRA, Wuhan, China*
[2]*South-central University for Nationalities, SCUN, Wuhan, China*
Email: *cch*1725@163.*com*

Abstract: A model for supercapacitor voltage equalization strategy is analyzed, and on this basis a supercapacitor voltage equalization method for Rubber Tyred Gantry Crane (RTG) energy saving system is proposed, namely active voltage equalization method based on Buck-Boost converter. The equalizing speed of the proposed method is fast. Firstly, the working principle and process of the voltage equalization circuit is analyzed in detail. In addition, design of active voltage equalization circuit parameters and control strategy are given. Finally, simulation analysis of the series connection of supercapacitors module is performed. Results show that this method for equalizing voltage can avoid over-voltage of each cell and possess practicable and high value for supercapacitor RTG energy saving system.

Keywords: supercapacitor, energy saving, rubber tyred gantry crane (RTG), voltage sharing, sesign of active equalization circuit

1. Introduction

Supercapacitor is a novel energy storage device based on the principle of the double layer-electrolyte capacity, which has many merits such as long lifetime, high efficiency, fast dynamic response, etc. So it is a power storage technology that has a bright future in power storage development. The power driver system in energy -saving RTG is composed of the diesel generator set, power balance system (made by supercapacitors), controller and the rising electromotor. Supercapacitors are used for storing energy from which electromotor generates and brakes energy when the load is fallen down, the supercapacitors release the energy which has been stored when the load is raising. Thus the original energy which is consumed by the braking resistance is recycled totally, then the purpose of energy saving and environment protection is realized.

Due to the lower voltage of a single supercapacitor, generally speaking, the series and parallel connection of supercapacitors form the energy storage module to meet the energy storage capacity and higher voltage requirements. However, the operational voltage of supercapacitors is different, and a local over-voltage can appear over one or several supercapacitors, which would affect the lifetime and reliability of the system. Therefore, it is essential and critical to research and realize supercapacitors voltage equalization technology for improving the supercapacitors power storage technology.

The present supercapacitors voltage equalization technology mainly includes zener diode type, switch resistor type, switch capacitor type, inductor type, forward converter type and flyback converter type voltage equalization circuits, etc. The switching resistor type and voltage-regulator diode type voltage equalization circuits consume amount of energy because of utilizing energy-consuming devices, so the system has lower efficiency and poorer reliability [1]. The switching capacitor type and inductor type voltage equalization circuits have ineffective energy flowing, especially when the two adjacent supercapacitors voltage difference is very closer or when much more supercapacitors are in series connection, balancing speed will be slower [2]. Forward converter type and flyback converter type voltage equalization circuit have a higher efficiency, but they are not attractive, because they also have many demerits such as complicated magnetic circuit, big volume, difficult extended winding and large voltage equalization error, etc [3]. In view of the existing problems of the above voltage equalization methods, the paper proposes an active voltage equalization method based on the principle of Buck-Boost converter, this method can transfer energy from the high-voltage supercapacitors to the low-voltage ones through the converter rapidly, and it has the character of the low

energy loss and the high equalizing speed in the process of charging and discharging.

2. Analysis of Voltage Equalization Model

The supercapacitor charging equalizing model is shown in Figure 1. On the basis of the paper [4], the model is further analyzed in detail. Assuming the value of two optional supercapacitors are C_1 and C_2, d_1 and d_2 are capacity deviation values of the supercapacitors C_1 and C_2 respectively, we define the values of C_1 and C_2 as below:

$$C_1 = C(1+d_1),\quad C_2 = C(1+d_2) \tag{1}$$

where C is the reference value for capacitors.

If two supercapacitors are connected in series, both of the initial voltage values are zero, a constant current I charges supercapacitors, the voltage difference during the same time t is defined as following:

$$\Delta U = \left|U_{c1} - U_{c2}\right| = \frac{\Delta C}{C_1 C_2} It \tag{2}$$

where ΔC is the capacity difference between C_1 and C_2.

If two supercapacitors are connected in series, both of the initial voltage values are zero, when different constant currents I_{c1} and I_{c2} charge supercapacitors, the voltage difference during the same time t can be expressed as in (3):

$$\Delta U = \left(\frac{I_{c1}}{C_1} - \frac{I_{c2}}{C_2}\right)t \tag{3}$$

Substituting (1) into (3) when the voltage difference is zero, the relation between charging current and the supercapacitor capacity deviation can be obtained as follows:

$$\frac{I_{c1}}{I_{c2}} = \frac{C_2}{C_1} = \frac{1+d_1}{1+d_2} \tag{4}$$

If two supercapacitors are connected in series, both of the initial voltage values are zero, the supercapacitors voltage rise from zero to the upper voltage U_u when constant current charges supercapacitors, the two cells voltages can be, respectively, calculated as:

$$U_{c1} = \frac{1+d_1+d_2}{2+d_1+d_2}U_c,\quad U_{c2} = \frac{1}{2+d_1+d_2}U_c \tag{5}$$

where U_{c1} and U_{c2} are the voltages across the supercapacitors C_1 and C_2 at the end of charging and U_c is the total voltage. Obviously, the two supercapacitors capabilities are same when $d_1 = d_2 = 0$, thus, the capacitors voltages can be described as: $U_{c1} = U_{c2} = U_c/2 = U_u$.

As Figure 1 is shown, assuming a current of equalizing current supply $I_{eq} = k_j I$ (both the two current supplies are reverse direction) is parallel connected with each capacitor side, k_j is equalizing coefficient. Then, the charging current across C_1 and C_2 can be, respectively, described as:

$$I_{c1} = I(1-K_j),\ I_{c2} = I(1+K_j) \tag{6}$$

Substituting (6) into (4), the ration between constant current source I and the charging current I_{eq} can be expressed as follows:

$$k_j = \frac{d_2 - d_1}{2+d_1+d_2} \tag{7}$$

Then, the two supercapacitors charging current can be, respectively, calculated as:

$$I_{c1} = \frac{2+2d_1}{2+d_1+d_2}I,\quad I_{c2} = \frac{2+2d_2}{2+d_1+d_2}I \tag{8}$$

Usually the supercapacitor capacity deviation d is not zero, but it is a random value, which variable range is $-10\% \sim +20\%$. The relation between the equalizing current I_{eq} and the charging current I can be calculated from d and (7) when the supercapacitors are in voltage equalization state.

$$I_{eq} \geq 0.143I \tag{9}$$

From (3), it can be concluded that if the supercapacitors initial voltage is not zero, the voltage difference ΔU will decrease gradually, and k_j value continues to increase, the voltage difference across the supercapacitors reduces more quickly.

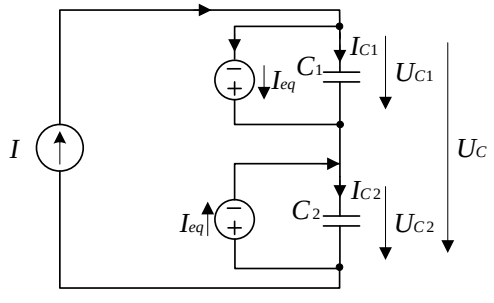

Figure 1. The supercapacitor charging equalizing model

3. Active Voltage Equalization Circuit

In view of the energy of the high-voltage supercapacitors is directly transferred to the low-voltage supercapacitors, this paper proposes an effective voltage equalization method-Active Circuit of Voltages Balance for the Series Supercapacitors. This method compares with the methods of "INDUCTION", and it is characterized by the low energy loss and the high equalizing speed in the process of charging and discharging.

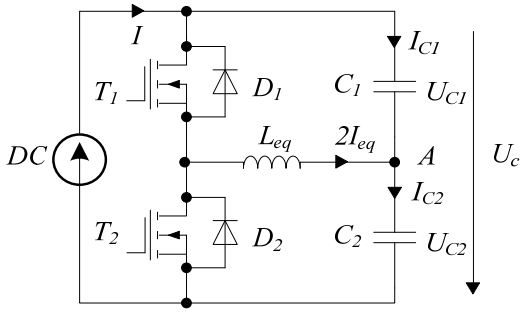

Figure 2. Active circuit of voltages equalization for two series supercapacitors

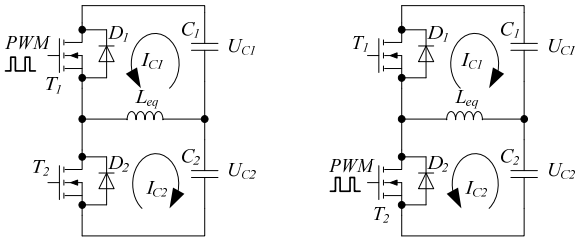

Figure 3. The principle circuit of active voltages balance

3.1 The Basic Operational Principle

As shown in Figure 6, switches T_1, T_2 are MOSFET; diodes D_1, D_2 are continued flow diodes; L_{eq} is the energy storage inductor; C_1, C_2 are two adjacent series cells, respectively. A Buck-Boost converter can be connected with two adjacent cells of supercapacitors.

The basic operational principle is shown in Figure 7. As is shown in Figure 3(a) below, when $U_{c1} > U_{c2}$, a PWM drive signal is given to the switches, and switch T_2 is turned off and T_1 is turned on. While T_1 is on, supercapacitor C_1, switch T_1 and inductor L_{eq} forms a loop circuit, whose current is I_{c1}. The part of energy of supercapacitor C_1 transfers to inductor L_{eq}. While T_1 is off, supercapacitor C_2, inductor L_{eq} and the diode D_2 forms a loop circuit, whose current is I_{c2}. The energy of inductor L_{eq} transfers to supercapacitor C_2. Similarly, as is shown in Figure 3(b) below, when $U_{c1} < U_{c2}$, switch T_1 is turned off and T_2 is turned on. The energy transfers from C_2 to C_1 until the voltages of the two supercapacitors are same.

3.2 Analysis of Operation Process of Voltage Equalization

According to the above principle of voltage equalization, and in order to analyze the operation process of the circuit, assume that the following items are satisfied:

1) It is assumed that the voltage of diode, the internal resistance of inductor, the on-resistance of the switch and the resistance of the circuit are all ignored, and supercapacitors are assumed to be ideal capacitors;

2) The circuit works in discontinuous conduction mode (DCM);

3) The capacity of the supercapacitor C_m is less than that of C_{m+1}, that it is to say, the supercapacitor C_m voltage is higher than C_{m+1}, where m is positive integer;

4) Because of the large capacity of supercapacitors and high swtiching frequency, the supercapacitor can be seen as a voltage supply during a switching period.

Equivalent circuit of active voltage equalization system of two supercapacitors is shown in Figure 4. Referring to the above equivalent circuit, the operating process of the voltage equalization can be analyzed in detail as follows:

3.2.1 Operation Mode 1 ($0 \le t \le D_1T$)

At t =0, the switch T_m is turned on, the diode D_m is turned off. According to the above assumption, the Figure 4 can be equivalent to Figure 5. During this operation mode, the supercapacitor C_m charges inductor

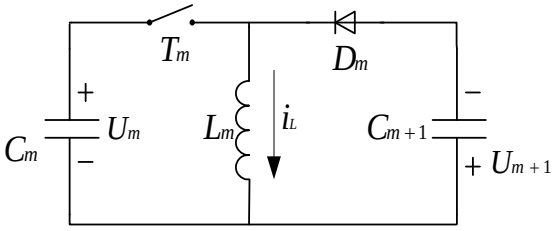

Figure 4. The equivalent circuit of active voltage equalization system

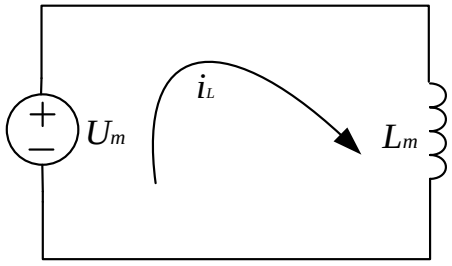

Figure 5. Equivalent circuit at mode 1

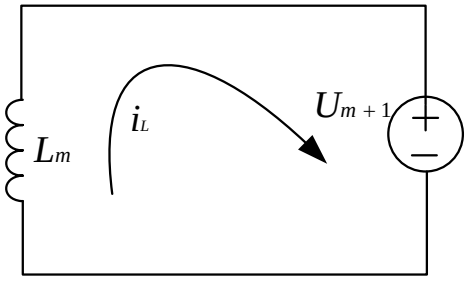

Figure 6. Equivalent circuit at mode 2

L_m, and energy is stored in inductor L_m, the inductor current keeps rising linearly. Thus,

$$L\frac{i_L}{D_1\times T}=U_m \tag{10}$$

3.2.2 Operation Mode 2 ($D_1T \le t \le (D_1+D_2)T$)

At $t=D_1T$, the switch T_m is turned off, the diode D_m is turned on. The Figure 4 can be equivalent to Figure 6. During this operation mode, the inductor L_m discharges supercapacitor C_m, energy is transferred to supercapacitor C_m, the inductor current keeps falling linearly from peak value to zero. Thus,

$$L\frac{i_L}{D_2\times T}=U_{m+1} \tag{11}$$

3.2.3 Operation Mode 3 ($(D_1+D_2)T \le t \le T$)

In this operation mode, the switch T_m and the diode D_m are all turned off.

4. Design and Simulation of Active Voltage Equalization Circuit

4.1 Design of the Active Voltage Equalization Circuit Parameters and Control Strategy

4.1.1 Operation Range of Duty Ratio

The following conclusion can be obtained from the (10) and (11).

$$U_m\cdot D_1=U_{m+1}\cdot D_2 \tag{12}$$

When the voltage equalization system works at steady state, the difference between U_m and U_{m+1} is very little. Thus, we can think $U_m=U_{m+1}=U$, in addition, because the circuit works in discontinuous conduction mode(DCM).

Then, $D_1+D_2<1$, $D_1=D_2$. thus,

$$D_1=D_2=D<50\% \tag{13}$$

From the above inequation, we can obtain $D<50\%$.

4.1.2 Inductor Selection

In a switching period, the working curve of inductor(L) current is shown in the Figure 7. The average current releases from Supercapacitor to the inductor L is:

$$I_{avg}=\frac{D\times I_L}{2} \tag{14}$$

where I_L is the peak current of inductor, and it can be expressed as below:

$$I_L=\frac{DT\times U}{L} \tag{15}$$

Substituting (14) into (15), thus, the average current can be calculated as follows:

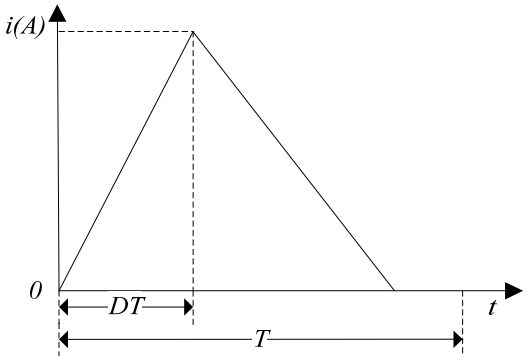

Figure 7. Working curve of inductor current

$$I_{avg}=\frac{D^2\times T\times U}{2\times L} \tag{16}$$

From what has been analyzed, it is considered that the average current of the inductor is also the equalizing current of active voltage equalization circuit. According to the principle of voltage equalization of supercapacitors, if the high-voltage supercapacitors release the average current I_{avg} more than the equalizing current I_{eq}, the voltage equalization can be realized. In order to increase the voltage equalizing speed, select the coefficient $k_j \ge 0.2$, then $I_{avg}\ge 0.2\times I$, and substituting this in Equation into (16), the inductor L can be obtained as follows:

$$L\le\frac{D^2\times T\times U}{0.4\times I} \tag{17}$$

In the circuit design, once the energy storage inductor L is selected, there are two ways to adjust the switching period:

1) Selecting the fixed switching period T, the equalizing current will be restrained by the limited cell voltage U in the process of charging and discharging, which makes it as a function of the voltage U;

2) The switching period T changes with the voltage U, which makes balancing current become a fixed value.

4.1.3 Voltage Equalization Control Strategy

Measuring two supercapacitors voltage U_m and U_{m+1}, the voltage difference can be calculated by the Equation $\Delta U_m=U_m-U_{m+1}$, and comparing the difference with the reference voltage U_{ref}, if $\Delta U_m \ge U_{ref}$, then the voltage Equalization circuit begins to work; if $\Delta U_m \le U_{ref}$, then the voltage equalization circuit stops working. In fact, if make all the supercapacitors reach the voltage equalization, every adjacent two supercapacitors will be parallel connected with a Buck-Boost converter, the voltage equalization controller generates different diving signals by analyzing all the measured supercapacitors

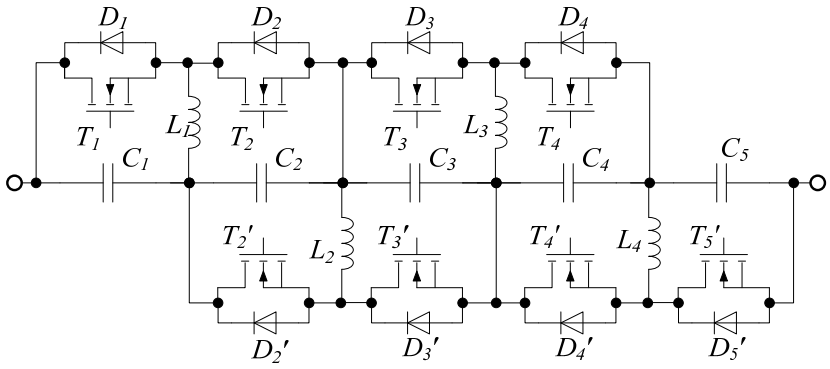

Figure 8. Active circuit of voltages balance for five superca-pacitors series

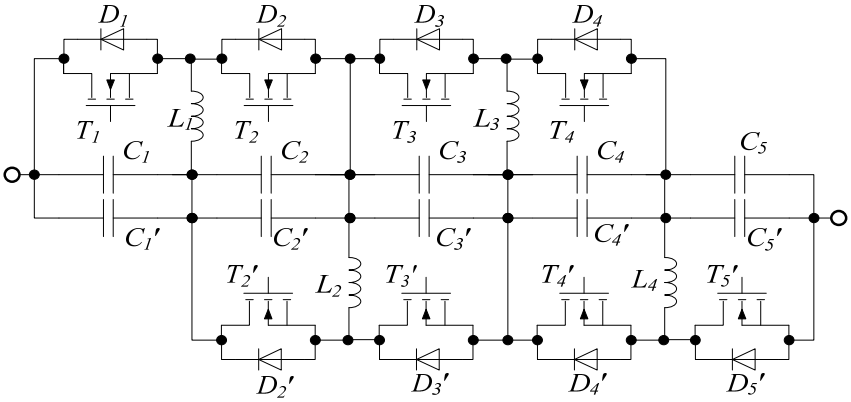

Figure 9. Active circuit of voltages balance for ten supercapacitors

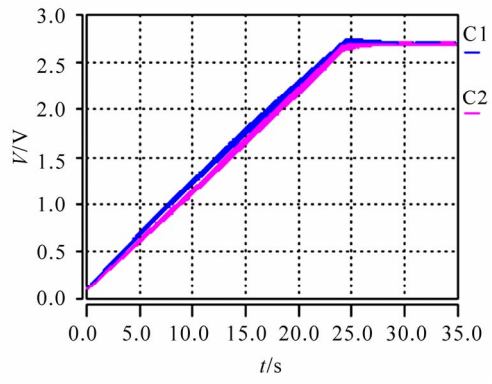

Figure 10. Simulation results of voltages balance for super-capacitors

voltage to drive MOSFET, in this way, equalization among all supercapacitors will be achieved at last.

4.2 The Extension Circuit of Voltage Equalization

Extending the above circuit, we can make it suitable for more series supercapacitor cells to meet the requirement of the RTG energy saving system. As is shown in Figure 8, we can see every two adjacent supercapacitors constitute a group which is controlled to balance voltage by a Buck-Boost converter. For example, the converter, which is composed of T_1, D_1, T_2 and D_2, balances the voltages between C_1 and C_2, and another one is composed of T_2, D_2, T_3' and D_3', balances the voltages between C_2 and C_3.The principle of equalization among C_3, C_4 and C_5 is the same as the above [5].

Considering the demand of hundreds of supercapacitor cells in RTG energy saving system, the series structure, as shown in Figure 8, makes the control components increase markedly and the control circuit become complicated. So the series and parallel structure in Figure 9, can be adopted in practical application.

4.3 Saber Simulation Analysis

In order to verify the character of the active voltage balance circuit in the energy recycling RTG system, we research the circuit composed of two supercapacitor cells in series module by the simulation study of Saber. Assume that the capacitance of one supercapacitor is

800F and the other one is 1000F, the constant charging current is 100A, the rate voltage of the supercapacitor is 2.7 V, the energy storage inductor is 1.36uH and the switching frequency is 10 kHz.

Figure 10 describes the process of charging two supercapacitors. It can be seen, at the end of the process, that the voltages of two supercapacitors become the same, no over-voltage. The result of Saber simulation indicates that active voltage balance circuit amends the inconsistency of the supercapacitor voltage greatly.

5. Conclusions

The active voltage equalization circuit based on the reversible Buck-Boost converter has been discussed in this paper. Theoretical analysis and simulation result show that the active control circuit can better solve the problem of the partial over-voltage over the supercapacitor groups. This method can be applied in the situation of higher charging or discharging current. Therefore, it has a high value to be used in the RTG energy saving system.

REFERENCES

[1] M. Okamura, "A basic study on power storage systems (translation of Japanese paper by the author with updating comments),"Journal Electrical Engineering in Japan, Vol.115, No.3, pp. 40–51, 1996.

[2] J. Zhao, J. C. Jiang, and L. Y. Niu, "A novel charge equalization technique for electric vehicle battery system," The Fifth International Conference on Power Electronics and Drive Systems, Singapore, 2003.

[3] S. W. Moore and P. J. Schneider, "A review of cell equalization methods for lithiumion and lithium polymer battery systems," SAE Technical Paper Series, pp. 1–5, 2001.

[4] H. D. Li, Z. Y. Feng, and Z. P. Qi, "Study on a fast voltage balancing for supercapacitors," Chinese Journal of Power Sources, Vol. 37, No. 3, pp. 186–189, 2007.

[5] A. Rufer and P. Barrade, "A supercapacitor-based energy-storage system for elevators with soft commutated interface," IEEE Transactions on Industry Applications, Vol. 38, No. 5, pp. 1151–1159, 2002.

Energy and Power Engineering, **2010, 31-38**
doi:10.4236/epe.2010.21006 Published Online February 2010 (http://www.scirp.org/journal/epe)

Amphiphilic Poly (3-Hydroxy Alkanoate)s: Potential Candidates for Medical Applications

Baki HAZER
Department of Chemistry, Zonguldak Karaelmas University, Zonguldak, Turkey
Email: bkhazer@karaelmas.edu.tr

Abstract: Poly (3-hydroxy alkanoate)s, PHAs, have been very attractive as biomaterials due to their biodegradability and biocompatibility. These hydrophobic natural polyesters, PHAs, need to have hydrophilic character particularly for drug delivery systems. In this manner, poly (ethylene glycol) (PEG) and hydrophilic functional groups such as amine, hydroxyl, carboxyl and sulfonic acid have been introduced into the PHAs in order to obtain amphiphilic polymers. This review involves in the synthesis and characterization of the amphiphilic PHAs.

Keywords: poly (3-hydroxy alkanoate), PHA, amphiphilic polymer, biomaterial, chemical modification

1. Introduction

Biomaterials have been widely used in medical applications, such as drug delivery, tissue engineering, device-based therapies and medical imaging [1,2]. Synthetic and naturally occurring polymers have played important role in the treatment of disease and the improvement of health care. Among them, PHAs are promising materials for biomedical applications in tissue engineering and drug delivery system because they are natural, renewable, biodegradable and biocompatible thermoplastics. PHAs have been used to develop devices, including sutures, nerve repair devices, repair patches, slings, cardiovascular patches, orthopedic pins, adhesion barriers stents, guided tissue repair/regeneration devices, articular cartilage repair devices, nerve guides, tendon repair devices, bone-marrow scaffolds, tissue engineered cardiovascular devices and wound dressing. However the direct use these polyesters has been hampered by their hydrophobic character and some physical shortcomings [3]. The key to biocompatibility of biomedical implanttable materials is to render their surface in a way that minimizes hydrophobic interaction with the surrounding tissue. Therefore, hydrophilic groups have been introduced into the PHAs in order to obtain amphiphilic polymer. This review has been focused on the chemically modified PHAs enhanced hydrophilic character as biomaterials for medical applications.

2. PHAs

PHAs are accumulated as intracellular granules as a result of a metabolic stress upon imbalanced growth due to a limited supply of an essential nutrient and the presence of an excess of a carbon source. These novel biopolymers have material properties ranging from rigid and highly crystalline to flexible, rather amorphous and elastomeric. There have been many studies reported on the modification reactions to enhance mechanical and thermal properties to prepare new biomaterials for the medical applications [4–13]. PHAs can be classified into three groups based on the number of carbon atoms in the monomer units: short-chain-length (*scl*PHA) containing 3–5 carbon atoms that are produced by *Ralstonia eutropha* (also referred *Watersia eutropha, A. Eutrophus*), medium-chain-length (*mcl*PHA) containing 6-14 carbon atoms, and long-chain-length (*lcl*PHAs), with more than 14 carbon atoms [14,15]. *Pseudomonas oleovorans* is a very versatile for PHA production because it can produce medium chain length polyesters (*mcl*PHA) and long chain length polyesters (*lcl*PHA) from a wide variety of carbon substrates. These types of the bacterial polyesters have been summarized in Table 1.

3. Amphiphilic PHAs

Amphiphilic polymers can be synthesized by introducing hydrophilic groups such as hydroxyl, carboxyl, amine, glycol and hydrophilic polymers such as PEG, poly (vinyl alcohol), polyacryl amide, poly acrylic acids, hydroxy ethyl methacrylate, poly vinyl pyridine and poly vinyl pyrrolidone to a hydrophobic moiety. Because of their ability to form micelles, amphiphilic block copolymers are strong candidates for potential applications as emulsifiers, dispersants, foamers, thickeners, rinse aids, and compatibilizers [16,17]. Similarly, amphiphilic PHAs can also be synthesized by introducing hydrophilic groups such as hydroxyl, carboxyl, amine,

Table 1. Classification of the bacterial polyesters

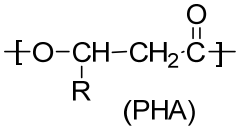

(PHA)

Carbon Source	Poly (3-hydroxy alkanoate) (PHA)			Thermal and Mechanical Properties		
	Type	Side chain (R)	Name*	T_g (°C)	T_m (°C)	Elongation (%)
Sugar, glucose, acetic acid	Short chain length	Methyl, ethyl	PHB PHV	15	170	5
Alkanoic acids, alkanes and alkanols	Medium chain length	Propyl, butyl, pentyl, hexyl, heptyl	PHHx PHHp PHO PHN PHD	-40	60	800
Plant oily acids	Long chain length	More than 14 Carbon per repeating unit		-50	40	Soft, sticky

*B: butyrate, V: valerate, Hx: hexanoate, Hp: heptenoate, O: octanoate, N: nonanoate, D: decanoate. T_g and T_m are glass and melting temperatures, respectively.

sulfonic acid, ethylene glycol and PEG. PEG is a polyether that is known for its exceptional blood and tissue compatibility. It is used extensively as biomaterial in a variety of drug delivery vehicles and is also under investtigation as surface coating for biomedical implants. PEG, when dissolved in water, has a low interfacial free energy and exhibits rapid chain motion, and its large excluded volume leads to steric repulsion of approaching molecules [18]. These properties make PEG excellent biocompatible material. Hydroxylation of the PHAs can be carried out by using both biosynthetically and chemical modification. The biosynthetic hydroxylation of the PHAs has successfully been reviewed by Foster, recently [19].

Chemical modifications of the PHAs have been extensively studied [6,9,15,20,21]. In this review, selective chemical modification reactions in order to obtain amphiphilic PHAs and some potential applications in biotechnology will be discussed.

4. Synthesis of Amphiphilic PHAs

Selective chemical modification of the PHAs involves functionalization and grafting reactions of the PHAs. Hydrophilic groups such as hydroxyl, carboxyl, amine, glycol and sulfonic acid can be introduced into the PHAs by means of functionalization. In grafting reactions, some hydrophilic groups have been attached in the PHA chain to obtain amphiphilic polymer.

4.1 Trans Esterification

Some ester group(s) of the PHA is exchanged with an alcohol in transesterification process. Transesterification is carried out in melt or in solution. Hydroxylation of the PHBs via chemical modification is usually achieved by the transesterification reactions to obtain diol ended PHB. Transesterification reactions in the melt between poly (ethylene glycol), mPEG, and PHB yield diblock amphiphilic copolymer with a dramatic decrease in molecular weight [22]. Catalyzed transesterification in the melt is used to produce diblock copolymers of poly ([*R*]-3-hydroxybutyric acid), PHB, and monomethoxy poly (ethylene glycol), mPEG, in the presence of a catalyst, in a one-step process. The formation of diblocks is accomplished by the nucleophilic attack from the hydroxyl end-group of the mPEG catalyzed by bis (2-ethylhexanoate) tin.

When the transesterification reaction between PHB and ethylene glycol in diglyme as a solvent is carried out, the telechelic PHB with MW at around 2000 Dalton is obtained [23]. Stannous octanoate as a transesterification catalyst causes the reaction of carboxylic end group and diol, quantitatively. Basically, short chain diol or polyol moiety can rarely renders a hydrophilic character to the longer hydrophobic PHA. Therefore amphiphilic character of the telechelic PHAs and PEGylated PHAs have been stood poor.

Telecehelic PHB obtained by this way can be used in the preparation of the polyester urethanes via diisocyanate chain extension reaction with synthetic aliphatic polyester as soft segment [24]. PHB-g-PCL graft copolyester urethane samples exhibited the elongation at break up to 900 %.

Two segmented biodegradable poly (ester-urethane) series, based on bacterial PHB as the hard segments, and either PCL or PBA as the soft segments, were easily

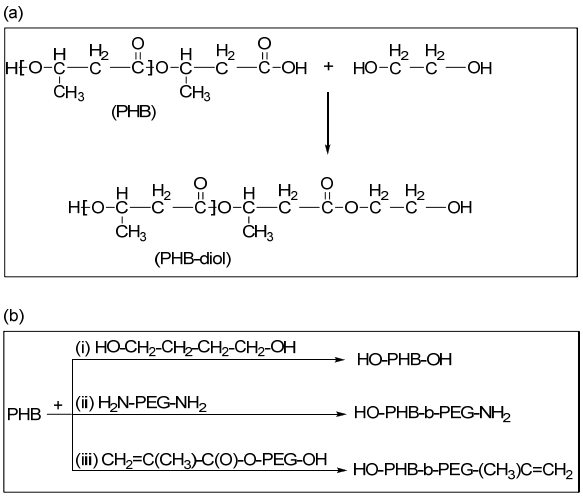

Figure 1. (a) Formation of the diol ended PHB via transesterification in the presence of ethylene glycol. (b) Transesterification reactions of PHB with (i) butane diol, (ii) transamidation with bisaminopropyl ended PEG, and (iii) transesterification reactions of PHB with methacryloyl oxy ethylene glycol in solution

synthesized by one-step solution polymerizations. Transesterification reaction of PHB with methacryloyl oxy poly (ethylene glycol) (MW: 526), poly (ethylene glycol) bis (2-aminopropyl ether) with MW 1000 and 2000 was achieved to obtain PHB-b-PEG telechelic diblock copolymers [25]. Similarly, telechelic PHB can also be obtained by transesterification with 1,4-butane diol in 1,2-dichloro benzene under reflux conditions. The transesterification reactions can be designed in Figure 1.

4.2 Oxidation of the Pendant Double Bonds

Most used unsaturated PHAs are mclPHAs obtained from unsaturated edible oils and synthetic olefinic substrates. When Pseudomonas oleovorans is grown on unsaturated carbon source such as soybean oily acids, 7-octenoic acid and 10-undecenoic acid, unsaturated PHAs are obtained [26]. Figure 2 shows the synthesis of the unsaturated PHAs.

Microbial polyesters containing unsaturated side chains are open the way for chemical modification reactions to prepare PHA derivatives. Pendent double bonds of the poly (3-hydroxy octanoate-co-10-undecenoate), PH(O)U, can be oxidized to the diol (PHOU-diol) and carboxylic acid (PHOU-COOH). $KMnO_4$ is used as an oxidizing agent. In mild conditions PHOU-diol is obtained [27]. While PHOU was insoluble in a polar solvent, PHOU-diol was soluble in methanol, acetone/water (80/20, v/v) and DMSO, even with 40–60% of double bonds unconverted, but it was insoluble in non-polar solvents such as chloroform, THF, acetone. Figure 3 shows the PHOU-diol.

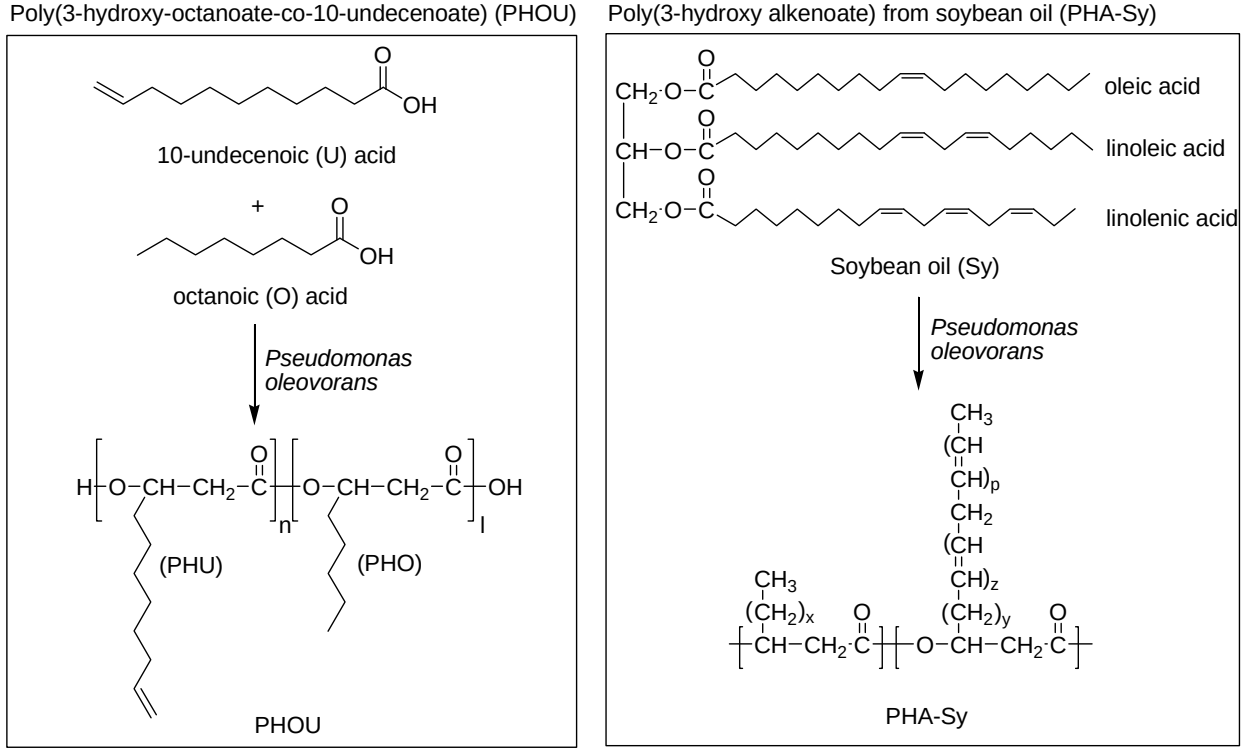

Figure 2. Synthesis of two types of unsaturated PHAs from *Pseudomonas oleovorans (i)* grown on soybean (PHA-Sy) and *(ii)* 10-undecenoic acid and octanoic acid (PHOU)

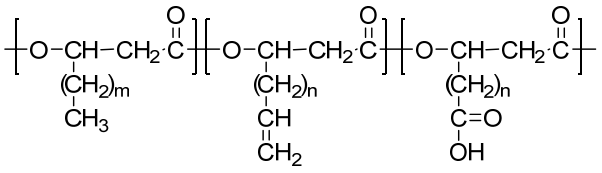

Figure 3. PHOU with pendant hydroxyl groups

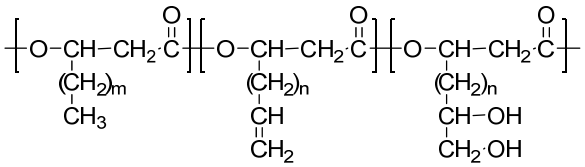

Figure 4. PHOU with pendant carboxylic acids (PHOU-COOH)

The use of $NaHCO_3$ even in hot solution (55℃) resulted mainly in diol groups, not carboxylic groups, while the same reaction at room temperature using $KHCO_3$, led to the conversion of the pendant unsaturated groups to the carboxyl groups [28]. Figure 4 shows the PHOU with pendant carboxyl groups.

Carboxylation of PHOU using OsO_4 as oxidant can be performed with the small decrease in MW after the reaction [29]. The quantitative hydroxylation of pendant vinyl groups of PHU with the use of either the borobicyclononane or the borane−tetrahydrofuran complex is also achieved in high yield [30]. After hydroxylation, the thermal stability and the molecular weight of the hydroxylated PHU showed small decreases; however, full solubility in methanol and almost full solubility in water are achieved [30].

Water wettability of saturated PHAs, poly(3-hydroxy butyrate) (PHB) and poly(3-hydroxy butyrate-co-3-hydroxy hexanoate) (PHBHHx) can also be improved by carboxyl ion implantation. Ion implantation is performed at an energy of 150 keV with fluences ranging from $5x10^{12}$ to $1x10^{15}$ ions/cm^2. Contact angle measurements are confirmed that the ion implantation improves the water wettability [31].

Epoxidation of the unsaturated polyester with m-chloroperbenzoic acid, as a chemical reagent, yields to quantitative conversions of the unsaturated groups into epoxy groups [32]. Primary and secondary amines can be reacted with epoxide groups to yield hydrophilic compounds.

Reaction between hexamethylene diamine with epoxidized PHOU provides crosslinked polyester [33].

Enhenced hydrophilicity of the PHOU has recently been achieved by the reaction between epoxidized PHOU and diethanol amine to give highly hydrophilic polyester, PHON [34]. The first reaction involved the transformation of the vinyl-terminated side chains of PHOU to epoxide groups (PHOE). Figure 5 shows to the conversion reaction of epoxidized PHOU (PHOE) to hydroxylated PHOU in the presence of diethanol amine (PHON).

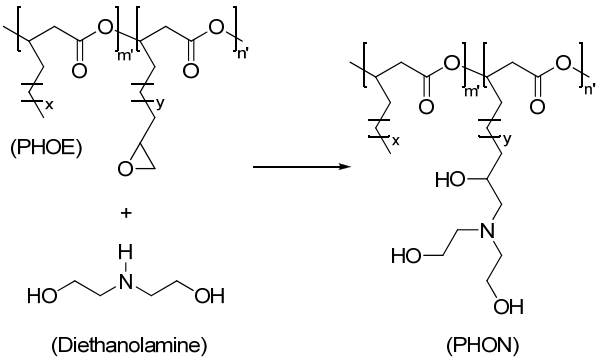

Figure 5. The conversion reaction of epoxidized-PHOU (PHOE) to hydroxylated PHOU in the presence of diethanol amine (PHON)

The successful side chain conversion was further substantiated by the change in solubility when converting PHOU to PHOE to PHON. As the functionalized side chains became more polar, the polymer became soluble in more polar solvents. In this respect, PHON was soluble in water.

4.3 Quarternization and Sulfonation of the PHAs

Halogenation of the polymers is a versatile method to open the way for further functionalization [25,35,36]. Addition of the chlorine and bromine into the double bond is quantitative and halogenated PHAs can be easily obtained by this way [25]. Chlorination is performed by either the addition to double bonds of the unsaturated PHA obtained from soybean oil (PHA-Sy) or substitution reactions with saturated hydrocarbon groups [35,36]. Chlorination of the sticky, soft PHA-Sy with double bond provides polyester with hard, brittle, and crystalline physical properties depending on the chlorine content. By this way, it is possible to introduce 35 wt% chlorine to the PHA. In case of the chlorinated PHO, glass transition temperature has been shifted to +2℃ from –40 ℃ [36]. For further functionalization, quaternization reactions of the chlorinated PHA with triethylamine (or triethanol amine) can be performed. Additionally, aqueous solution of $Na_2S_2O_3{\cdot}5H_2O$ can be reacted with solution of PHA-Cl in acetone to give sulfonate derivative of the PHO [36].

4.4 Grafting Reactions of the PHAs

4.4.1 Chitosan Grafting

Chemical modifications of chitosan by grafting method are important to prepare multifunctional materials in different fields of application and to improve its chemical, physical, and mechanical properties [37]. Chitosan-g-PHBV graft copolymer was synthesized and grafting of linoleic acid on chitosan were performed by condensation reaction under vacuum at 90–95℃. Graft

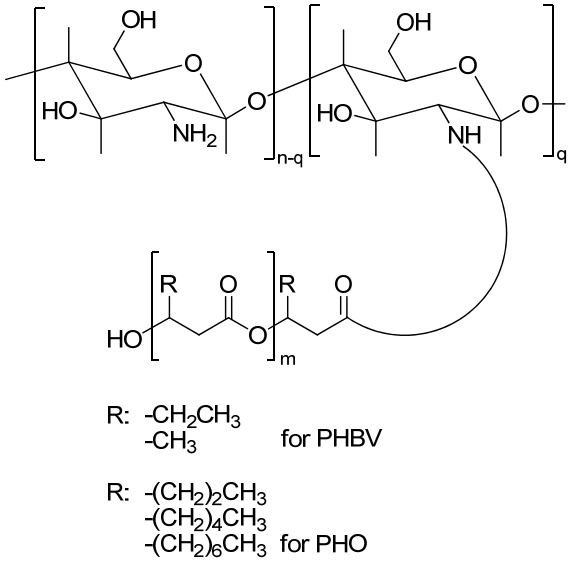

Figure 6. Chitosan-g-PHBV graft copolymer

copolymers exhibit different solubility behavior as a function of degree of substitution of NH_2 in other words as a function of grafting percent such as solubility, insolubility, or swelling in 2 wt % acetic acid and in water while chitosan does not swell in water. Chitosan-g-PHBV graft copolymer is shown in Figure 6.

4.4.2 Sugar Grafting

Glycopolymers are emerging as a novel class of neoglycoconjugates useful for biological studies and they are prepared either by copolymerization or grafting methods [38]. Since it has been shown that thiosugars are potent tools in glycobiology, 1-thiomaltose derivatives has been grafted onto PHAs in two ways [39]; the thiol sugar is added to the double bond and the reaction between thiol sugar and bromo end groups of polyester biosynthesized from 11-bromoundecanoic acid [40]. These new grafted polymers are insoluble in dichloromethane and chloroform, but very soluble in *N*,*N*-dimethylformamide and dimethyl sulfoxide, as opposed to their parent PHAs. As expected, modified PHAs are more hydrophilic than their parent compounds.

4.4.3 PEG Grafting

Diazo linkaged PEG, a polyazoester synthesized by the reaction of PEG and 4,4'-azobis(4-cyanopentanoyl chloride) creates PEG macro radicals which is easily attack to the double bonds of the unsaturated PHA to obtain the poly(3-hydroxyalkanoate)-*g*-poly(ethylene glycol) crosslinked graft copolymers [41]. Poly(3-hydroxyalkanoate)s containing double bonds in the side chain (PHA-DB) were obtained by co-feeding *Pseudomonas oleovorans* with a mixture of nonanoic acid and anchovy (hamci) oily acid (in weight ratios of 50/50 and 70/30). PHA-DB was thermally grafted with a [41].

Graft copolymers of the saturated mclPHAs can be synthesized by using macro radicals via H-abstraction from the tertiary carbon of the polyester [42]. Similarily, macroradicals onto the PHAs are induced by the UV irradiation via H-abstraction in the presence of a PEG-macromonomer to prepare PEG-g-PHO graft copolymers [43]. Homogeneous solutions of poly (3-hydroxyoctanoate) (PHO) and the monoacrylate-poly (ethylene glycol) (PEGMA) monomer in chloroform were irradiated with UV light to obtain PEGMA-grafted PHO (PEGMA-*g*-PHO) copolymers. The results of the protein adsorption and platelet adhesion tests show that the blood compatibility was also enhanced by grafting the PEGMA chains. The adsorption of proteins and

Table 2. Methods for the synthesis of the amphiphilic PHAs

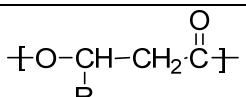

(PHA)

Carbon Source	Poly (3-hydroxy alkanoate) (PHA)			Thermal and Mechanical Properties		
	Type	Side chain (R)	Name*	T_g (°C)	T_m (°C)	Elongation (%)
Sugar, glucose, acetic acid	Short chain length	Methyl, ethyl	PHB PHV	15	170	5
Alkanoic acids, alkanes and alkanols	Medium chain length	Propyl, butyl, pentyl, hexyl, heptyl	PHHx PHHp PHO PHN PHD	-40	60	800
Plant oily acids	Long chain length	More than 14 Carbon per repeating unit		-50	40	Soft, sticky

*B: butyrate, V: valerate, Hx: hexanoate, Hp: heptenoate, O: octanoate, N: nonanoate, D: decanoate. T_g and T_m are glass and melting temperatures, respectively.

platelets was increasingly suppressed, as the DG of PEGMA onto PHO increased. Glycerol 1, 3-diglycerol diacrylate-grafted poly(3-hydroxyoctanoate) copolymers are also prepared by heating homogeneous solutions of PHO, diacrylate monomer and benzoyl peroxide initiator [44]. The resulting copolymers have enhanced thermal properties and mechanical strengths. The surfaces and the bulk of the graft copolymers became more hydrophilic as the diglycerol-diacrylate grafting density in the copolymer increased. Many studies have reported that hydrophilic surfaces, such as those of hydro gels and PEG-grafted polymers, suppress protein adsorption and platelet adhesion. The surfaces of these graft copolymers become more hydrophilic with grafted diglycerol groups. These surface characteristics make this graft copolymer to prevent protein adsorption and platelet adhesion very effectively. As a summary, Table 2 indicates the sum of the chemical modification reactions to obtain amphiphilic PHAs. In this manner, Renard *et al*. achieved the amphiphilic copolymer based on PHOU and PEG [45]. Carboxilic acid terminal groups in the side chains are reacted with PEG in the presence of dicyclohexyl carbamate at room temperature. Amphiphilic graft copolymer obtained is soluble in the mixture of H_2O/ acetone (80/20) whereas precursor PHOU is not soluble.

5. Conclusions

Microbial polyesters are biocompatible and biodegradable hydrophobic natural thermoplastics. Amphiphilic PHAs from swollen in water to soluble in water are much more desirable in the drug delivery system and tissue engineering. In most attempts to synthesize amphiphilic PHAs, degradation of the polyester chain has been unavoidable. To obtain new amphiphilic PHAs with high molecular weight and their medical applications have been attractive for scientists.

6. Acknowledgment

This work was financially supported by TUBITAK (grant no. 108T423) and ZKU Research Fund.

REFERENCES

[1] R. Langer and D. A. Tirrell, "Designing materials for biology and medicine," Nature, No. 428, pp. 487–492, 2004.

[2] S. Mitragotri and J. Lahann, "Physical approaches to biomaterial design," Nature Mater, No. 8, pp. 15–23, 2009.

[3] S. P. Valappil, S. K. Misra, A. R. Boccaccini, and I. Roy, "Biomedical applications of polyhydroxyalkanoates, an overview of animal testing and in vivo responses," Expert Review of Medical Devices, No. 3, pp. 853–868, 2006.

[4] A. J. Anderson and E. A. Dawes, "Occurrence, metabolism, metabolic role, and industrial uses of bacterial polyhydroxyalkanoates," Microbiological Reviews, No. 54, pp. 450–472, 1990.

[5] R. W. Lenz and R. H. Marchessault, "Bacterial polyesters: Biosynthesis, biodegradable plastics and biotechnology," Biomacromolecules, No. 6, pp. 1–8, 2005.

[6] B. Hazer and A. Steinbüchel, "Increased diversification of polyhydroxyalkanoates by modification reactions for industrial and medical applications," Applied Microbiology and Biotechnology, No. 74, pp. 1–12, 2007.

[7] K. Sudesh, H. Abe, and Y. Doi, "Synthesis, structure and properties of polyhydroxy alkanoates: Biological polyesters," Progress in Polymer Science, No. 25, pp. 1503–1555, 2000.

[8] A. Steinbüchel and B. Füchtenbusch, "Bacterial and other biological systems for polyester production," Trends in Biotechnology, No. 16, pp. 419–427, 1998.

[9] D. Y. Kim, H. W. Kim, M. G. Chung, and Y. H. Rhee, "Biosynthesis, modification, and biodegradation of bacterial medium-chain-length polyhydroxyalkanoates," Journal of Microbiology, No. 45, pp. 87–97, 2007.

[10] R. H. Marchessault, "Polyhydroxyalkanoate (PHA) history at Syracuse University and beyond cellulose," Cellulose, No. 16, pp. 357–359, 2009.

[11] W. Orts, G. Nobes, J. Kawada, S. Nguyen, G. Yu, and F. Ravenelle, "Poly (hydroxyalkanoates): Biorefinery polymers with a whole range of applications, the work of Robert H. Marchessault," Canadian Journal of Chemistry, No. 86, pp. 628–640, 2008.

[12] M. Zinn, B. Witholt, and T. Egli, "Occurrence, synthesis and medical application of bacterial polyhydroxyalkanoate," Advanced Drug Delivery Reviews, No. 53, pp. 5–21, 2001.

[13] Q. Wu, Y. Wang, and G. Q. Chen, "Medical application of microbial biopolyesters polyhydroxyalkanoates," Artificial Cells Blood Substitutes and Biotechnol, No. 37, pp. 1–12, 2009.

[14] K. Ruth, G. de Roo, T. Egli, and Q. Ren, "Identification of two acyl-CoA synthetases from Pseudomonas putida GPo1: One is located at the surface of polyhydroxyalkanoates granules," Biomacromolecules, No. 9, pp. 1652–1659, 2008.

[15] A. Steinbuchel and H. E. Valentin, "Diversity of bacterial polyhydroxyalkanoic acids," FEMS Microbiology Letters, No. 128, pp. 219–228, 1995.

[16] S. Förster and M. Antonietti, "Amphiphilic block copolymers in structure-controlled nanomaterial hybrids," Advanced Materials, No. 10, pp. 195–217, 1998.

[17] N. Hadjichristidis, M. Pitsikalis, S. Pispas, and H. Iatrou, "Polymers with complex architecture by living anionic polymerization," Chemical Reviews, No. 101, pp. 3747–3792, 2001.

[18] K. J. Townsend, K. Busse, J. Kressler, and C. Scholz, "Contact angle, WAXS, and SAXS analysis of poly (3-hydroxybutyrate) and poly (ethylene glycol) block copolymers obtained via azotobacter vinelandii UWD,"

Biotechnology Progress, No. 21, pp. 959–964, 2005.

[19] L. J. R. Foster, "Biosynthesis, properties and potential of natural–synthetic hybrids of polyhydroxyalkanoates and polyethylene glycols," Applied Microbiology and Biotechnology, No. 75, pp. 1241–1247, 2007.

[20] B. Hazer, "Chemical modification of synthetic and biosynthetic polyesters," in Biopolymers (Editor: A. Steinbuchel), Vol. 10, Chapter 6, pp. 181–208, Wiley-VCH, Weinheim, 2003.

[21] (a) S. Ilter, B. Hazer, M. Borcaklı, and O. Atıcı, "Graft copolymerisation of methyl methacrylate onto a bacterial polyester containing unsaturated side chains," Macromolecular Chemistry and Physics, No. 202, pp. 2281–2286, 2001. (b) B. Hazer, "Chemical modification of bacterial polyester," Current Trends in Polymer Science, No. 7, pp. 131–138, 2002. (c) B. Cakmakli, B. Hazer, and M. Borcakli, "Poly (styrene peroxide) and poly(methyl methacrylate peroxide) for grafting on unsaturated bacterial polyesters," Macromolecular Bioscience, No. 1, pp. 348–354, 2001. (d) B. Hazer, "Poly (beta-hydroxynonanoate) and polystyrene or poly (methyl methacrylate) graft copolymers: Microstructure characteristics and mechanical and thermal behavior," Macromolecular Chemistry and Physics, No. 197, pp. 431–441, 1996.

[22] F. Ravenelle and R. H. Marchessault, "One-step synthesis of amphiphilic diblock copolymers from bacterial poly ([R]-3-hydroxybutyric acid)," Biomacromolecules, No. 3, pp. 1057–1064, 2002.

[23] T. D. Hirt, P. Neuenschwander, and U. W. Suter, "Telechelic diols from poly [(R)-3-hydroxybutyric acid] and poly ([(R)-3-hydroxybutyricacid]-co-[(R)-3-hydroxyvalericacid]," Macromolecular Chemistry and Physics, No. 197, pp. 1609–1614, 1996.

[24] (a) G. R. Saad, "Calorimetric and dielectric study of the segmented biodegradable poly (ester-urethane)s based on bacterial poly [(R)-3-hydroxybutyrate]," Macromolecular Bioscience, No. 1, pp. 387–396, 2001. (b) G. R. Saad, Y. J. Lee, and H. Seliger, "Synthesis and characterization of biodegradable poly (ester-urethanes) based on bacterial poly (R-3-hydroxybutyrate)," Journal of Applied Polymer Science, No. 83, pp. 703–718, 2002.

[25] H. Erduranlı, B. Hazer, and M. Borcaklı, "Post polymerization of saturated and unsaturated poly (3-hydroxy alkanoate)s," Macromolecular Symposia, No. 269, pp. 161–169, 2008.

[26] (a) B. Hazer, O. Torul, M. Borcaklı, R. W. Lenz, R. C. Fuller, and S. D. Goodwin, "Bacterial production of polyesters from free fatty acids obtained from natural oils by Pseudomonas Oleovorans," Journal of Environmental Polymer Degradation, No. 6, pp. 109–113, 1998. (b) R. D. Ashby and T. A. Foglia, "Poly (hydroxyalkanoate) biosynthesis from triglyceride substrates," Applied Microbiology and Biotechnology, No. 49, pp. 431–437, 1998. (c) K. Fritzsche, R. W. Lenz, and R. C. Fuller, "Production of unsaturated polyesters by Pseudomonas oleovorans," International Journal of Biological Macromolecules, No. 12, pp. 85–91, 1990. (d) Y. B. Kim, R. W. Lenz, and R. C. Fuller, "Poly-3-Hydroxyalkanoates containing unsaturated repeating units produced by pseudomonas oleovorans," Journal of Polymer Science Part A: Polymer Chemistry, No. 33, pp. 1367–1374, 1995.

[27] M. Y. Lee, W. H. Park, and R. W. Lenz, "Hydrophilic bacterial polyesters modified with pendant hydroxyl groups," Polymer, No. 41, pp. 703–1709, 2000.

[28] M. Y. Lee and W. H. Park, "Preparation of bacterial copolyesters with improvedhydrophilicity by carboxylation," Macromolecular Chemistry and Physics, No. 201, pp. 2771–2774, 2000.

[29] D. J. Stigers and G. N. Tew, "Poly (3-hydroxyalkanoate)s functionalized with carboxylic acid Groups in the side chain," Biomacromolecules, No. 4, pp. 193–195, 2003.

[30] (a) M. S. Eroglu, B. Hazer, T. Ozturk, and T. Caykara, "Hydroxylation of pendant vinyl groups of poly (3-hydroxy undec-10-enoate) in high yield," Journal of Applied Polymer Science, No. 97, pp. 2132–2139, 2005. (b) E. Renard, A. Poux, L. Timbart, V. Langlois, and P. Guérin, "Preparation of a novel artificial bacterial polyester modified with pendant hydroxyl groups," Biomacromolecules, No. 6, pp. 891–896, 2005.

[31] D. M. Zhang, F. Z. Cui, Z. S. Luo, Y. B. Lin, K. Zhao, and G. Q. Chen, "Wettability improvement of bacterial polyhydroxyalkanoates via ion implantation," Surface and Coatings Technology, No. 131, pp. 350–354, 2000.

[32] M. Bear, M. Leboucher-Durand, V. Langlois, R. W. Lenz, S. Goodwin, and P. Guerin, "Bacterial poly-3-hydroxyalkenoates with epoxy groups in the side chains," Reactive and Functional Polymers, No. 34, pp. 65–77, 1997.

[33] M. Y. Lee, S. Y. Cha, and W. H. Park, "Crosslinking of microbial copolyesters with pendant epoxide groups by daimine," Polymer, No. 40, pp. 3787–3793, 1999.

[34] J. Sparks and C. Scholz, "Synthesis and Characterization of a Cationic Poly (-hydroxyalkanoate)," Biomacromolecules, No. 9, pp. 2091–2096, 2008.

[35] A. H. Arkin, B. Hazer, and M. Borcakli, "Chlorination of poly-3-hydroxy alkanoates containing unsaturated side chains," Macromolecules, No. 33, pp. 3219–3223, 2000.

[36] A. H. Arkin and B. Hazer, "Chemical modification of chlorinated microbial polyesters," Biomacromolecules, No. 3, pp. 1327–1335, 2002.

[37] (a) G. Yu, F. G. Morin, G. A. R. Nobes, and R. H. Marchessault, "Degree of acetylation of chitin and extent of grafting PHB on chitosan determined by solid state 15N NMR," Macromolecules, No. 32, pp. 518–520, 1999. (b) H. Arslan, B. Hazer, and S. C. Yoon, "Grafting of poly (3-hydroxyalkanoate) and linoleic acid onto chitosan," Journal of Applied Polymer Science, No. 103, pp. 81–89, 2007.

[38] S. Muthukrishnan, G. Jutz, X. Andre´, H. Mori, and A. H. E. Müller, "Synthesis of hyperbranched glycopolymers via self-condensing atom transfer radical copolymerization of a sugar-carrying acrylate," Macromolecules, No. 38, pp. 9–18, 2005.

[39] M. Constantin, C. I. Simionescu, A. Carpov, E. Samain, and H. Driguez, "Chemical modification of poly (hydroxyalkanoates), copolymers bearing pendant sugars,"

Macromolecular Rapid Communications, No. 20, pp. 91–94, 1999.

[40] Y. B. Kim, R. W. Lenz, and R. C. Fuller, "Poly (β-hydroxyalkanoate) copolymers containing brominated repeating units produced by Pseudomonas oleovorans," Macromolecules, No. 25, pp. 1852–1857, 1992.

[41] B. Hazer, R. W. Lenz, B. Çakmaklı, M. Borcaklı, and H. Koçer, "Preparation of poly (ethylene glycol) grafted poly (3-hydroxyalkanoate)s," Macromolecular Chemistry and Physics, No. 200, pp. 1903–1907, 1999.

[42] (a) B. Hazer, "Poly (*β*-hydroxy nonanoate) and polystyrene or poly (methyl methacrylate) graft copolymers: Microstructure characteristics and mechanical and thermal behavior," Macromolecular Chemistry and Physics, No. 197, pp. 431–441, 1996. (b) S. Ilter, B. Hazer, M. Borcakli, and O. Atici, "Graft copolymerization of methyl methacrylate onto bacterial polyester containing unsaturated side chains," Macromolecular Chemistry and Physics, No. 202, pp. 2281–2286, 2001.

[43] (a) H. W. Kim, C. W. Chung, and Y. H. Rhee, "UV-induced graft copolymerization of monoacrylate-poly(ethylene glycol) onto poly(3-hydroxyoctanoate) to reduce protein adsorption and platelet adhesion," International Journal of Biological Macromolecules, No. 35, pp. 47–53, 2005. (b) C.W. Chung, H. W. Kim, Y. B. Kim, and Y. H. Rhee, "Poly (ethylene glycol)-grafted poly (3-hydroxyundecenoate) networks for enhanced blood compatibility," International Journal of Biological Macromolecules, No. 32, pp. 17–22, 2003.

[44] H. W. Kim, M. G. Chung, Y. B. Kim, and Y. H. Rhee, "Graft copolymerization of glycerol 1,3-diglycerolate diacrylate onto poly(3-hydroxyoctanoate) to improve physical properties and biocompatibility," International Journal of Biological Macromolecules, No. 43, pp. 307–313, 2008.

[45] S. Domenek, V. Langlois, and E. Renard, "Bacterial polyesters grafted with poly (ethylene glycol): Behaviour in aqueous media," Polymer Degradation and Stability, No. 92, pp. 1384–1392, 2007.

Energy and Power Engineering, **2010, 39-45**
doi:10.4236/epe.2010.21007 Published Online February 2010 (http://www.scirp.org/journal/epe)

Simulation of Electric Fields in Small Size Divertor Tokamak Plasma Edge

A. H. BEKHEIT
Plasma & Nuclear Fusion Department, Nuclear Research Centre, Atomic Energy Authority, Cairo, Egypt
Email: *amrbekheitga@yahoo.com*

Abstract: The fluid simulation of Small Size Divertor Tokamak (SSDT) plasma edge by the B2-SOLPS5.0 2D [1] transport code gives the following results: First, in the vicinity of separatrix the radial electric field result is not close to the neoclassical electric field. Second, the shear of radial electric field is independent on plasma parameters. Third, switching on poloidal drifts (E×B and diamagnetic drifts) leads to asymmetric parallel and poloidal fluxes from outer to inner plates and upper part of SOL for normal direction of toroidal magnetic field. Fourth, for the normal direction of toroidal magnetic, the radial electric field of SSDT is affected by the variation in temperature heating of plasma. Fifth, the parallel flux is directed from inner to outer plate in case of discharge without neutral beam injection (NBI).

Keywords: electric field, transport codes, divertor tokamak

1. Introduction

A regime of improved confinement is extremely important for the operation of a thermonuclear reactor. A transition from the low confinement (L-mode) to high confinement regime (H-mode) was discovered [2], and since then it has been observed on many tokamaks and stellarators. The L-H transition may be caused by a strong radial electric field at the edge plasma and suppression of the fluctuation level by strong poloidal rotation in the E×B fields [3,4]. As a result, the transport coefficients are strongly reduced in the H-mode and transport barriers with steep density and temperature gradients were formed near the separatrix or close flux surface. The key element in the transition physics is the origin of the strong radial electric field in the edge plasma. If the radial electric field is sufficiently strong, the poloidal $E\times B$ flow acquires a large shear, which is considered to be necessary for suppression of edge turbulence. The radial electric field in the separatrix vicinity is simulated by using the B2-SOLPS5.0 two dimensional fluid code [1], in which most complete system of transport equations is solved including all the important perpendicular current and E×B drifts for SSDT. This code differs from the similar fluid codes (e.g. codes [5,6]), since it included detail account of parallel viscosity and perpendicular current. The equation system provides a transition to the neoclassical equation when the anomalous transport coefficients are replaced by classical value. The simulation is performed for SSDT, where the plasma parameters in the separatrix vicinity and the Scrap Off Layer (SOL) correspond to Pfirch-Schlueter regime [7], thus justifying the applicability of the fluid equations. On the basis of simulation for different power of additional heating, plasma densities, toroidal rotation velocities and magnetic field directions, it is demonstrated that the radial electric field in the separatrix vicinity is not of the order of the neoclassical field. In this paper the shear of the poloidal E×B drifts is calculated. It is shown that the shear of the poloidal rotation is not function of plasma parameters.

2. Simultion Results

The computation region for simulation is based on Single Null (SN) magnetic divertor and covers the SOL, core and private regions as shown in Figure 1. In computation region the coordinate which vary in the direction along flux surfaces (x-coordinate or poloidal coordinate) and the coordinate which vary in the direction across flux surfaces (y-coordinate or radial coordinate). The computation mesh is divided into 24×96 units (where-1≤ $x \le 96$, $-1 \le y \le 24$) and the separatrix was at y=12. The simulations were performed for L-regimes of SSDT (minor radius a=0.1m, major radius R=0.3 m, I=50kA, B_T=1.7 T, electron density at equatorial midplane $n_e = n_i = n = 2 \times 10^{19}\ m^{-3}$, ion temperature T_i=31-93 eV).

The anomalous values of diffusion and heat conductivity coefficients were chosen: D=0.5 m^2s^{-1}, $\chi_{e,i}$ = 0.7 m^2s^{-1}. The perpendicular viscosity was taken in the form $\eta = nm_iD$. The inner boundary flux surface, was located in the core few cm from the separetrix, the boundary conditions for the density of plasma, the average toroidal momentum flux, the electron and ion

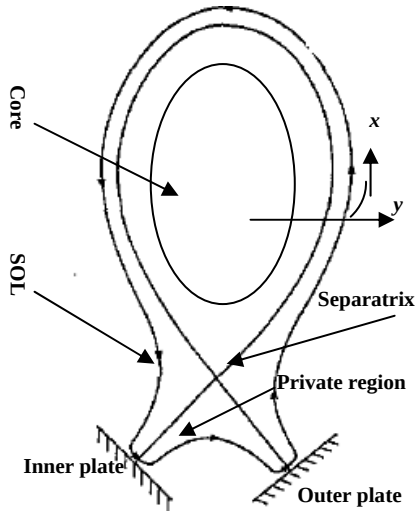

Figure 1. Coordinate system and simulation mesh

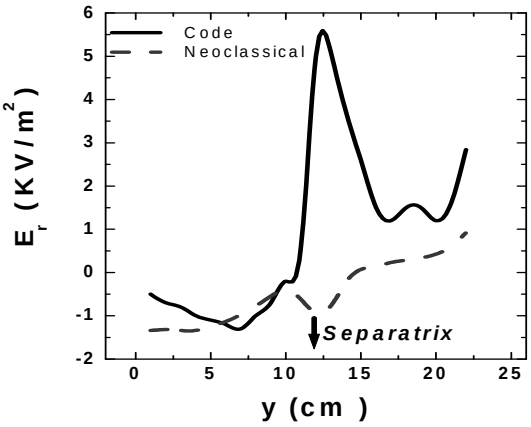

Figure 2. Radial electric field at edge of SSDT for discharge without neutral beam injection (NBI) at T_i = 31 e v, n_i = 4×10^{19}m^{-3}

heat fluxes were specified [8]. The first result of simulations for the radial electric field E_r was compared with the neoclassical electric field $E^{(NEO)}$ which is given by [7]:

$$E^{(NEO)} = \frac{T_i}{e}\left(\frac{1}{h_y}\frac{d\ln n}{dy} + k_T\frac{1}{h_y}\frac{d\ln T_i}{dy}\right) - b_x\frac{\oint\sqrt{g}V_{\|}B\,dx}{\oint\sqrt{g}\,dx} \quad (1)$$

where $b_x = B_x/B$ (B_x is poloidal magnetic field and $B=\sqrt{B_x^2+B_z^2}$ where B_z is toroidal magnetic fields), $\sqrt{g}=h_x h_y h_z$ is the metric coefficients, ($hx = 1/|\nabla x|$, $h_y = 1/|\nabla y|$, $h_z = 1/|\nabla z|$) $V_{||}$ is the parallel (toroidal) velocity (the coefficient k_T = 2.7 corresponds to the Pfirsch-Schlueter regime).Typical radial electric field is shown in Figure 2. The comparison is showed that in the vicinity of separatrix the radial electric field is not order of the neoclassical electric field for both discharges without neutral beam injection (NBI). This fact means that, the radial transport of toroidal (parallel) momentum is larger than parallel viscosity in parallel momentum balance equation [8]. It is worth to mention that the averaged parallel velocity in Equation (1) is determined by the radial transport of parallel (toroidal) momentum i.e. by anomalous values of the diffusion and perpen-dicular viscosity coefficients. The radial profiles of parallel velocity for different values of average velocity at the inner boundary are shown in Figure 3. Even in the Ohmic case the contribution from the last term in Equation (1) is not negligible and should take into account. The second result, the radial electric field calculate by the code is negative in core, vicinity of separatrix and is positive in SOL, Figures 2. For normal direction of toroidal magnetic field in SOL one can see that the $E_r \times B_T$ drifts are directed from outer plate to inner plate in SOL, and from inner plate to outer plate in the private region as shown

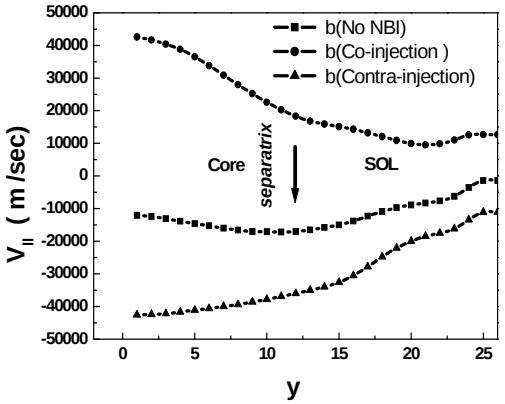

Figure 3. Parallel velocity for discharges with co and contra-injection neutral beam (NBI), for parameter of SSDT

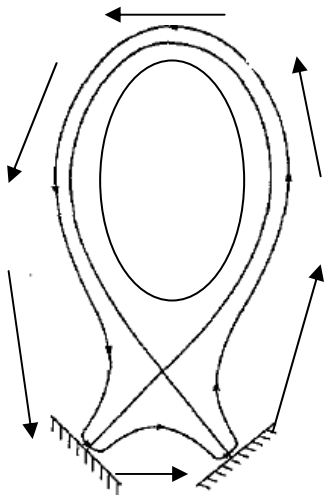

Figure 4. The arrows shows the direction of $E \times B$ drifts in the edge plasma of small size divertor tokamak

in Figure 4. Plasma rotates in the core in the direction opposite to that in the SOL, thus creating a shear near separatrix. The third result it has been found that radial electric field is affected by the variation in temperature of plasma heating (temperature heating of plasma given by $T_{heating} = 2 \times A_p \times \alpha$, where A_p surface plasma area = 1.53 for SSDT and α is constant given by code. For example, for $\alpha = 98.125$, $T_{heating} = 2 \times 1.53 \times 98.125 = 300.27$ eV) for SSDT as shown in Figure 5.Therefore, the increasing of the temperature heating of plasma causes a change in the structure of the edge radial electric field of SSDT (the electric field is more negative in the core). The fourth result is in the simulations, the parametric independence of radial electric field and its shear ω_s [9] defined by Equation, $\omega_s = \left| d\, V_{E\times B} / dy \right| = (RB_x / B) \left| d\, (E_y / RB_x) / h_y\, dy \right|$, on plasma parameters has been studied. The independence of shear of the electric field on plasma parameters was obtained, Figures (6–8).

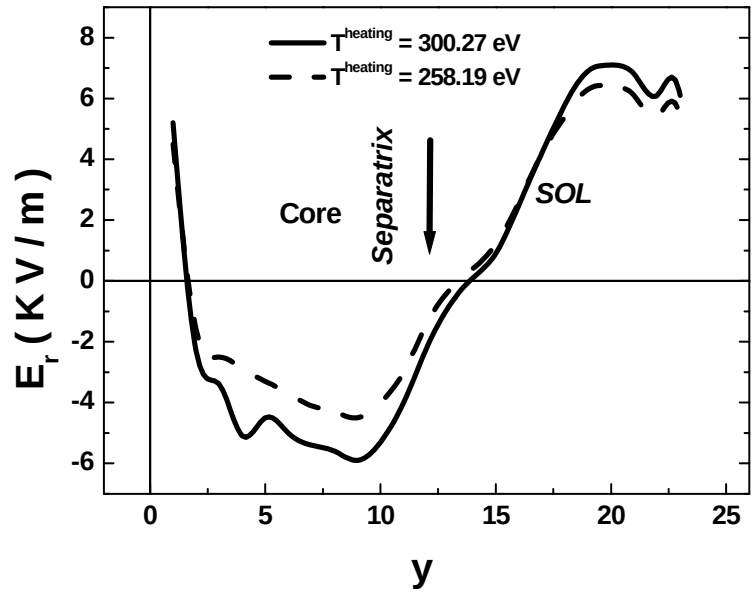

Figure 5. The radial electric field at different temperatures heating of plasma for SSDT

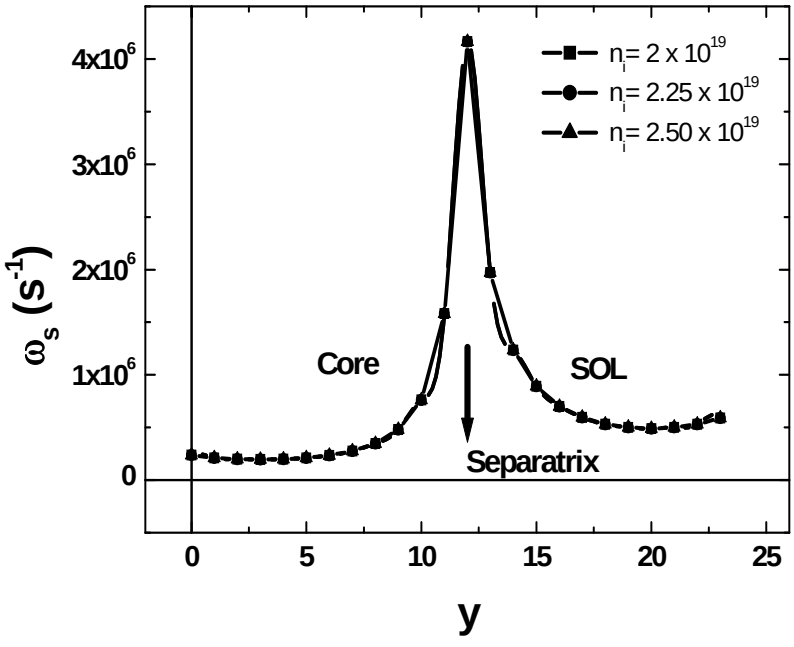

Figure 6. *E* × *B* shear at different plasma density

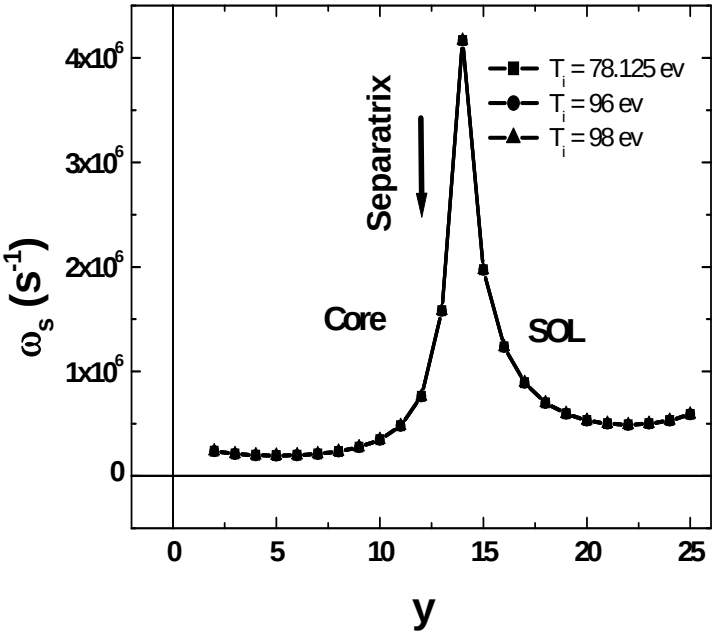

Figure 7. *E* × *B* shear at different ion temperature

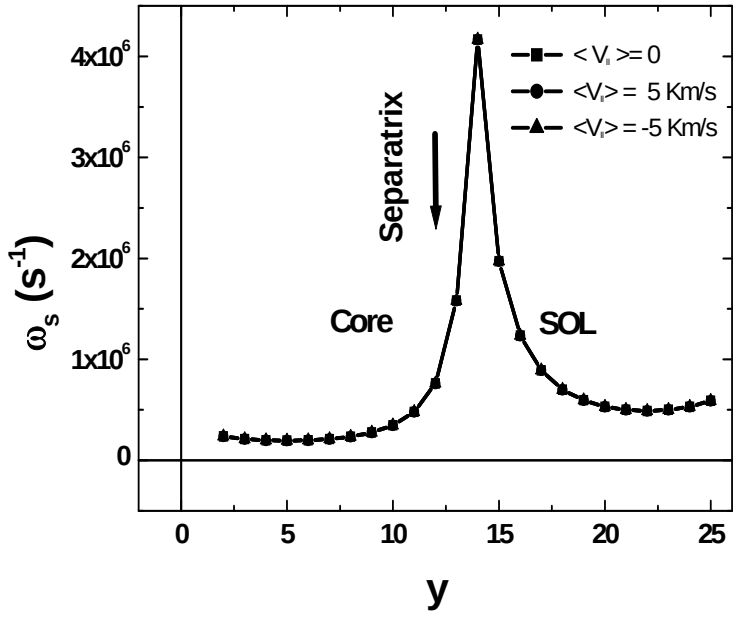

Figure 8. *E* × *B* shear at different average parallel velocity

To obtain a scaling for the L-H transition threshold it is necessary to specify the critical shear when the transition starts. For the critical shear we chose the value of ω_s independently of the regime due to limited knowledge of the turbulent processes. This value must be gives best fitting to the experiment. To reach the chosen critical shear it is necessary to increase the heating power proportionally to the local density and the toroidal magnetic field. This result is explained by the neoclassical nature of the simulated radial electric field. Indeed, the linear dependence of the threshold heating power on the local density corresponds to the constant critical value of the ion temperature, which determines the critical shear. In the vicinity of separatrix the radial electric field of SSDT, is not of order of neoclassical field. Therefore, for SSDT it's can't reach to critical shear to start L-H transition. The deviation of the electric field from the neoclassical value is relatively pronounced

near the separatrix in the outer midplane, as shown in Figure 2. The reason for this difference is connected with the contribution of anomalous radial transport of the toroidal (parallel) momentum to the parallel momentum balance equation [8]. As result, for normal direction of toroidal magnetic field, the parallel fluxes inside and outside the separatrix are coupled Figure (9). The fifth result of simulation is studding the influence of drifts ($E \times B$ and diamagnetic drifts) on the fluxes in SOL. This could be understood from the analysis of parallel and poloidal fluxes in SOL. The structure of the parallel fluxes in the SOL is governed by the combination of three factors. The first is the Pfirch – Schlueter (PS) parallel fluxes close the vertical ion ∇ B drift, and their direction depends on the toroidal magnetic field. The second is the contribution from the radial electric field to the PS fluxes has the same sign as the contribution from ∇ B drift in the SOL since the radial electric

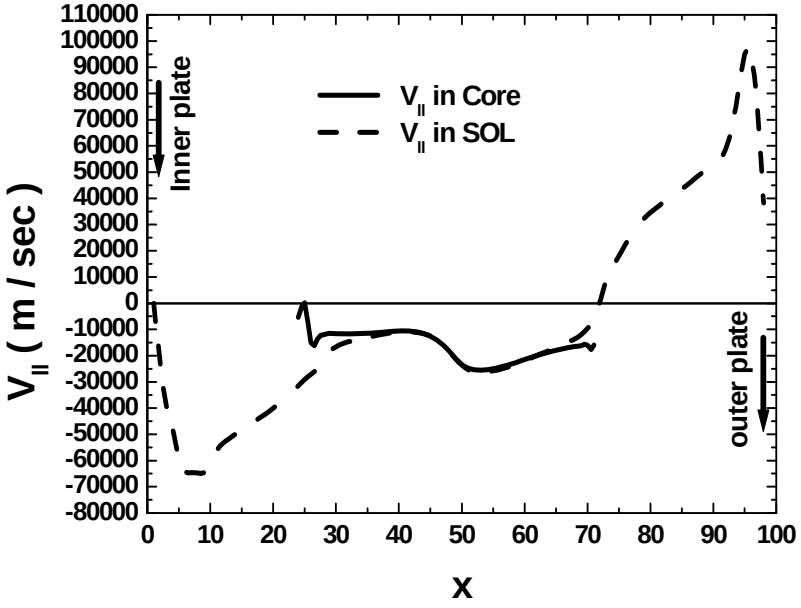

Figure 9. Parallel velocity inside and outside the separatrix

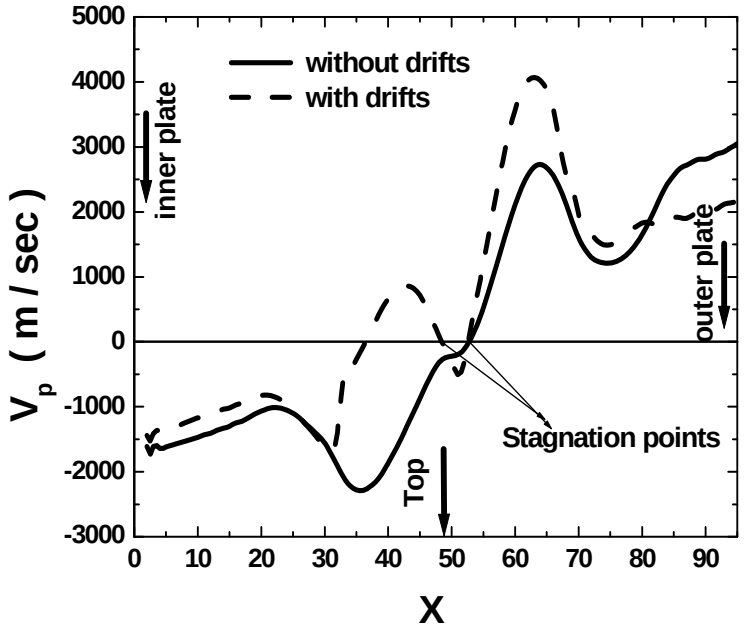

Figure 10. Poloidal velocity in SOL with and without drifts

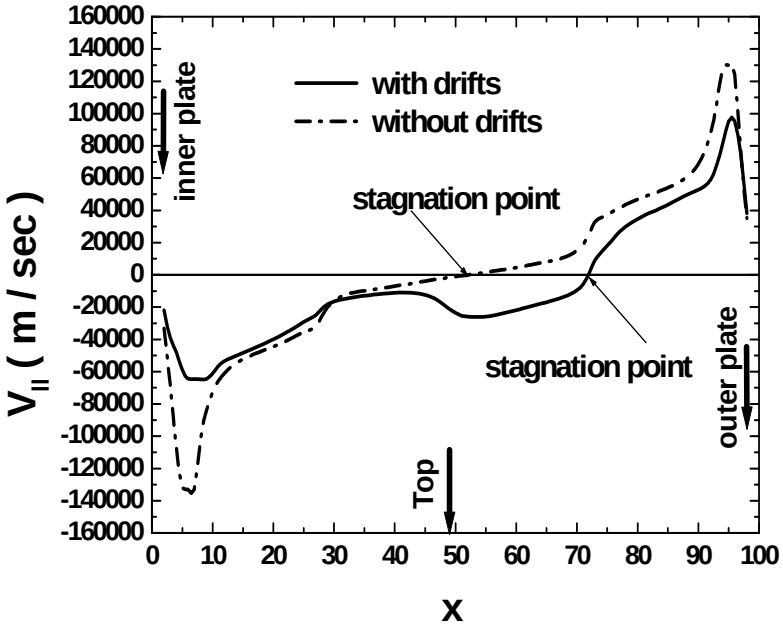

Figure 11. Parallel velocity with and without drifts

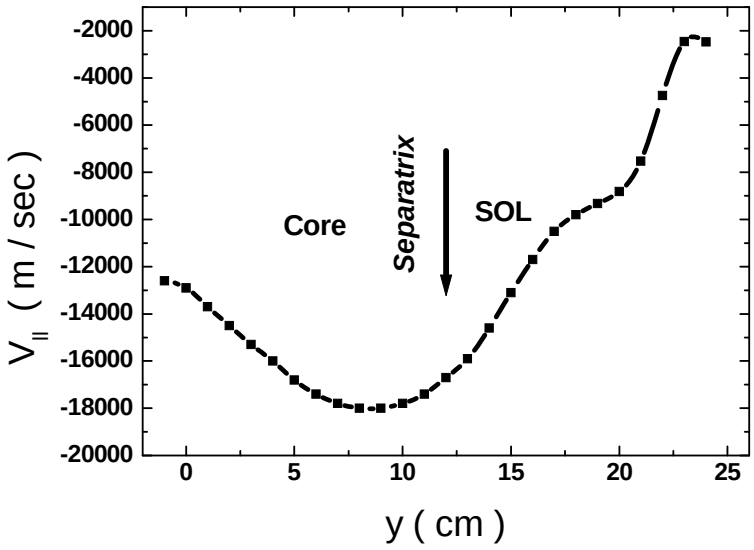

Figure 12. Parallel flux in the edge of SSDT

field is positive in the SOL as shown in Figure 2 (inside separatrix, where the radial electric field is negative, the contribution to PS fluxes ∇ B drifts and E×B drift compensate each other in accordance with neoclassical theory). The third contribution arises from the poloidal fluxes that are responsible for the particle transport to the plates. Those poloidal fluxes are closed the radial diffusive particle fluxes. In the absence of the poloidal E×B and ∇ B drifts these fluxes coincide with the projection of the parallel fluxes. On the one hand, the outer plate is larger than the inner plate and the integral poloidal flux to this plate should be larger. On the other hand, since the plasma in the vicinity of the inner plate is colder and denser, the particle flux per square meter to this plate that is proportional to $n\,(T/m_i)^{1/2}$ is larger than particle flux to outer plate (the pressure is almost the same at the plates).

Switching on E×*B* drift leads to asymmetric in parallel and poloidal fluxes from outer to inner plates and upper part of SOL as shown as in Figures (10,11). Also switching on the poloidal drifts leads to decrease of the parallel velocity, because the poloidal projection of the parallel velocity not compensates poloidal E×B drifts, so that the poloidal rotation changes. Moreover, the position stagnation point for the poloidal did not change much which is

located somewhere near the upper part of the SOL, as shown in Figure 11. In contrast, the position of the stagnation point for parallel flux may be significantly different Figure 11. For normal B the stagnation point is strongly shifted towards the outer plate. This fact is consistent with the observations with simulations [10]. Finally the parallel flow pattern is the result of all three factors. For normal B parallel flux in SOL is negative as shown in Figure 12. Therefore, for normal B parallel flux is directed from outer to inner plate.

3. Conclusions

In conclusion, the performed simulations for SSDT demonstrate the following results: (First) In the vicinity of separatrix the radial electric field was not close to the neoclassical electric field. (Second) the independence of the shear of radial electric field on plasma parameters. (Third) For normal direction of torodial magnetic field, the radial electric field of SSDT was affected by the variation in temperature heating of plasma. (Fourth) Switching on poloidal drifts leads to asymmetric parallel and poloidal fluxes from outer to inner plates and upper part of SOL for normal direction of toroidal magnetic field. Also switching on the poloidal drifts leads to decrease of the parallel velocity, because the poloidal projection of the parallel velocity not compensates poloidal E×B drifts, so that the poloidal rotation changes. (Fifth) The parallel flux is directed from outer to inner plate. (Sixth) The $E \times B$ drift are directed from outer plate to inner plate in SOL, and from inner plate to outer plate in the private region.

REFERENCES

[1] R. Schneider, V. Rozhansky, and P. Xantopoulos, Contribution Plasma Physics, No. 40, pp. 4213, 2004.

[2] F. Wagner, Physical Review Letters, No. 49, pp. 1408, 1982.

[3] H. Biglari, P. H. Diamond, and P. W. Terry, Physics of Fluids, No. B21, pp. 1, 1990.

[4] K. H. Burrell, Physics of Plasma, No. 4, pp. 1499, 1997.

[5] G. J. Radford, Contribution Plasma Physics, No. 36, pp. 187, 1996.

[6] T. D. Rognlien, D. D. Ryutov, N. Mattor, and G. D. Porter, Physics of Plasmas, No. 6, pp. 1851, 1999.

[7] S. P. Hirshman and D. J. Sigmar, Nuclear Fusion, No. 21, pp. 1079, 1981.

[8] A. H. Bekheit, Egyptian Journal of Fusion energy, Vol. 28, No. 4, pp. 338–345, 2008.

[9] T. S. Hahm and K. H. Burrell, Phyics of Plasma, No. 2, pp. 1648, 1994.

[10] S. K. Erents, G. Corrigan, and J. Spence, Journal of Nuclear Materials, No. 290–293, pp. 518, 2001.

Energy and Power Engineering, **2010, 46-52**
doi:10.4236/epe.2010.21008 Published Online February 2010 (http://www.scirp.org/journal/epe)

Valuing Health Effects of Natural Radionuclides Releases from Yatağan Power Plant

Tayfun BÜKE[1], Aylin Çiğdem KÖNE[2]
[1]*Department of Physics, Muğla University, Muğla, Turkey*
[2]*Department of Economics, Muğla University, Muğla, Turkey*
Email: *tbuke@mu.edu.tr*

Abstract: The objective of this paper is the valuation of radiological health effects of Yatağan Power Plant. To this aim the radiation dose calculations are carried out for the population living within 80 km radius of the plant. The average of the maximum measured specific isotopes ^{238}U, ^{232}Th and ^{226}Ra in the flying ash samples are considered as radioactive sources. Based on the dose calculations, first the stochastic health effects and then monetary health effects are estimated. The estimated total collective dose and economic value of the predicted health effects are 0.3098 man Sv/y and 14791 US$/y respectively. The results obtained from the dose calculations are lower than the limits of International Commission of Radiation Protection (ICRP) and it does not pose any risk for public health. Monetary value of health risks is also negligible in comparison to the average yearly sales revenue of the plant which is 250 million US$.

Keywords: coal-fired power plants, collective dose, atmospheric dispersion, valuing health effects

1. Introduction

Yatağan Power Plant (YPP) is one of the largest lignite-fired power plants in Turkey with a total capacity of 630 MW. It has been operated in Muğla province at the western Anatolia since 1982 [1]. Lignite in Muğla province contains some uranium as all lignite does. That uranium passes to ash with a higher concentration during the firing process in furnace chamber at 1000 ^{o}C. While well-urned ash goes to the plant chimney, the others are not burned perfectly, which are called slag ashen drops the furnace chamber floor [2,3]. The radioactive flying ash is released to the atmosphere, depending on the efficiency of the plant's chimney emission control equipment. The major potential pathway, which might result in increased radiation doses to people are inhalation of flying ash, ingestion of food grown in contaminated soil or direct radiation exposure from the increased deposited radioactivity when flying ash are released from the plant chimney [4,5].

In this study, the radiation dose calculations have been carried out using the code CAP88-PC which stands for Clean Air Act Assessment Package [6] for the population living within 80 km radius of the YPP by using the average of the maximum measured specific isotopes ^{238}U, ^{232}Th and ^{226}Ra in the flying ash samples as radioactive sources. Based on the dose calculations, the stochastic health effects have been estimated by using the risk factors, as recommended by the International Commission of Radiation Protection (ICRP) [7]. Then the predicted health effects have been monetized by using the methodology given in NucPacts model [8].

In order to estimate the average dispersion of radionuclides released from a point source, a modified plume dispersion model has been used in the calculations. Pasquill categories A-F with site-specific averaged meteorological conditions are used in the modified dispersion model. The meteorological data on atmospheric stability conditions like mean wind speed and the frequency distribution of wind direction are obtained from Turkish State Meteorological Service [9]. The population distribution around the YPP is taken from Turkish State Institute of Statistics [10].

Annual radioactivity release rate for three different radionuclides in the dose calculations is calculated by using the ash emission rate from the plant chimney, the measured activity in flying ash and the plant loading factor [11,12].

The rest of the study is organized as follows. Section 2 introduces the source terms for ^{238}U, ^{232}Th and ^{226}Ra. Section 3 deals with the assessment of radiation hazard. In Section 4 risk calculations are given in detail. Section 5 presents a monetary valuation of health effects. Finally, Section 6 gathers the main conclusions derived from this paper.

2. Source Terms

In this study, the literature related to the maximum measured specific isotopes ^{238}U, ^{232}Th and ^{226}Ra in the flying ashes of the YPP are reviewed. In those studies, the concentrations of ^{238}U, ^{232}Th and ^{226}Ra have been

measured with high-resolution gamma spectroscopy. The maximum radionuclides concentrations in flying ashes of the YPP are presented in Table 1 [13–15]. As seen from Table 1 the measured concentrations are different from each other and the average of the maximum measured concentrations of different studies for ^{238}U, ^{232}Th and ^{226}Ra are 854, 191, 286 Bq/kg respectively. This is an expected result since the natural radionuclides content in the flying ashes of a coal fired power plant depend on the quality of the coals burned in the power plant. The radionuclides concentrations can be changed up to 1 and 2 orders in magnitude according to the coal types used in the power plant [2].

In this study, the average of the maximum measured specific isotopes ^{238}U, ^{232}Th and ^{226}Ra in the flying ash samples are used as radioactive sources for the potential worst-case scenario.

3. Assessment of Radiation Hazard

The radiation dose calculations have been carried out by the code CAP88-PC for the population living within 80 km radius of the YPP by using the average of the maximum measured specific isotopes ^{238}U, ^{232}Th and ^{226}Ra in the flying ash samples as radioactive sources.

The CAP88-PC (which stands for Clean Air Act Assessment Package) computer code is a set of computer programs, databases and associated utility programs for estimation of dose and risk from radionuclide emissions to air on a personal computer. It uses a modified Gaussian plume equation to estimate the average dispersion of radionuclides released from up to six emitting sources for a circular grid of distances and directions for a radius of up to 80 km around the facility. The sources may be either elevated stacks, such as a smokestack, or uniform area sources, such as a pile of uranium mill tailings. Plume rise can be calculated assuming either a momentum or buoyant-driven plume. The plume centerline remains at effective stack height unless gravitational settling of particulates produces a downward tilt, or until meteorological conditions change. Radionuclides are depleted from the plume by precipitation scavenging, dry deposition and radioactive decay. The stored depletion fractions were calculated numerically with a Simpson's rule. Ground surface and soil concentrations are calculated for those nuclides subject to deposition due to dry deposition and precipitation scavenging. Agricultural arrays of milk cattle, beef cattle and agricultural crop area are generated automatically, requiring the user to supply only the agricultural productivity values. Only 7 organs are valid for the effective dose equivalent. They are Gonads 25 %, Breast 15%, Red marrow 12%, Lungs 12%, Thyroid 3%, Endost 3% and Remainder 30 %. Doses are provided for the pathways of ingestion and inhalation intake, ground level air immersion and ground surface irradiation. Particle size, clearance class and gut-to-blood transfer factors of the released nuclide type are further break down factors. These factors are stored in a database for use by the program.

Table 1. Concentrations of natural radionuclides in flying ashes of the YPP (Bq/kg)

Reference number	^{238}U	^{232}Th	^{226}Ra
[13]	375	253	63
[14]	1704	178	122
[15]	484	141	672
Average	**854**	**191**	**286**

3.1 Input Data

The estimate of radioactivity released annually in the environment by the YPP has been carried out for ^{238}U, ^{232}Th and ^{226}Ra that, according to average of the maximum measured concentrations given in the literature, have resulted to be the most significant. Annual nuclide release rate for the radionuclide type i [Q_i : Bq/y] is calculated from the relation given by:

$$Q_i = \dot{m} A_i L \tag{1}$$

where $\dot{m}$ is the ash emission rate from the plant chimney (kg/y), A_i is the average of the maximum measured radionuclide type i in flying ash (Bq/kg) and L is the plant loading factor.

Plume rise is calculated by using the momentum plume model since ash emission velocity at the chimney exit is known. An average lid for the assessment area is provided as part of the input data. The agricultural data like beef cattle density, milk cattle density and land fraction cultivated for vegetable crop and others for the region are inputted to the code in order to estimate of emitted radionuclides into the food chain.

The meteorological data which obtained from Turkish State Meteorological Service [9] are processed to find out the stability array file for 16 directions. The atmospheric dispersion of the radionuclides from the stack of a power plant are strongly depends on the meteorological conditions where the power plant is located. Therefore the meteorological data are annually averaged within hourly time step for the each year of the period 1975–2006. The better estimation has been made in dose calculations by this way.

The stability array file consists of 4 different wind frequencies, one for each of the 16 wind directions and 6 Pasquill stability category (A-F). 16 records are entered for each Pasquill stability category and wind frequencies. Pasquill stability classes used in the code are A) extremely unstable, B) unstable, C) slightly unstable, D) neutral, E) slightly stable, and F) stable. Once a stability array file has been prepared, and it is converted to wind file for input to the CAP88-PC code which is namely

MUGLA. WND.

Population distribution in the 80-km radius of the plant is presented Table 2 [10] and the dose calculations are made for those population. The program uses a population file for dose calculations. The population file contains the location description, latitude, and longitude of the facility, the number of distances and population for each distance according to 16 wind directions in counter-clockwise order starting with North. The distances are edge points of each sector and are entered in the population file in km. The population distribution file which is namely MUGLA.POP is prepared for 20 distances of each wind direction. Those 20 distances are chosen closest values to the distances presented in Table 2, which are the exact values around the plant to get the sensible results for dose calculations.

Input parameters used in the calculations are given in Table 3 [1,16–18]. Calculated collective effective dose equivalent rate values including all radionuclides and pathways effect around the plant by CAP88-PC code are presented Table 4.

4. Risk Calculation

The occurrence of each of the main stochastic health effects (i.e. fatal and non-fatal cancers and severe hereditary effects) arising as a result of routine atmospheric emission from a power plant is calculated as [8],

$$N_h = HR_h \tag{2}$$

where N_h is the total occurrence of health effect, h (cases/y), H is the total collective dose occurring via all pathways (man Sv/y), R_h is the risk factor for health effect h (cases man/Sv).

The calculated health effects by the risk factors in CAP88-PC computer code are lower than the calculated health effects by the risk factors which are recommended by the ICRP [7]. Therefore in this study, the ICRP's risk factors have been used in calculations for the potential worst-case scenario. Those values are given in Table 5. The total stochastic health effects around the YPP which are calculated from Equation (2) are given in Table 6.

Table 2. Population distribution in the 80-km radius of the YPP

Location name	Population	Distance to plant (km)	Direction
Yatağan	46252	3	N
Çine	53770	32	N
Köşk	25321	65	N
Sultanhisar	22795	66	N
Aydın, Merkez	208341	46	NNW
Koçarlı	37167	53	NNW
İncirliova	40733	70	NNW
Germencik	45821	75	NNW
Karpuzlu	13207	37	NW
Söke	137739	70	NW
Milas	112808	28	W
Didim	37395	71	W
Bodrum	97826	68	WSW
Datça	13914	77	WSW
Marmaris	79302	55	S
Muğla, (center)	83511	26	SE
Ula	21944	44	SE
Köyceğiz	29196	66	SE
Ortaca	35670	77	SE
Beyağaç	7332	72	ESE
Kale	21390	61	E
Tavas	60669	80	E
Kavaklıdere	12548	25	ENE
Babadağ	8212	80	ENE
Karacasu	21980	65	NE
Bozdoğan	35190	44	NNE
Yenipazar	15492	51	NNE
Nazilli	145963	67	NNE
Kuyucak	31094	81	NNE
Total	**1502582**		

Table 3. Input parameters used in the calculation

Explanation	Values
Grid distances, (m)	3000, 14500, 26500, 35000, 45000, 54000, 61000, 67000, 73000, 78000
Annual precipitation in Yatağan, (cm/y)	64.96
Annual ambient temperature in Yatağan, (°C)	16.20
Annual average wind speed in Yatağan, (m/s)	2
Height of lid, (m)	642
Chimney height, (m)	120
Chimney inner diameter at the exit, (m)	6.4
Ash emission velocity at the chimney exit, (m/s)	4.1
Ash emission rate from the chimney, (kg/y)	7.55×10^6
Plant loading factor (%)	75
Average of the maximum measured activity in flying ash (^{238}U, ^{232}Th, ^{226}Ra) (Bq/kg)	854, 191, 286
Annual nuclide release rate, (Bq/y)	4.84×10^9, 1.08×10^9, 1.62×10^9
Human inhalation rate, (cm^3/hr)	9.17×10^5
Land fraction cultivated for vegetable crops	5.50×10^{-2}
Beef cattle density, (number/km^2)	3.89
Milk cattle density, (number/km^2)	1.13
Meat ingestion per person, (kg/y)	15
Leafy vegetable ingestion per person, (kg/y)	140
Cereals ingestion per person, (kg/y)	228
Milk ingestion per person, (L/y)	33

Table 4. Collective effective dose equivalent (man Sv/y)

Distance, km	N	NNW	NW	WNW
3.00	0.0480	0.0000	0.0000	0.0000
14.50	0.0000	0.0000	0.0000	0.0000
26.50	0.0000	0.0000	0.0000	0.0000
35.00	0.0081	0.0000	0.0040	0.0000
45.00	0.0000	0.0390	0.0000	0.0000
54.00	0.0000	0.0060	0.0000	0.0000
61.00	0.0000	0.0000	0.0000	0.0000
67.00	0.0050	0.0000	0.0000	0.0000
73.00	0.0000	0.0110	0.0230	0.0000
78.00	0.0000	0.0000	0.0000	0.0000
Distance, km	W	WSW	SW	SSW
3.00	0.0000	0.0000	0.0000	0.0000
14.50	0.0000	0.0000	0.0000	0.0000
26.50	0.0510	0.0000	0.0000	0.0000
35.00	0.0000	0.0000	0.0000	0.0000
45.00	0.0000	0.0000	0.0000	0.0000
54.00	0.0000	0.0000	0.0000	0.0000
61.00	0.0000	0.0000	0.0000	0.0000
67.00	0.0000	0.0120	0.0000	0.0000
73.00	0.0055	0.0000	0.0000	0.0000
78.00	0.0000	0.0015	0.0000	0.0000
Distance, km	S	SSE	SE	ESE
3.00	0.0000	0.0000	0.0000	0.0000
14.50	0.0000	0.0000	0.0000	0.0000
26.50	0.0000	0.0000	0.0260	0.0000
35.00	0.0000	0.0000	0.0000	0.0000
45.00	0.0000	0.0000	0.0048	0.0000
54.00	0.0150	0.0000	0.0000	0.0000

Distance, km	N	NNW	NW	WNW
61.00	0.0000	0.0000	0.0000	0.0000
67.00	0.0000	0.0000	0.0045	0.0000
73.00	0.0000	0.0000	0.0000	0.0012
78.00	0.0000	0.0000	0.0050	0.0000
Distance, km	E	ENE	NE	NNE
3.00	0.0000	0.0000	0.0000	0.0000
14.50	0.0000	0.0000	0.0000	0.0000
26.50	0.0000	0.0027	0.0000	0.0000
35.00	0.0000	0.0000	0.0000	0.0000
45.00	0.0000	0.0000	0.0000	0.0039
54.00	0.0000	0.0000	0.0000	0.0016
61.00	0.0034	0.0000	0.0000	0.0000
67.00	0.0000	0.0000	0.0023	0.0140
73.00	0.0000	0.0000	0.0000	0.0000
78.00	0.0077	0.0009	0.0000	0.0027

Table 5. Risk factors for main stochastic health effects for whole population (case/man Sv)

Health Effect	Risk factor
Fatal cancer	$5.0\text{x}10^{-2}$
Non fatal cancer	$1.0\text{x}10^{-2}$
Severe hereditary effects	$1.3\text{x}10^{-2}$

Table 6. The total stochastic health effects (cases/y)

Health effect type	Number of cases
Fatal cancer	$1.549\text{x}10^{-2}$
Non fatal cancer	$3.098\text{x}10^{-3}$
Severe hereditary effects	$4.027\text{x}10^{-3}$

5. Monetary Unit Costs for Health Impact Assessments

The final stage of the impact pathway analysis is to value the health endpoints in money terms. In literature there are two approaches that may be used in health risk assessments; the first is based on the Value of a Statistical Life (VOSL) and the second is based on the Value of a Life Year Lost (VLYL) [19]. The latter differs from the former in that it takes into account the latency period of different types of cancers. A component related to the cost of illness has also been included in VLYL. Estimates for the economic unit value of radiological health effects have been made for several countries. Ideally, economic unit values should be based on local economic valuation of a country. However, in the absence of such information economic unit values for specific to a country may be transferred to another country after making some adjustments on the basis of real per capita income. This adjustment is required to reflect differences in income and hence, willingness-to-pay regarding the valuation of the health damages of two countries. The following formula can be used to arrive at economic unit values of radiological health effects for countries where there are no studies [19]:

$$D_Y = D_X \left(\frac{PPPGNP_Y}{PPPGNP_X} \right)^E \quad (3)$$

where D_Y economic unit values of radiological health damages for country Y, D_X economic unit values of radiological health damages for country X, $PPPGNP_Y$ and $PPPGNP_X$ is real Gross National Product per capita in purchasing power parity terms for country Y and X respectively, E is the elasticity of income.

Once the total occurrence of health effect and economic unit values are calculated from Equation (2) and Equation (3) respectively; the total damage in terms of health effect h is valued using $VOSL$ or $VLYL$ approach. $V_h(VOSL, VLYL)$ can be calculated from the following formula [19]:

$$V_h(VOSL, VLYL) = N_h \, D_h(VOSL, VLYL) \quad (4)$$

In this study, the economic unit values for Turkey are estimated by using Canadian economic unit values of radiological health impacts since the Canada is the country that the recent economic unit values of radiological health impacts are available [8]. $PPPGNP_{Turkey}$ and $PPPGNP_{Canada}$ 8600 US$ and 27630 US$ respectively, in 2000 [20]. The elasticity (E) of income is assumed to be

Table 7. Economic unit values of radiological health impacts (US$/case)

	Canada	Turkey
Fatal cancer VOSL	$1.73\text{x}10^6$	$5.38\text{x}10^5$
Fatal cancer VLYL	$7.73\text{x}10^5$	$2.41\text{x}10^5$
Non-fatal cancer	$5.77\text{x}10^5$	$1.80\text{x}10^5$
Severe hereditary effect	$1.73\text{x}10^6$	$5.38\text{x}10^5$

Table 8. The monetary value of the predicted health effects (US$/y)

Health effect type	Damage cost
Fatal cancer VOSL	8334
Fatal cancer VLYL	3733
Non fatal cancer	558
Severe hereditary effects	2167
Total	**14791**

equal to 1 [8,21]. Economic unit values of radiological health impacts for Canada and estimated values for Turkey are given in Table 7.

Based on the economic unit values of radiological health impacts (see Table 7), the valuation of the predicted health effects are calculated from Equation (4). The calculated damage costs of the radiological health effects are given in Table 8.

6. Conclusions

In this study, the radiation dose calculations have been carried out by the code CAP88-PC for the population living within 80 km radius of the Yatağan coal-fired power plant (YPP). The average of the maximum measured specific isotopes ^{238}U, ^{232}Th and ^{226}Ra in the flying ash samples are considered as radioactive sources. Based on the dose calculations, the stochastic health effects and predicted health effects have been estimated. It is seen that the total and the maximum collective effective dose equivalent rate is 0.3098 man Sv/y and 0.0510 man Sv/y respectively. Those values are lower than recommended by the ICRP and it does not pose any risk for public health.

The total monetary value of health risk is 14791 US$/y. The yearly total revenue of the YPP from the sales of electricity is approximately 250 million US$ [1,22]. The results indicate that the predicted health effects are negligible in comparison to the economic value of the YPP.

YPP was stopped between 20 February and 20 March 1993 because of the speculations on radionuclide emissions from the plant. It was a big occasion for news media [23]. The speculations on the radionuclide emissions from the YPP and their health effects have continued since 1993. Against the speculations, there is no significant literature on the stochastic health effects and the cost of the predicted health effects from the YPP [24]. Therefore, the results of this study are very useful for ending up the speculations on the health effects and the costs of those effects.

REFERENCES

[1] General Description of Yatağan Coal Fired Power Plant, Electricity Generation Cooperation, Muğla, 2006.

[2] T. Zeevaert, L. Sweeck, and H. Vanmarcke, "The radiological impact from airborne routine discharges of a modern coal fired power plant," Journal of Environmental Radioactivity, Vol. 85, No. 3, pp. 1–22, 2006.

[3] C. Papastefanou and S. Charalambous, "On the escaping radioactivity from coal power plants (CPP)," Health Physics, Vol. 64, pp. 293–302, 1984.

[4] Radiological Impact on the UK Population of Industries Which Use or Produce Materials Containing Enhanced Levels of Naturally Occurring Radionuclides: Part I: Coal-Fired Electricity Generation, Report No: NRPB-R327, National Radiological Protection Board, Chilton, 2001.

[5] A. Nakaoka, M. Fukushima, and S. Takagi, "Environmental effects of natural radionuclides from coal-fired power plants," Health Physics, Vol. 47, No. 3, pp. 407–416, 1984.

[6] B. Parks and S. P. E. Chaki, CAP88-PC Version 2.0 Updated User's Guide, Report No: EPA 402-R-00-004, Las Vegas, 2000.

[7] 1990 Recommendations of the International Commission on Radiological Protection, Report No. 60, International Commission on Radiological Protection, Pergamon Press, Oxford, 1991.

[8] Review of NucPacts: An Environmental Assessment Package, International Atomic Energy Agency, Vienna, 2003.

[9] Annual Meteorological Conditions in Yatağan 1975–2006 Periods, Turkish State Meteorological Service, Ankara, 2007.

[10] City and Village Population, Annual Growth Rate of Popupation, Surface Area and Density by Districts in Turkey, Turkish Statistical Institute, Ankara, http://www.tuik.gov.tr/PreIstatistikTablo.do?istab_id=220

[11] T. Buke, "Dose assessment around the Yatağan coal-fired power plant due to measured gross alpha radioactivity levels in flying ash," Journal of Radioanalytical and Nuclear Chemistry, Vol. 256, No. 2, pp. 323–328, 2003.

[12] S. Righi, P. Lucialli, and L. Bruzzi, "Health and environmental impacts of a fertilizer plant Part I: Assessment of radioactive pollution," Journal of Environmental Radioactivity, Vol. 82, pp. 167–182, 2005.

[13] Natural radioactivity measurements in ash-samples of the Yatağan Power Plant, Turkish Atomic Energy Authority, Ankara, 1994.

[14] T. Akyüz, S. Akyüz, A. Varinlioğlu, A. Köse, J. Eric, and D. Davies, "FT-IR, EDXRF and gamma-isotopic analyses of ashes from coal fired power plants of Turkey," Spectroscopy Letters, Vol. 29, pp. 1131–1139, 1996.

[15] G. A. Ayçık and A. Ercan, "Off-line determination of ash content directly in coal samples via-spectrometry," Applied Spectroscopy Reviews, Vol.33, pp. 237–251, 1998.

[16] Economic and Commercial Conditions of Aydın. Industry and Trade Center of Muğla, Muğla, 2007.

[17] Economic and Commercial Conditions of Muğla, Industry and Trade Center of Muğla, Muğla, 2007.

[18] N Selçuk, A. Atımtay, O. Uslu, Ş. Cirik, H. Vurdu, G. Tuncel, Z. Kaya, M. Evirgen, and C. Yurteri, Scientific Committee Report for Kemerkoy Thermal Power Plant, Ankara, 1995.

[19] A. Markandya and R. Boyd, "Valuing the human health effects of routine atmospheric releases from nuclear facilities," International Atomic Energy Agency, Vienna, 1999.

[20] World Development Indicators (WDI), http://ddp-xt.worldbank.org.

[21] E. Liun, A. H. Kuncoro, and E. Sartono, "Environmental impacts assessment of Java's electricity generation using SimPacts model," International Conference on Advances in Nuclear Science and Engineering in Conjunction with LKSTN, pp. 379–384, 2007.

[22] Electricity selling prices of Turkey for the year 2000, Directorate General of Turkish Electricity Distribution, 2000.

[23] M. Aslan, "A typical example of the discussion about the environmental impacts of coal fired thermal power plants in Turkey: Yatağan thermal power plant experience," Symposium on Environmental effects of Electricity Production from Coal, Ankara, 1995.

[24] T. Oğuz "Personal communications," Associate Mayor of Yatağan, 2008.

Energy and Power Engineering, **2010, 53-64**
doi:10.4236/epe.2010.21009 Published Online February 2010 (http://www.scirp.org/journal/epe)

The Implications of Fluorescent Lamp Electronic Ballast Dimming
—An Experimental Study

Sheryl G. Colaco[1], Ciji P. Kurian[2], V. I. George[1], Anitha M. Colaco[3]
[1]*Department of Instrumentation & Control Engineering, Manipal Institute of Technology, Manipal, India*
[2]*Electrical & Electronics Engineering, Manipal Institute of Technology, Manipal, India*
[3]*Electrical & Electronics Engineering, NMAMIT, Nitte, India*
Email: *sheryl_grace*2001@*yahoo.co.in*

Abstract: In recent years, fluorescent lamp dimming controls are an integral part of daylight artificial light integrated schemes intended for realization of energy savings. However, dimming, like any lighting option, presents its own particular challenges and potential tradeoffs. In view of this, the present manuscript depicts the preliminary work progress carried out to arrive at a comprehensive idea on dimming implications on key factors: electrical characteristics, photometric distributions of lighting systems and influence on quality as well as quantity of visual environment. The objective is to experimentally establish the acceptable range of dimming control voltage that would satisfy both electrical and photometric performance of luminaire. The vital part of the paper is devoted towards presentation of measurement results. For the experimental analysis, three representative samples of different commercial analog 1-10VDC electronic dimmable ballasts and fluorescent fixtures are compared and evaluated over their control voltage dimming range.

Keywords: dimming, power factor, power quality, chromaticity, light intensity, illuminance

1. Introduction

In the present scenario, electronic dimming ballasts are crucial in automatic control and dimming function for energy-management applications such as daylight harvesting [1]. Over many years, in spite of many reports and case studies cite the advantages of daylight linked automatic light dimming systems; comparatively very less schemes have been implemented [2,3]. Part of the reason could be attributed to the issues associated with lamp dimming that have been debated during the last few years. A number of literatures in print state that at some stage during deep dimming; electronic dimming ballast exhibit poor performance reflected by dramatic deterioration of electric and photometric characteristics [4] Important concerns related to dimming include lamp life, perceived brightness, perception of light level reduction, color shift, power quality and energy efficiency [3]. Many past studies address these issues separately. The effect of dimming on lamp life was investigated by Tetri and Gligor [5]. Their experimental results indicate that mortality was higher in the dimmed test groups than in the undimmed test groups. Further their lamp life test result showed that with electronic ballasts lamps reached their nominal life even if the lamps are dimmed statically or dynamically. A study by Akashi *et al*. [6] on the detection and acceptability of temporarily reduced light levels showed that a reduction of 15% in illuminance levels is the approximate threshold for noticing changes under typical office lighting conditions. Further their study revealed, light level reductions that are deemed acceptable in an office environment ranges from approximately 33% to 50% depending on the office task and whether the occupants were aware of the purpose and benefits of dimming. Literature reports and utilities show an increased concern about the power quality aspects due to dimming of electronic ballasts [7,8]. Experimental tests performed by National Lighting Product Information Program (NLPIP)[9] on electronic dimmable ballasts of T8 and CFL lamps document that progressive decrease in dimming levels are associated with increase in voltage as well as current THD accompanied by corresponding diminishing of power factor at minimum light output. In their separate experimental study conducted by Benoit *et al*. [10] and Doulos *et al*. [11] showed that power factor decreases in function of dimming depth due to subsequent setting up of harmonics while dimming. Further, inorder to quantify energy savings from dimming ballasts Doulos *et al*. [11] performed various sets of electrical and illuminance measurements on eighteen commercial

ballasts at different dimming levels. The authors [11] developed polynomial functions between light output and consumed power to reckon the relative differences in energy savings. The chromaticity of a fluorescent lamp is a supplementary parameter used to gauge light quality. The adverse effect of dimming when it lowers the luminous efficacy of the light source or changes its colour requires careful inspection. The present communication reports the preliminary study of an ongoing research project on promotion of daylighting for energy conservation in a daylight artificial light integrated scheme. This paper is organized as follows. Following a brief discussion on problem statement in Section 2, the main sections of this paper includes experimental methodology in Section 3, presentation of measurement results in Section 4 and finally, brief conclusions are deduced in Section 5. It is envisaged that the information from these studies would be of assistance to architect, the engineer, the lighting designer or a combination of these during the initial stage when different daylighting schemes and concepts are being developed.

2. Problem Statement

The performance characteristic of lamps and ballasts usually vary from one manufacturer to another. Therefore prior to new lighting installations not only choice of the lamp make is important but also there is a need to study electrical and photometric characteristics of luminaire. Obviously this could also serve as an important starting datum for analysis and optimization of installations performances in buildings. Issues related to electronic ballast dimming on fluorescent lamp and visual performance characteristics are the subject considered for discussions in this paper. This paper seeks to put into perspective the subject of fluorescent lamp dimming in a manner that has not been discussed previously. The intention is to ascertain the preferable range of ballast control signal voltage that does not deteriorate electrical characteristics, photometric distributions of lighting systems and visual environment quality as well as quantity. For practical evaluation, three separate analogs dimming ballast each supplied by different manufacturer and most commonly employed for daylight responsive dimming applications in Indian offices are analyzed.

3. Experimental Methodology

The methodology developed in this work combines electrical; and photometric measurements including computer simulations. The customary testing and measurement procedures specified by CIE and IESNA were followed [12–15]. The experimental tests were performed under a standard set of conditions at the Photometry Laboratory of Manipal Institute of Technology, Manipal (India). Three 230V, 2×36W analog electronic dimming ballasts with corresponding pairs of T8 fluorescent lamps supplied by 3 different manufacturers Osram, Wipro & Philips (labeled in this paper as EDB-A, EDB-B, EDB-C respectively) were examined for practical comparison and evaluation. In order to assess the performance characteristic during dimming; twin 36W fluorescent lamps were dimmed by manual adjustment of dimming ballast control signal DC voltage from 1 to 10V (up or down) with a digital 0-30V regulated DC power supply. Prior to taking measurements the tested lamps were pre burned for full light output for 100 hours before dimming with a supply voltage of 230V a.c. 50 Hz and ballast control voltage of 10V. The adjustment from one dimming level to another level was done gradually. The lamps were tested on 10 different ballast control voltages in step difference of 1 volt. To ensure that the temperature of each lamp stabilized during testing, at each control voltage level the lamps were operated for at least 10 min. All the measurements were performed at an ambient temperature of 26℃±2° with a stabilized line voltage of 230V a.c.

To assess the performance characteristics; dimming ballast control voltage (1-10V DC) formed the variable parameter. The dependent variables include electrical parameters (i.e., current, power factor, active power, voltage and current harmonics) and photometric parameters (i.e., luminous intensity, CCT, CU, chromaticity). The following measurements were carried out to provide the technical background for evaluating the electric and photometric characteristics of tubular fluorescent lamp systems all through dimming control signal voltage range of electronic dimming ballast.

The luminous flux of the lamp in each dimming mode was measured in an integrating sphere with an inner diameter of 2.0 m**.** Power line voltage and line current harmonic spectrum together with active power, apparent power and power factor was recorded using FLUKE 43B power quality analyzer. Lamp Chromaticity coordinates were gauged using Konica Minolta CL-200 Chroma meter contained in a Color chromaticity coordinate measuring unit. The estimation of luminaire luminous light intensity in C0-180 and C 90-270 planes involved collection of illuminance data in both the specified planes in a darkroom at a fixed distance of 5m from luminaires mounted on a swing arm Goniophotometer. The luminous intensity was then calculated from preceding illuminance measurement using the inverse square distance law. Lighting calculation software that this authors typically uses are AGI 32 photometric toolbox for computation of CU chart and Relux light simulation software for rendering of results for visualization of the effects of dimming on quality and quantity of illuminance in an interior. Luminaire candela power distribution plots and 3D mesh plots of work plane illuminance distribution were obtained using Matlab; a computational software [16].

4. Presentation of Measurement Results

Analog electronic dimming ballasts permit the light output of the lamp to be continuously controlled over a range of approximately 1% to 100% of full light output.The main method of analog control utilizes a low voltage control signal in the range 1-10V dc. A separate pair of control cables runs from the controller to luminaires in the controlled group. Dimming is accomplished by adjustment of control signal voltage of the ballast. This modifies the amplitude of current flow in the fluorescent lamp to achieve variation in emitted lamp light output. Consistent dimming behaviour varies among different ballasts made by different manufacturers. The ensuing subsections enumerate the impacts of dimming on performance characteristics of fluorescent lamps.

4.1. Effect on Electrical Characteristics

Figures 1(a) and 1(b) illustrate the decrease in current and subsequently reduction in power consumption during dimming down from 10V to 0V. All the reported ballast lighting system has a maximum active power consumption of approximately 72W. During dimming down process the reduction in active power consumption ranges from a maximum of 100% at 10V to a minimum of 16%, 19% and 17% at 0V; for ballasts EDB-A, EDB-B and EDB-C respectively. Figures 1(c) and 1(d) depict the variation of percentage light output as a function of control voltage and percentage input power respectively. It is noted that for all the ballasts neither the light output nor the system power consumption has a linear relationship with control voltage. Studies of Choi *et al*. [17] report that this nonlinear variation in light output with different dimming control voltage is one among many other reasons for unreliability and inaccuracy of daylight dimming systems, seeing that a particular control voltage cannot be predicted when a certain light output is required. In order to achieve performance consistency of electronic dimming ballast especially for PC based light control algorithms, authors [17] suggests the application of best fit functions using regression methods that would satisfy the relationship between control voltage of dimming ballast and its corresponding light output characteristics. As seen form Figure 1(d), at a control voltage of 0V; all the test lamps emit approximately 1% of light output with a minimum power consumption of approximately 20%. It is noticed during the experiment that neither the lamp extinguishes nor flickers at minimum control voltage. Figure 1(e) shows the variation of luminous efficacy as a function of percentage active power consumption. The luminous efficacy drops from a maximum of 43%, 45% and 42% to a minimum of approximately 1% for EDB-A, EDB-B and EDB-C lamps respectively. It is also observed from Figure 1(e) that luminous efficacy of all the tested lamps stays approximately constant with dimming until about 57% of input power; thereafter it decreases drastically.

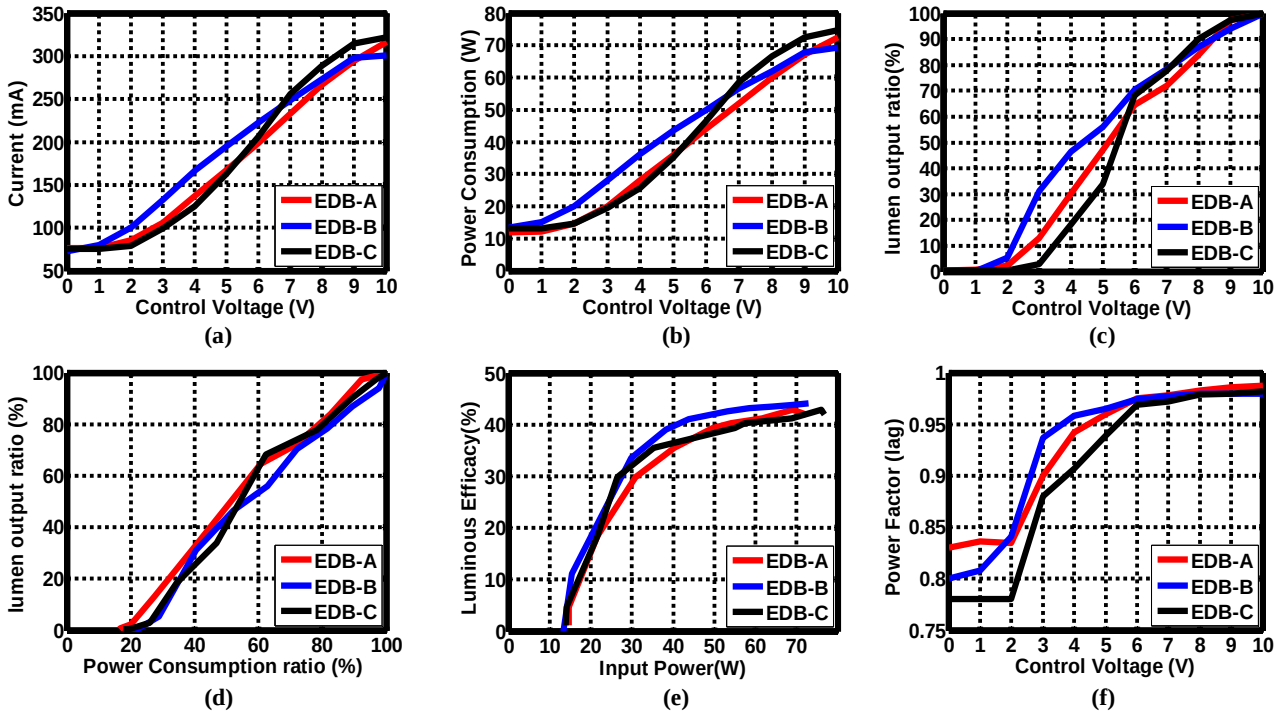

Figure 1. Measured electrical characteristics over the control voltage dimming range

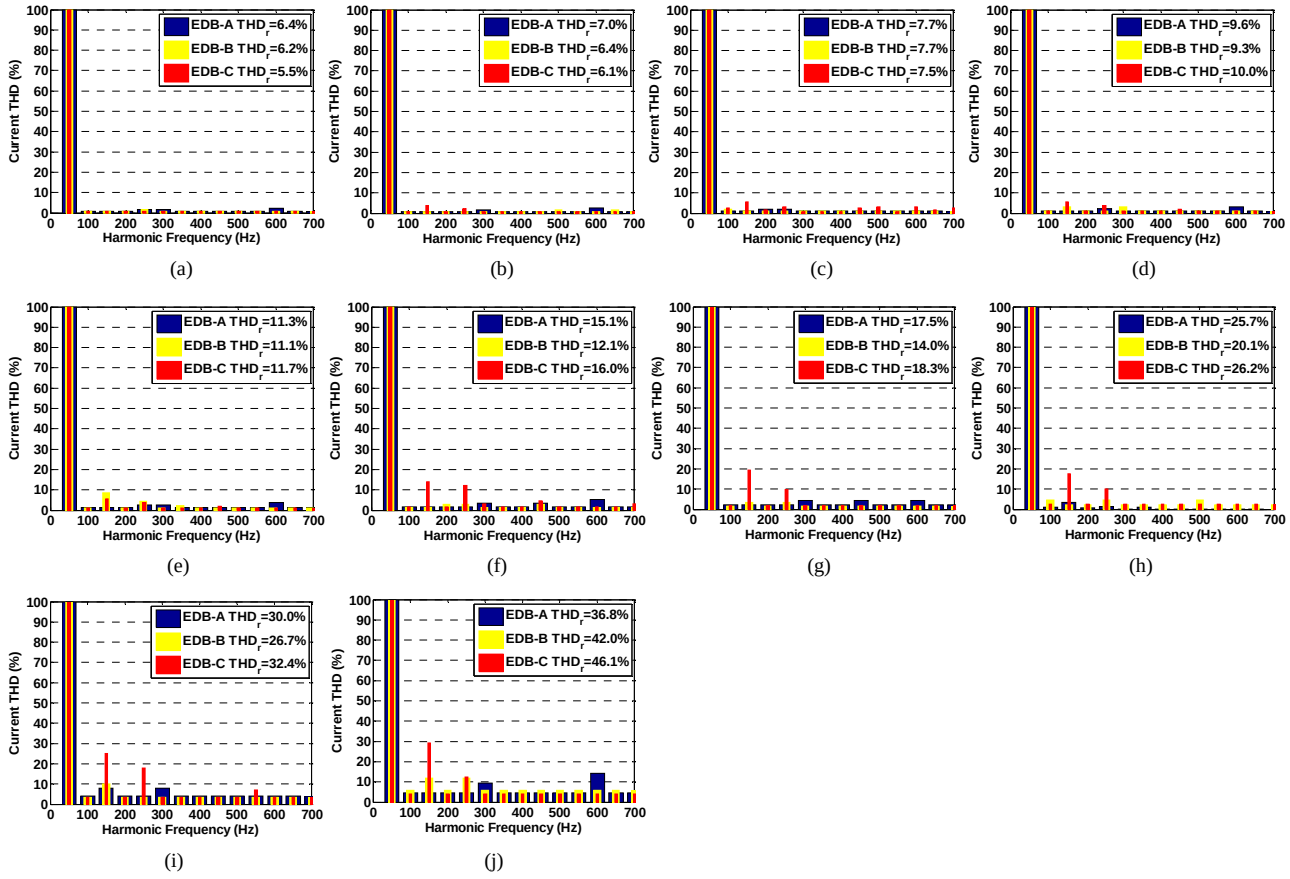

Figure 2. Current harmonic spectra at decreasing ballast dimming voltages a) 10V b) 9 V c) 8v d) 7v e) 6v f) 5v g) 4V h) 3V i) 2V j) 1V

Figure 1(f) demonstrates the deterioration of power factor with reduction in control voltage. The power factor reduces from approximately 0.98 to 0.83, 0.8 and 0.78 for EDB-A, EDB-B and EDB-C lighting system respectively. This decline in power factor is attributed to surfacing of lower odd order harmonics during dimming. The influence of dimming on power quality is discussed in next Subsection 4.1.1. A mathematical relationship between power factor and harmonics is given by Equation (1) [18].

$$p.f = \frac{1}{\sqrt{1+THD^2}}\cos(\phi) \qquad (1)$$

Additionally, the electricity supply companies require that the power factor at which the supply is used shall be maintained at not less than 0.9 lagging. Referring to Figure 1(e), for dimming voltages below 3V power factor of the tested ballasts lies below 0.9.

4.1.1 Power Quality

Power quality issues are concerned with growing presence of line harmonic distortions characterized by poor power factor. Harmonics are frequencies that are integral multiples of the fundamental frequency. Harmonics emanate whenever the supply wave shape is distorted from a pure sine wave. In electronic ballast system, the narrow current pulses drawn by the conventional rectifier-capacitor type interface is rich in harmonics [19]. A common measure of distortion in current and voltage is defined by percentage Total Harmonic Distortion.

Industry standards for harmonic current distortion from electronic lamp systems have not been formally established [20]. ANSI C82.77 sets a maximum current THD limit of 32% for the lighting equipment [21]. According to IEEE 519 and IEC 61000-3-2 [22,23], the current THD and voltage THD limits for electronic ballasts is 20% and 5% respectively. Current and voltage harmonic spectra for the different lamps used in the study are presented in Figure 2 and Figure 3 respectively. Though the investigated ballasts were equipped with harmonic suppression filters by the manufacturers; the significantly distorted current during dimming is possibly owed to the construction me- thod in order to decrease the ballast size and cost. The bar Figures 2(a)–(j) shows the individual harmonic distortion expressed in percent of the fundamental current as defined by the formula in Equation (2)

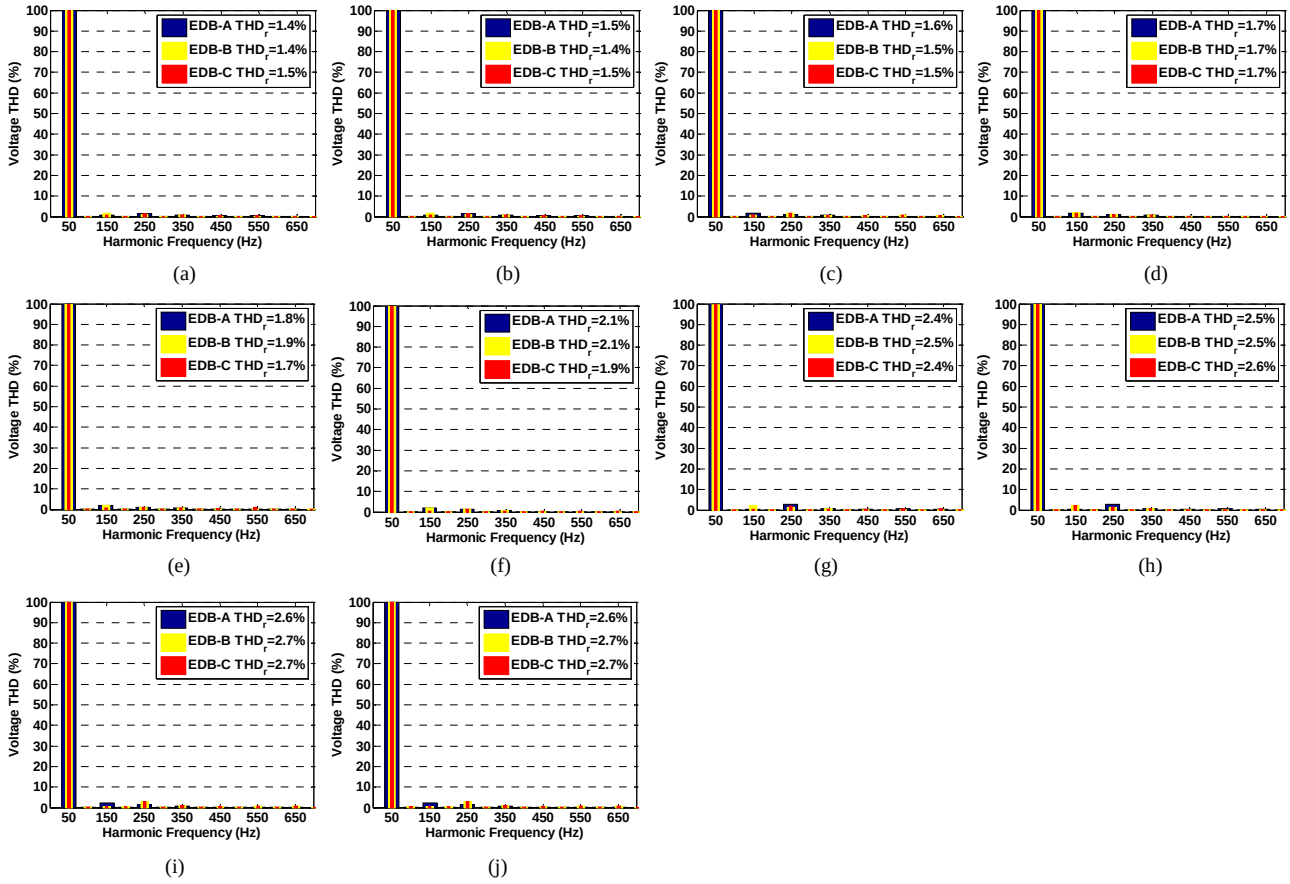

Figure 3. Voltage harmonic spectra at decreasing ballast dimming voltages a) 10V b) 9 V c) 8v d) 7v e) 6v f) 5v g) 4V h) 3V i) 2V j) 1V

$$THD = \frac{\sqrt{\sum_{n=2}^{14} I_n^{\,2}}}{I_1} \qquad (2)$$

As depicted in Figure 2(a) through (j) when the lamps are dimmed down from 10V to 1V the spectrum of current is characterized by emergence and elevation of magnitudes of third and fifth order harmonic components while dimming. Ballast B accounts a lower current THD (except at 1V) compared to other ballast A and ballast C. On an average for all the ballasts the line current THD increases from a minimum of 6.0% at 10V to maximum of 42.0 % at 1V. From the measurements results, it is clear that for the reported ballasts; THD in current lies within recommended IEEE 519 for control voltage above 3V. Similarly, for control voltage more than 2V current THD is less than ANSI C82.77 limits. Bar Figures 3(a)–(j) depicts the voltage harmonic spectra during lamp dimming down process. On an average for all the tested ballasts line voltage THD lies between 1.6% at 10V to 2.6% at 1V complying with IEEE 519 standard voltage limit of 5%. Additionally, it is observed during dimming that line current and line voltage crest factor is below 1.7.

4.2 Effect on Photometric Characteristics

Table 1 illustrates the influence of dimming on candela power distribution curves and CU values of luminaires under examination. Light distribution curves are curves defining variation of luminous intensity with angle of emission in a C 0-180 and C 90-270 plane, passing though centre of luminaire [24]. Furthermore specifiers use the coefficient of utilization chart to assess how effectively luminaire delivers light to a work plane. Referring to the polar curves presented in column 2 of Table 1; whilst dimming down from 10 to 1V, EDB-B has a lower light intensity compared to EDB-A and EDB-C. The candela power of the lamp EDB–A is downsized from approximately 2000 cd/1000 lm to approximately 65 cd/1000 lm. For EDB-B and EDB-C lamps the light intensity value decreases from approximately 1800 cd/ 1000lm to 60cd/ 1000lm. It is observed that there is not much deviation in the light distribution contour shape at different dimming levels. However, it is noticed that the light distribution pattern is slightly affected for control voltage less than 4V for EDB-C luminaire and below 2V for EDB-A and EDB-B lamps respectively, the luminaire efficiency while

Table 1. Effect of dimming on candela power distribution (II column) and on values of coefficient of utilization (III column) for each dc control voltage (I column)

Control Voltage	Light intensity curves (cd/1000lm)	Coefficient of Utilization (%)

10V

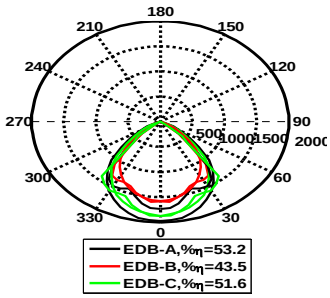

RC	80				70				50			30			10			0
RW	70	50	30	10	70	50	30	10	50	30	10	50	30	10	50	30	10	0
0	63	63	63	63	62	62	62	62	59	59	59	56	56	56	54	54	54	53
1	59	57	56	54	58	56	55	53	54	53	52	52	51	50	50	49	49	48
2	55	52	49	47	54	51	48	46	49	47	45	48	46	44	46	45	43	42
3	51	47	43	41	50	46	43	40	45	42	40	43	41	39	42	40	38	37
4	48	43	39	36	47	42	38	36	41	38	35	39	37	35	38	36	34	33
5	44	39	35	32	43	38	34	32	37	34	31	36	33	31	35	33	31	30
6	41	35	31	28	40	35	31	28	34	31	28	33	30	28	32	30	28	27
7	39	32	28	25	38	32	28	25	31	28	25	30	27	25	30	27	25	24
8	36	30	26	23	35	29	26	23	29	25	23	28	25	23	28	25	23	22
9	34	28	24	21	33	27	23	21	27	23	21	26	23	21	26	23	21	20
10	32	26	22	19	31	25	22	19	25	21	19	24	21	19	24	21	19	18

Effective Floor Cavity Reflectance 0.20

9V

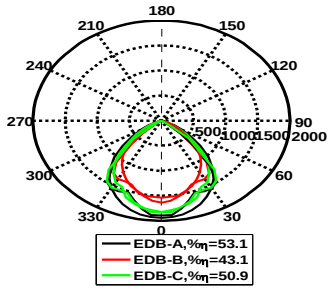

RC	80				70				50			30			10			0
RW	70	50	30	10	70	50	30	10	50	30	10	50	30	10	50	30	10	0
0	63	63	63	63	62	62	62	62	59	59	59	57	57	57	54	54	54	53
1	59	58	56	54	58	56	55	54	54	53	52	52	51	50	50	50	49	48
2	55	52	49	47	54	51	49	47	49	47	45	48	46	44	46	45	44	43
3	52	47	44	41	50	46	43	41	45	42	40	44	41	39	42	40	39	38
4	48	43	39	36	47	42	39	36	41	38	35	40	37	35	39	36	35	34
5	45	39	35	32	44	38	35	32	37	34	32	36	34	31	35	33	31	30
6	42	36	32	29	41	35	31	29	34	31	28	33	30	28	33	30	28	27
7	39	33	29	26	38	32	28	26	32	28	26	31	28	25	30	27	25	24
8	36	30	26	23	36	30	26	23	29	26	23	28	25	23	28	25	23	22
9	34	28	24	21	33	28	24	21	27	24	21	26	23	21	26	23	21	20
10	32	26	22	20	31	26	22	19	25	22	19	25	22	19	24	21	19	18

Effective Floor Cavity Reflectance 0.20

8V

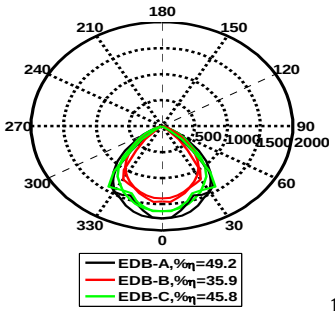

RC	80				70				50			30			10			0
RW	70	50	30	10	70	50	30	10	50	30	10	50	30	10	50	30	10	0
0	59	59	59	59	57	57	57	57	55	55	55	52	52	52	50	50	50	49
1	55	53	52	50	54	52	51	50	50	49	48	48	47	47	47	46	45	44
2	51	48	46	44	50	47	45	43	46	44	42	44	43	41	43	41	40	39
3	48	44	40	38	47	43	40	38	42	39	37	40	38	36	39	37	36	35
4	44	40	36	33	43	39	36	33	38	35	33	37	34	32	36	34	32	31
5	41	36	32	30	40	36	32	30	35	32	29	34	31	29	33	31	29	28
6	39	33	29	27	38	33	29	26	32	29	26	31	28	26	30	28	26	25
7	36	30	27	24	35	30	26	24	29	26	24	28	26	24	28	25	23	23
8	34	28	24	22	33	28	24	22	27	24	21	26	23	21	26	23	21	20
9	32	26	22	20	31	25	22	20	25	22	20	24	22	20	24	21	19	19
10	30	24	20	18	29	24	20	18	23	20	18	23	20	18	22	20	18	17

Effective Floor Cavity Reflectance 0.20

7V

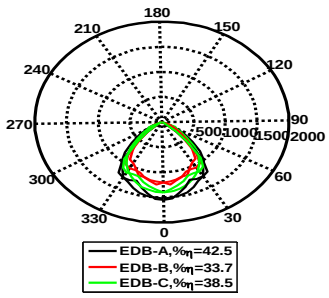

RC	80				70				50			30			10			0
RW	70	50	30	10	70	50	30	10	50	30	10	50	30	10	50	30	10	0
0	51	51	51	51	49	49	49	49	47	47	47	45	45	45	43	43	43	43
1	48	46	45	44	46	45	44	43	43	42	41	42	41	40	40	40	39	38
2	44	42	39	38	43	41	39	37	39	38	36	38	37	36	37	36	35	34
3	41	38	35	33	40	37	35	33	36	34	32	35	33	31	34	32	31	30
4	38	34	31	29	37	34	31	29	33	30	28	32	30	28	31	29	28	27
5	36	31	28	26	35	31	28	26	30	27	25	29	27	25	28	26	25	24
6	33	28	25	23	33	28	25	23	27	25	23	27	24	22	26	24	22	22
7	31	26	23	21	30	26	23	21	25	22	20	25	22	20	24	22	20	19
8	29	24	21	19	28	24	21	19	23	21	19	23	20	18	22	20	18	18
9	27	22	19	17	27	22	19	17	22	19	17	21	19	17	21	18	17	16
10	26	21	18	16	25	20	18	16	20	17	16	20	17	15	19	17	15	15

Effective Floor Cavity Reflectance 0.20

6V

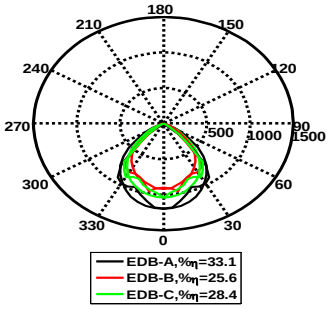

RC	80				70				50				30				10				0
RW	70	50	30	10	70	50	30	10	50	30	10		50	30	10		50	30	10		0
0	39	39	39	39	38	38	38	38	37	37	37		35	35	35		34	34	34		33
1	37	36	35	34	36	35	34	33	34	33	32		32	32	31		31	31	30		30
2	34	32	31	29	34	32	30	29	31	29	28		30	29	28		29	28	27		26
3	32	29	27	26	31	29	27	25	28	26	25		27	26	24		26	25	24		23
4	30	27	24	22	29	26	24	22	25	24	22		25	23	22		24	23	22		21
5	28	24	22	20	27	24	22	20	23	21	20		23	21	19		22	21	19		19
6	26	22	20	18	25	22	19	18	21	19	18		21	19	18		20	19	17		17
7	24	20	18	16	24	20	18	16	20	17	16		19	17	16		19	17	16		15
8	23	19	16	15	22	18	16	15	18	16	14		18	16	14		17	16	14		14
9	21	17	15	13	21	17	15	13	17	15	13		16	14	13		16	14	13		13
10	20	16	14	12	20	16	14	12	16	14	12		15	13	12		15	13	12		11

Effective Floor Cavity Reflectance 0.20

5V

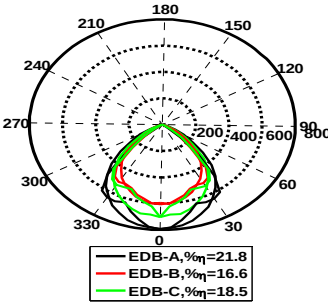

RC	80				70				50				30				10				0
RW	70	50	30	10	70	50	30	10	50	30	10		50	30	10		50	30	10		0
0	26	26	26	26	25	25	25	25	24	24	24		23	23	23		22	22	22		22
1	24	24	23	22	24	23	23	22	22	22	21		21	21	21		21	20	20		20
2	23	21	20	19	22	21	20	19	20	19	19		20	19	18		19	18	18		17
3	21	19	18	17	21	19	18	17	18	17	16		18	17	16		17	17	16		15
4	20	18	16	15	19	17	16	15	17	16	15		16	15	14		16	15	14		14
5	18	16	14	13	18	16	14	13	15	14	13		15	14	13		15	14	13		12
6	17	15	13	12	17	14	13	12	14	13	12		14	12	12		13	12	11		11
7	16	13	12	11	16	13	12	11	13	12	10		13	11	10		12	11	10		10
8	15	12	11	10	15	12	11	10	12	11	10		12	10	9		11	10	9		9
9	14	11	10	9	14	11	10	9	11	10	9		11	10	9		11	9	9		8
10	13	11	9	8	13	10	9	8	10	9	8		10	9	8		10	9	8		8

Effective Floor Cavity Reflectance 0.20

4V

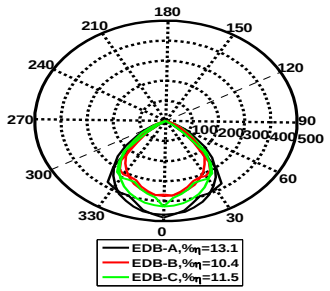

RC	80				70				50				30				10				0
RW	70	50	30	10	70	50	30	10	50	30	10		50	30	10		50	30	10		0
0	16	16	16	16	15	15	15	15	15	15	15		14	14	14		13	13	13		13
1	15	14	14	13	14	14	14	13	13	13	13		13	13	12		12	12	12		12
2	14	13	12	12	13	13	12	12	12	12	11		12	11	11		11	11	11		11
3	13	12	11	10	12	11	11	10	11	10	10		11	10	10		10	10	10		9
4	12	11	10	9	12	10	10	9	10	9	9		10	9	9		10	9	9		8
5	11	10	9	8	11	10	9	8	9	8	8		9	8	8		9	8	8		7
6	10	9	8	7	10	9	8	7	8	8	7		8	8	7		8	7	7		7
7	10	8	7	6	9	8	7	6	8	7	6		8	7	6		7	7	6		6
8	9	7	6	6	9	7	6	6	7	6	6		7	6	6		7	6	6		5
9	8	7	6	5	8	7	6	5	7	6	5		7	6	5		6	6	5		5
10	8	6	5	5	8	6	5	5	6	5	5		6	5	5		6	5	5		5

Effective Floor Cavity Reflectance 0.20

3V

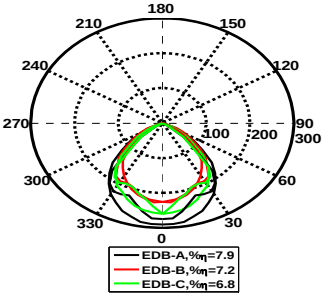

RC	80				70				50				30				10				0
RW	70	50	30	10	70	50	30	10	50	30	10		50	30	10		50	30	10		0
0	9	9	9	9	9	9	9	9	9	9	9		8	8	8		8	8	8		8
1	9	9	8	8	9	8	8	8	8	8	8		8	8	7		7	7	7		7
2	8	8	7	7	8	8	7	7	7	7	7		7	7	7		7	7	6		6
3	8	7	6	6	7	7	6	6	7	6	6		6	6	6		6	6	6		6
4	7	6	6	5	7	6	6	5	6	6	5		6	6	5		6	5	5		5
5	7	6	5	5	6	6	5	5	6	5	5		5	5	5		5	5	5		4
6	6	5	5	4	6	5	5	4	5	5	4		5	5	4		5	4	4		4
7	6	5	4	4	6	5	4	4	5	4	4		5	4	4		4	4	4		4
8	5	4	4	3	5	4	4	3	4	4	3		4	4	3		4	4	3		3
9	5	4	4	3	5	4	4	3	4	3	3		4	3	3		4	3	3		3
10	5	4	3	3	5	4	3	3	4	3	3		4	3	3		4	3	3		3

Effective Floor Cavity Reflectance 0.20

2V

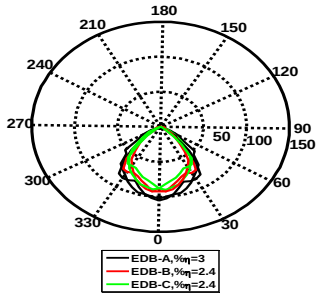

RC	80				70				50			30			10			0
RW	70	50	30	10	70	50	30	10	50	30	10	50	30	10	50	30	10	0
0	4	4	4	4	3	3	3	3	3	3	3	3	3	3	3	3	3	3
1	3	3	3	3	3	3	3	3	3	3	3	3	3	3	3	3	3	3
2	3	3	3	3	3	3	3	3	3	3	3	3	3	2	3	3	2	2
3	3	3	2	2	3	3	2	2	3	2	2	2	2	2	2	2	2	2
4	3	2	2	2	3	2	2	2	2	2	2	2	2	2	2	2	2	2
5	2	2	2	2	2	2	2	2	2	2	2	2	2	2	2	2	2	2
6	2	2	2	2	2	2	2	2	2	2	2	2	2	2	2	2	2	1
7	2	2	2	1	2	2	2	1	2	2	1	2	2	1	2	2	1	1
8	2	2	1	1	2	2	1	1	2	1	1	2	1	1	2	1	1	1
9	2	2	1	1	2	2	1	1	1	1	1	1	1	1	1	1	1	1
10	2	1	1	1	2	1	1	1	1	1	1	1	1	1	1	1	1	1

Effective Floor Cavity Reflectance 0.20

1V

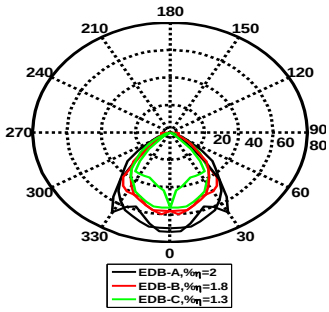

RC	80				70				50			30			10			0
RW	70	50	30	10	70	50	30	10	50	30	10	50	30	10	50	30	10	0
0	2	2	2	2	2	2	2	2	2	2	2	2	2	2	2	2	2	2
1	2	2	2	2	2	2	2	2	2	2	2	2	2	2	2	2	2	2
2	2	2	2	2	2	2	2	2	2	2	2	2	2	2	2	2	2	2
3	2	2	2	2	2	2	2	2	2	2	2	2	2	1	2	2	1	1
4	2	2	1	1	2	2	1	1	2	1	1	1	1	1	1	1	1	1
5	2	1	1	1	2	1	1	1	1	1	1	1	1	1	1	1	1	1
6	2	1	1	1	2	1	1	1	1	1	1	1	1	1	1	1	1	1
7	1	1	1	1	1	1	1	1	1	1	1	1	1	1	1	1	1	1
8	1	1	1	1	1	1	1	1	1	1	1	1	1	1	1	1	1	1
9	1	1	1	1	1	1	1	1	1	1	1	1	1	1	1	1	1	1
10	1	1	1	1	1	1	1	1	1	1	1	1	1	1	1	1	1	1

Effective Floor Cavity Reflectance 0.20

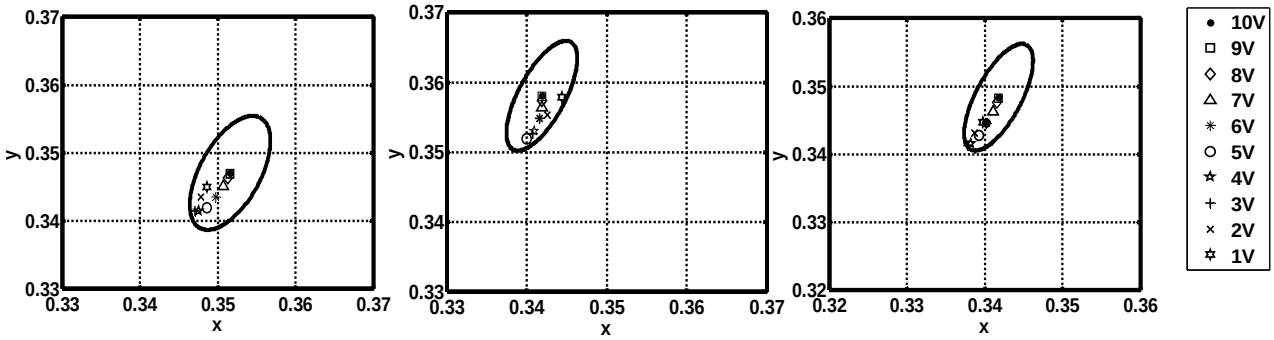

Figure 4. Chromaticity diagrams and Mac Adam ellipses for a)EDB-A b) EDB-B and c) EDB-C lamps

dimming down drops from a maximum of 53.2%, 43.5% and 51.6% to a minimum of 2%, 18%, 1.8% for EDB-A, EDB-B, EDB-C respectively due to decrease in the ballast control voltage. Taking the representative case of EDB-A luminaire, tabulated percentage CU values generated by AGI-32 Photometric toolbox is shown in third column of Table 1 against each ballast control voltage. The row labeled RC is the effective ceiling reflectance, the row labeled RW is the wall reflectance and the first column is the Room Cavity Ratio. For the indicated ceiling, wall and room cavity ratios, the tabulation shows the percentage of utilized lumens on the work plane. Clearly, percentage CU value of the luminaire depreciates with the reduction in the control voltage.

4.2.1 Chromaticity and CCT

Chromaticity values are customarily used for characterizing the color appearance of a light source. A metric commonly used for quantifying perceivable color difference is the MacAdam ellipse, which is a contour in the chromaticity diagram [25]. The ANSI specifies a 4-step MacAdam ellipse as the acceptable chromaticity tolerance area for certain types of fluorescent lamps [26]. Almost all color-normal subjects will perceive a color difference in source if the chromaticity coordinates of experimental light source in the course of dimming; falls beyond chromaticity tolerance area. Using the chromaticity coordinates of maximum output as the centre of the ellipse, 4 steps MacAdam ellipse plotted for the reported ballasts are shown in Figure 4 (a) through (c). As can be

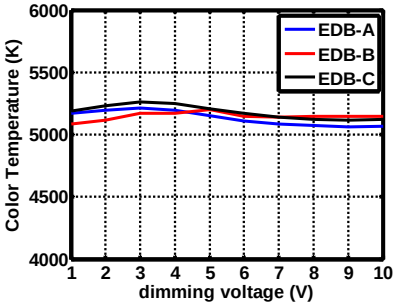

Figure 5. CCT(K) versus ballast analog control voltage

seen from the Figure 4 all the experimental lamps in question subjected to dimming confines their chromaticity shift within 4-step MacAdam ellipse. Further it is noticed that X- Y chromaticity coordinates remain essentially constant throughout the dimming range. Figure 5 indicates the relative CCT shift for various dimming control voltage of the ballast. It is observed that there is no appreciable deflection in CCT all through the dimming voltage range.

4.3 Effect on Visual Performance

This section highlights on the influence of fluorescent lamp dimming systems on quantity and quality of interior illuminance. Figure 6 (a) through (j) portrays the simulated view of standard office room (2.0×2.0×3.0m) rendered by Relux lighting simulation software. In addition Matlab generated 3D mesh plot of interior horizontal illuminance for each control voltage of the ballast is illustrated in Figures 6(a)–(j). Reflections of the floors, walls and ceiling are considered to be diffuse with reflection coefficients of 0.3, 0.5 and 0.7 respectively. For elucidation, this paper documents the artificial lighting analysis just with EDB-A luminaire. The results presented in this section concentrates on impact of T8 fluorescent lamp dimming on quantity of quality of artificial lighting without daylight intervention into the experimental room under examination. Further, the assessment of perceived discomfort glare due to lighting is not taken into consideration. The simulated 3D illuminance takes into account 0.5m offset from the walls at a horizontal working plane 0.7m above the floor. The recommended visual performance criterion advocates a minimum average illuminance value at the workplane as 300 lx and uniformity (ratio of minimum illuminance to average illuminance) above 0.8[27,28]. Rendered scenes depicted in Figure 6(a)-(j) disclose that there is no perceptible difference in the appearance of the light as well as general appearance of the interior especially related to color. The reason may be that, there is no significant deflection in CCT as well as light distribution pattern of lamp all through dimming as highlighted in the previous sections. However in practical schemes the general brightness of the room depreciates slightly during dimming which could be perceived by the normal observer. This is due to the fact that many working interiors appear dim for illuminance value lower than 200 lx which is the minimum recommended illuminance for a work space. As represented in Figure 6, illuminance value lower than 200 lx manifests for dimming voltages beneath 6V. Nevertheless through out dimming uniformity of illuminance in the whole interior stays above 0.8 as displayed in illuminance distribution plots of Figures 6(a)–(j).

5. Conclusions

As an energy conservation strategy, dimming controls for electric lighting have been one of the mainstays of the effort to use daylighting. In view of this, the present communication experimentally examined the fluorescent lamp dimming implications on performance characteristics of lighting systems from non manufacturer's perspective. The purpose was to discover acceptable range of dimming control voltage that would gratify both electrical and photometric performance of luminaire. We recognize that there may be a few high frequency electronic dimmable ballasts which are indeed as per national /international specifications. However, our conclusions are limited to the ballasts obtained from afore mentioned manufacturers for our experiments. The following salient points can be gleaned from the experimental results presented in this paper:

- The measurement on electrical characteristics shows, all the tested lamps could be dimmed down from 100% to 1% of light output with a power consumption of approximately 20% at 1V d.c. Further, neither the lamp flickers nor extinguishes even at minimum control voltage of 0V d.c. During dimming down on an average current THD and voltage THD rises from approximately 6.0% to 45% and 1.4% to 2.7% respectively. As a consequence the power factor deteriorates from approximately 0.98 at 10V to 0.8 at 1V.
- With respect to photometric performance characteristics, it is inferred that during dimming there is no significant variation in light intensity distribution pattern, CCT and chromaticity shift. On an average for all the tested lamps, the light intensity value drops off from approximately 2000 cd/1000lm to approximately 25cd/1000lm. There is also a significant drop in utilization factor values during dimming. The desired limits of utilization factor depend on task application.
- Rendered simulation results depict no significant variation in visual performance characteristics during dimming as; standards prescribed illuminance uniformity criterion of 0.8 is met. During dimming, average illuminance value dwindles from approximately 520 lx to 20 lx. However, in practical schemes the interiors appear dim for illuminance values lower than 200lx. Therefore, the judgment of desired lux level for a range of dimming

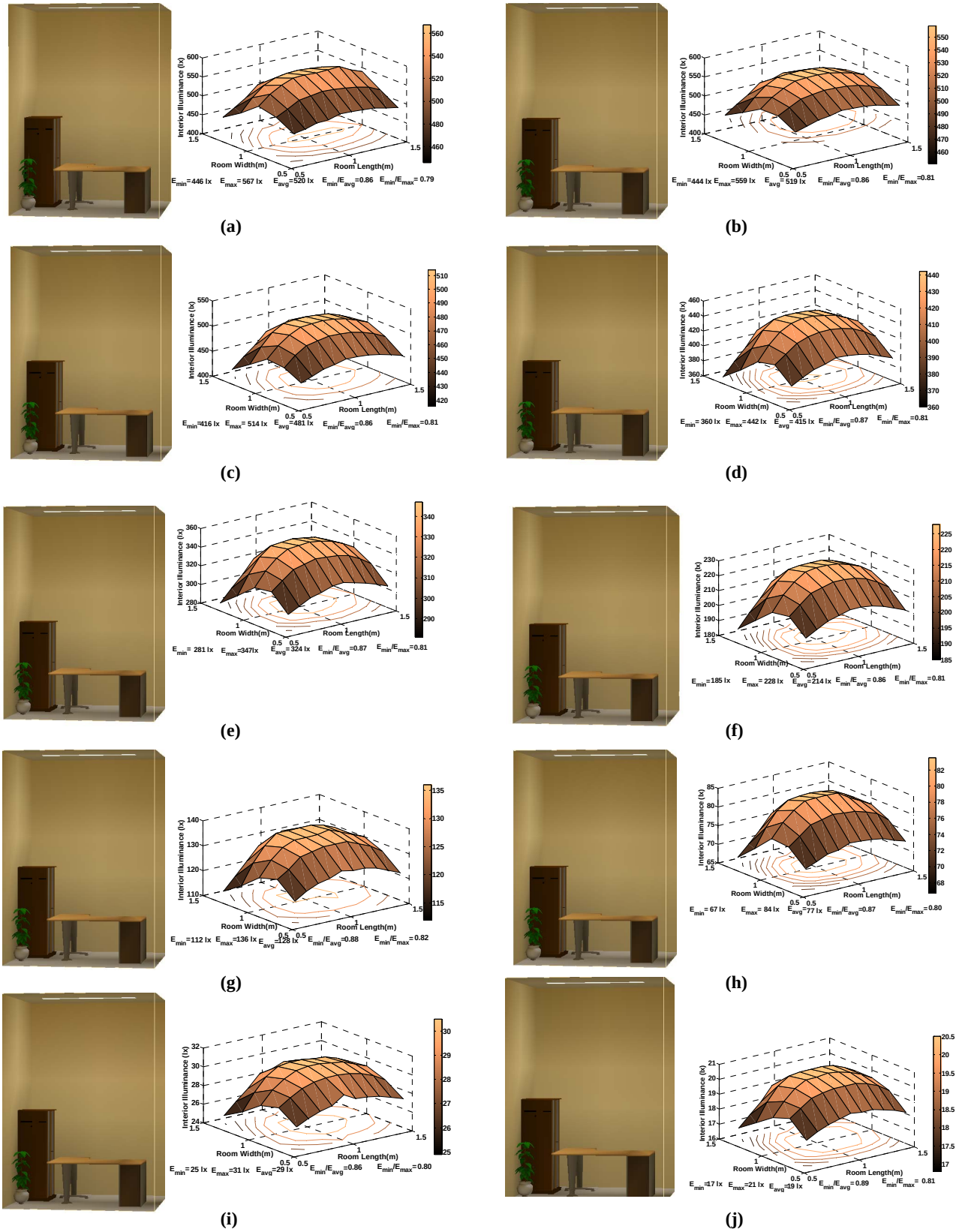

Figure 6. Visualizing image and corresponding mesh plot of illuminance distribution depicts the influence of dimming on quality and quantity of interior lighting at each dimming voltage a) 10V b) 9 V c)8v d)7v e) 6v f) 5v g) 4V h) 3V i) 2V j) 1V

control voltage requires particular attention based on task application.

In summary it is concluded from our experimental analysis that in order to achieve superior electrical, photometric as well as visual performance from a luminaire; the optimum control voltage range of ballast dimming should preferably lie between 10V to 3V d.c. The laboratory result of this paper demonstrate that fluorescent lamp dimming schemes are not an obstacle for wider use of energy efficient daylight artificial light integrated schemes.

6. Acknowledgements

The present research is funded by Department of Science & Technology under WOS-A scheme, Government of India. The authors gratefully acknowledge this contribution. Any opinions, findings and conclusions or recommendations expressed in this material are of the authors.

REFERENCES

[1] S. G. Colaco, C. P. Kurian, V. I. George, and A. M. Colaco, "Prospective techniques of effective daylight harvesting in commercial buildings by employing window glazing, dynamic shading devices and dimming control-A literature review," Building Simulation, Vol. 1, No. 4. P. 279–289, 2008.

[2] C. P. Kurian, R. S. Aithal, J. Bhat, and V. I. George, "Robust control and optimization of energy consumption in daylight-Artificial light integrated schemes," Lighting Research and Technology, Vol. 40, No. 4, pp. 7–24, 2008.

[3] M. S. Rea, "Lighting handbook: Reference and application," Illuminating Engineering Society of North America (IESNA), 9th Edition, New York, 2000.

[4] C. D. Louie, "Linear fluorescent dimming ballasts: Technology, methods," Protocols Lighting Controls Association, 2004, http://www.aboutlightingcontrols.org/education/papers/dimming.shtml)

[5] E. Tetri and V. Gligor, "Dimming according to daylight-effect on lamp life," Right Light 5, Proceedings of the 5th European Conference on Energy-Efficient Lighting. Nice, France, pp. 421–424, 2002.

[6] Y. Akashi and J. Neches, "Detectability and acceptability of. illuminance reduction for load shedding," Journal of Illuminating Engineering Society, Vol. 33, No. 1, pp. 3–13, 2004.

[7] M. Etezadi-Amoli and T. Florence, "Power factor and harmonic distortion characteristics of energy efficient lamps," IEEE Transactions on Power Delivery lamps, Vol. 4, No. 3, pp. 1965–1969, 1989.

[8] J. Yunfen, D. Robert, C. O'Rourke, E. Wai Mun Chui, "Compatibility testing of fluorescent lamp and ballast systems," IEEE Transactions on Industry Applications Vol. 35, No. 6, pp. 1271–1276, 1999.

[9] "Dimming Electronic Ballasts," National Lighting Product Information Program Specifier Reports, Troy, Lighting Research Center, NY, Rensselaer Polytechnic Institute, Vol. 7, No. 3, October 1999.

[10] R. Benoit, A. Deneyer, P. D'Herdt, and S. M. Diga, "Performance evaluation of dimmable lighting sources with fluorescent tubes for indoor applications," Proceedings of International Lighting Symposium, Modern Quality Solutions for an Efficient Lighting, Sinaia, Romania, October 12–14, 2006

[11] L. Doulos, A. Tsangrassoulis, and F. Topalis, "Quantifying energy savings in daylight responsive systems: The role of dimming electronic ballasts," Energy and Buildings, Vol. 40, No. 1, pp. 36–50, 2008.

[12] Commission internationale de l'éclairage, "The measurement of absolute luminous intensity distributions," CIE Technical Report, No. 70, 1987.

[13] Commission internationale de l'éclairage, "The photometry and goniophotometery of luminaires," CIE Technical Report, No. 121, 1996.

[14] Illuminating Engineering Society of North America (1999), IESNA guide to lamp seasoning, IES committee on testing procedures IES LM-54- 9,. New York.

[15] Illuminating Engineering Society of North America, "IESNA approved method for electrical and photometric measurements of fluorescent lamps," IES comitee on testing procedures IES LM-9-99, New York, 1999.

[16] Matlab R2009a version 7.5 user manual, http://www.mathworks.com.

[17] A. Choi, K. Song, and Y. Kim, "The characteristics of photosensors and electronic dimming ballasts in daylight responsive dimming systems," Building and Environment, Vol. 40, pp. 39–50, 2005

[18] F. V. Topalis, "Efficiency of energy saving lamps and harmonic distortion in distribution systems," IEEE Transactions on Power Delivery, Vol. 8, No. 4, pp. 2038–2042, 1993.

[19] T. Jednacz, "Power quality design implications of high frequency lighting ballasts and controls," Industry Applications Society Annual Meeting, Vol. 2, pp. 1833–1835, 1991.

[20] R. Wolsey, "Lighting answers: power quality," Lighting Research Center, Rensselaer Polytechnic Institute, Vol. 2, No. 2, 1995, http://www.sdeg.org/docs/LAPQ.pdf.

[21] Harmonic Emission Limits—Related Power Quality Requirements for Lighting, American National Standards Institute (ANSI), C82.77, New York, 1993.

[22] IEEE recommended practice and requirements for harmonic control in electrical power systems, IEEE standard pp. 519, 1992

[23] Limits for harmonic current emission equipment input current ≤16A per phase (2004) International Electrotechnical Commission (IEC) Edition 2.2

[24] C. P. Kurian, R. S. Aithal, and S. G. Colaco, "Performance evaluation of lamp-luminaire combination: A software approach using MATLAB," Journal of Institution of

Engineers, Vol. 85, pp. 98–101, 2004.

[25] G. Wyszecki and W. S. Stiles, Color Science, Wiley, New York, 1982.

[26] "American national standard for electric lamps: Specifications for the chromaticity of fluorescent lamps," American National Standards Institute (ANSI) C78.376, National Electrical Manufacturers Association, Rosslyn, VA, 2001.

[27] Code Bureau of Indian Standards, Code of practice for interior illumination: Part 1 General requirements and recommendations for working interiors IS 3646, Part 1, Section 0, 1992, Reaffirmed 2003

[28] R. Yarham, Code for Interior Lighting Chartered Institution of Building Services Engineers (CIBSE), London, 1994.

Nomenclatures:

η	Luminaire efficiency
$\cos(\phi)$	Cosine of the phase angle between input voltage and current.
I_1	Fundamental current (A)
I_n	Current at harmonic order number n
pf	Power factor given by $\cos(\phi)$
THD	Total Harmonic Distortion
CCT	Correlated Color Temperature (K)
CU	Coefficient of Utilization
E_{min}	Minimum Illuminance (lx)
E_{max}	Maximum Illuminance (lx)
E_{avg}	Average Illuminance (lx)

Energy and Power Engineering, **2010, 65-72**
doi:10.4236/epe.2010.21010 Published Online February 2010 (http://www.scirp.org/journal/epe)

Scaling Laws for Plasma Focus Machines from Numerical Experiments

S. H. SAW[1,2], S. LEE[1,2,3]
[1]*INTI University College, Nilai, Malaysia*
[2]*Institute for Plasma Focus Studies,* 32 *Oakpark Drive, Chadstone, Australia*
[3]*NSSE, National Institute of Education, Nanyang Technological University, Singapore*
Email: *leesing@optusnet.com.au, saw_sorheoh@intimal.edu.my*

Abstract: Numerical experiments carried out systematically using the Lee Model code unveil insightful and practical wide-ranging scaling laws for plasma focus machines for nuclear fusion energy as well as other applications. An essential feature of the numerical experiments is the fitting of a measured current waveform to the computed waveform to calibrate the model for the particular machine, thus providing a reliable and rigorous determination of the all-important pinch current. The thermodynamics and radiation properties of the resulting plasma are then reliably determined. This paper provides an overview of the recently published scaling laws for neutron (Y_n) and neon soft x-ray, SXR (Y_{sxr}) yields:

$Y_n = 3.2\text{x}10^{11}\, I_{pinch}^{4.5}$; $Y_n = 1.8\text{x}10^{10}\, I_{peak}^{3.8}$; I_{peak} (0.3 to 5.7), I_{pinch} (0.2 to 2.4) in MA.
$Y_n \sim E_0^{2.0}$ at tens of kJ to $Y_n \sim E_0^{0.84}$ at MJ level (up to 25MJ) and
$Y_{sxr} = 8.3\text{x}10^{3}\, I_{pinch}^{3.6}$; $Y_{sxr} = 6\text{x}10^{2}\, I_{peak}^{3.2}$; I_{peak} (0.1 to 2.4), I_{pinch} (0.07 to1.3) in MA.
$Y_{sxr} \sim E_0^{1.6}$ (kJ range) to $Y_{sxr} \sim E_0^{0.8}$ (towards MJ).

Keywords: dense plasma focus, plasma focus scaling laws, neutron scaling laws, soft x-ray scaling laws, plasma focus modeling, Lee model code

1. Introduction

Plasma focus machines of various energies are increasingly being studied as sources of neutrons and soft x-rays. The most exciting prospect is for scaling the plasma focus up to regimes relevant for fusion energy studies. However, even a simple machine such as the UNU/ICTP PFF 3 kJ machine consistently produces 10^8 neutrons when operated in deuterium [1]. Plasma focus machines operated in neon have also been studied as intense sources of soft x-rays with potential applications [2–4]. Whilst many recent experiments have concentrated efforts on low energy devices [2–4] with a view of operating these as repetitive pulsed sources, other experiments have looked at x-ray pulses from larger plasma focus devices [5,6] extending to the MJ regime. Numerical experiments simulating x-ray pulses from plasma focus devices are also gaining more interest in the public domain. For example, the Institute of Plasma Focus Studies [7] conducted a recent international Internet Workshop on Plasma Focus Numerical Experiments [8], at which it was demonstrated that the Lee model code [9] not only computes realistic focus pinch parameters, but also absolute values of neutron yield Y_n and soft x-ray yield Y_{sxr} which are consistent with those measured experimentally. A comparison was made for the case of the NX2 machine [4], showing good agreement between computed and measured Y_{sxr} as a function of P_0 [8,10]. This gives confidence that the Lee model code gives realistic results in the computation of Y_n and Y_{sxr}.

In this paper, we show the comprehensive range of numerical experiments conducted to derive scaling laws on neutron yield Y_n [11,12] and neon Y_{sxr}, in terms of storage energy E_0, peak discharge current I_{peak} and peak focus pinch current I_{pinch} obtained from studies carried out over E_0 varying from 0.2 kJ to 25 MJ for optimised machine parameters and operating parameters. It is worth mentioning that the scaling laws in terms of I_{pinch} and I_{peak} have also been obtained for numerical experiments using the Lee model code fitted with the actual machine parameters and operating parameters and the difference from that obtained for the optimised conditions are within the order of 0.1 in the scaling laws power factor for neutrons and no change for neon SXR yield with I_{pinch}.

We also wish to point out that the distinction of I_{pinch} from I_{peak} is of basic importance [13–15]. The scaling with I_{pinch} is the more fundamental and robust one; since obviously there are situations (no pinching or poor pinching however optimized) where I_{peak} may be large but Y_n is zero or small; whereas the scaling with I_{pinch} is

certainly more consistent with all situations. In these works the primary importance of I_{pinch} for scaling plasma focus properties including neutron yield Y_n, has been firmly established [11–15].

2. The Lee Model Code

The Lee model code couples the electrical circuit with plasma focus dynamics, thermodynamics and radiation, enabling realistic simulation of all gross focus properties. The basic model, described in 1984 [16] was successfully used to assist several projects [17–19]. Radiation-coupled dynamics was included in the five-phase code leading to numerical experiments on radiation cooling [20]. The vital role of a finite small disturbance speed discussed by Potter in a Z-pinch situation [21] was incorporated together with real gas thermodynamics and radiation-yield terms. Before this 'communication delay effect' was incorporated, the model consistently overestimated the radial speeds. This is serious from the point of view of neutron yields. A factor of two in shock speeds gives a factor of four in temperatures leading to a difference in fusion cross-sections of~1000 at the range of temperatures we are dealing with. This version of the code assisted other research projects [22–27] and was web-published in 2000 [28] and 2005 [29]. Plasma self-absorption was included in 2007 [27] improving SXR yield simulation. The code has been used extensively in several machines including UNU/ICTP PFF [1, 17,22,23,25–27,30,31], NX2 [24,27,32], NX1 [3,32] and adapted for the Filippov-type plasma focus DENA [33]. A recent development is the inclusion of the neutron yield Y_n using a beam–target mechanism [11,12,14,15, 34], incorporated in recent versions [9] of the code (versions later than RADPFV5.13), resulting in realistic Y_n scaling with I_{pinch} [11,12]. The versatility and utility of the model are demonstrated in its clear distinction of I_{pinch} from I_{peak} [13] and the recent uncovering of a plasma focus pinch current limitation effect [14,15]. The description, theory, code and a broad range of results of this 'Universal Plasma Focus Laboratory Facility' are available for download from [9].

A brief description of the code is given below. The five phases are summarised as follows:

1) Axial Phase: Described by a snowplow model with an equation of motion coupled to a circuit equation. The equation of motion incorporates the axial phase model parameters: mass and current factors f_m and f_c respectively. The mass swept-up factor f_m accounts for not only the porosity of the current sheet but also for the inclination of the moving current sheet-shock front structure and all other unspecified effects which have effects equivalent to increasing or reducing the amount of mass in the moving structure during the axial phase. The current factor f_c accounts for the fraction of current effectively flowing in the moving structure (due to all effects such as current shedding at or near the back-wall and current sheet inclination). This defines the fraction of current effectively driving the structure during the axial phase.

2) Radial Inward Shock Phase: Described by four coupled equations using an elongating slug model. The first equation computes the radial inward shock speed from the driving magnetic pressure. The second equation computes the axial elongation speed of the column. The third equation computes the speed of the current sheath, also called the magnetic piston, allowing the current sheath to separate from the shock front by applying an adiabatic approximation. The fourth is the circuit equation. Thermodynamic effects due to ionization and excitation are incorporated into these equations, these effects being important for gases other than hydrogen and deuterium. Temperature and number densities are computed during this phase. A communication delay between shock front and current sheath due to the finite small disturbance speed is crucially implemented in this phase. The model parameters, radial phase mass swept-up and current factors f_{mr} and f_{cr} respectively are incorporated in all three radial phases. The mass swept-up factor f_{mr} accounts for all mechanisms which have effects equivalent to increasing or reducing the amount of mass in the moving slug during the radial phase. The current factor f_{cr} accounts for the fraction of current effectively flowing in the moving piston forming the back of the slug (due to all effects). This defines the fraction of current effectively driving the radial slug.

3) Radial Reflected Shock (RS) Phase: When the shock front hits the axis, because the focus plasma is collisional, a reflected shock develops which moves radially outwards, whilst the radial current sheath piston continues to move inwards. Four coupled equations are also used to describe this phase, these being for the reflected shock moving radially outwards, the piston moving radially inwards, the elongation of the annular column and the circuit. The same model parameters f_{mr} and f_{cr} are used as in the previous radial phase. The plasma temperature behind the RS undergoes a jump by a factor of approximately two.

4) Slow Compression (Quiescent) or Pinch Phase: When the out-going reflected shock hits the in-coming piston the compression enters a radiative phase, in which for gases such as neon radiation emission may actually enhance the compression, where we have included energy loss/gain terms from Joule heating and radiation losses into the piston equation of motion. Three coupled equations describe this phase; these being the piston radial motion equation, the pinch column elongation equation and the circuit equation, incorporating the same model parameters as in the previous two phases. Thermodynamic effects are incorporated into this phase. The duration of this slow compression phase is set as the time

of transit of small disturbances across the pinched plasma column. The computation of this phase is terminated at the end of this duration.

4) Expanded Column Phase: To simulate the current trace beyond this point, we allow the column to suddenly attain the radius of the anode, and use the expanded column inductance for further integration. In this final phase the snowplow model is used, and two coupled equations are used; similar to the axial phase above. This phase is not considered important as it occurs after the focus pinch.

2.1 Computation of Neutron Yield

The neutron yield is computed using a phenomenological beam-target neutron generating mechanism described recently by Gribkov *et al* [34] and adapted to yield the following equation. A beam of fast deuteron ions is produced by diode action in a thin layer close to the anode, with plasma disruptions generating the necessary high voltages. The beam interacts with the hot dense plasma of the focus pinch column to produce the fusion neutrons. The beam-target yield is derived [11,12,14,28] as:

$$Y_{b\text{-}t} = C_n\, n_i\, I_{pinch}{}^2 z_p{}^2 (ln\ (b/r_p)\ \sigma/U^{0.5} \qquad (1)$$

where n_i is the ion density, b is the cathode radius, r_p is the radius of the plasma pinch with length z_p, σ the cross-section of the D-D fusion reaction, n- branch [35] and U, the beam energy. C_n is treated as a calibration constant combining various constants in the derivation process.

The D-D cross-section is sensitive to the beam energy in the range 15–150kV; so it is necessary to use the appropriate range of beam energy to compute σ. The code computes induced voltages (due to current motion inductive effects) V_{max} of the order of only 15–50 kV. However it is known, from experiments that the ion energy responsible for the beam-target neutrons is in the range 50–150 keV [34], and for smaller lower-voltage machines the relevant energy could be lower at 30–60 keV [31]. Thus in line with experimental observations the D-D cross section σ is reasonably obtained by using $U=3V_{max}$. This fit was tested by using U equal to various multiples of V_{max}. A reasonably good fit of the computed neutron yields to the measured published neutron yields at energy levels from sub-kJ to near MJ was obtained when the multiple of 3 was used; with poor agreement for most of the data points when for example a multiple of 1 or 2 or 4 or 5 was used. The model uses a value of C_n=2.7x10^7 obtained by calibrating the yield [9,13,14] at an experimental point of 0.5 MA.

The thermonuclear component is also computed in every case and it is found that this component is negligible when compared with the beam-target component.

2.2 Computation of Neon SXR Yield

We note that the transition from Phase 4 to Phase 5 is observed in laboratory measurements to occur in an extremely short time with plasma/current disruptions resulting in localized regions of high densities and temperatures. These localized regions are not modelled in the code, which consequently computes only an average uniform density, and an average uniform temperature which are considerably lower than measured peak density and temperature. However, because the 4 model parameters are obtained by fitting the computed total current waveform to the measured total current waveform, the model incorporates the energy and mass balances equivalent, at least in the gross sense, to all the processes which are not even specifically modelled. Hence the computed gross features such as speeds and trajectories and integrated soft x-ray yields have been extensively tested in numerical experiments for several machines and are found to be comparable with measured values.

In the code [9], neon line radiation Q_L is calculated as follows:

$$\frac{dQ_L}{dt} = -4.6x10^{-31} n_i^2 Z Z_n^4 (\pi r_p^2) z_f / T \qquad (2)$$

where for the temperatures of interest in our experiments we take the SXR yield $Y_{sxr} = Q_L$. Z_n is the atomic number. Hence the SXR energy generated within the plasma pinch depends on the properties: number density n_i, effective charge number Z, pinch radius r_p, pinch length z_f and temperature T. It also depends on the pinch duration since in our code the Q_L is obtained by integrating over the pinch duration.

This generated energy is then reduced by the plasma self-absorption which depends primarily on density and temperature; the reduced quantity of energy is then emitted as the SXR yield. These effects are included in the modelling by computing volumetric plasma self-absorption factor A derived from the photonic excitation number M which is a function of Z_n, n_i, Z and T. However, in our range of operation, the numerical experiments show that the self absorption is not significant. It was first pointed out by Liu Mahe [23] that a temperature around 300 eV is optimum for SXR production. Shan Bing's subsequent work [24] and our experience through numerical experiments suggest that around 2x10^6 K (below 200 eV) or even a little lower could be better. Hence unlike the case of neutron scaling, for SXR scaling there is an optimum small range of temperatures (T windows) to operate.

3. Numerical Experiments

The Lee code is configured to work as any plasma focus by inputting the bank parameters, L_0, C_0 and stray circuit resistance r_0; the tube parameters b, a and z_0 and operational parameters V_0 and P_0 and the fill gas. The standard

practice is to fit the computed total current waveform to an experimentally measured total current waveform [11,13–15,28,29] using the four model parameters representing the mass swept-up factor f_m, the plasma current factor f_c for the axial phase and factors f_{mr} and f_{cr} for the radial phases.

From experience it is known that the current trace of the focus is one of the best indicators of gross performance. The axial and radial phase dynamics and the crucial energy transfer into the focus pinch are among the important information that is quickly apparent from the current trace.

The exact time profile of the total current trace is governed by the bank parameters, by the focus tube geometry and the operational parameters. It also depends on the fraction of mass swept-up and the fraction of sheath current and the variation of these fractions through the axial and radial phases. These parameters determine the axial and radial dynamics, specifically the axial and radial speeds which in turn affect the profile and magnitudes of the discharge current. The detailed profile of the discharge current during the pinch phase also reflects the Joule heating and radiative yields. At the end of the pinch phase the total current profile also reflects the sudden transition of the current flow from a constricted pinch to a large column flow. Thus the discharge current powers all dynamic, electrodynamic, thermodynamic and radiation processes in the various phases of the plasma focus. Conversely all the dynamic, electrodynamic, thermodynamic and radiation processes in the various phases of the plasma focus affect the discharge current. It is then no exaggeration to say that the discharge current waveform contains information on all the dynamic, electrodynamic, thermodynamic and radiation processes that occur in the various phases of the plasma focus. This explains the importance attached to matching the computed current trace to the measured current trace in the procedure adopted by the Lee model code.

3.1 Scaling Laws for Neutrons from Numerical Experiments over a Range of Energies from 10kJ to 25 MJ

We apply the Lee model code to the MJ machine PF1000 over a range of C_0 to study the neutrons emitted by PF1000-like bank energies from 10kJ to 25 MJ.

First, we fitted a measured current trace to obtain the model parameters. A measured current trace of the PF1000 with C_0 =1332 μF, operated at 27 kV, 3.5 torr deuterium, has been published [34], with cathode/anode radii b=16 cm, a=11.55 cm and anode length z_0=60cm. In the numerical experiments we fitted external (or static) inductance L_0= 33.5 nH and stray resistance r_0=6.1 mΩ (damping factor $RESF=r_0/(L_0/C_0)^{0.5}$=1.22). The fitted model parameters are: f_m=0.13, f_c=0.7, f_{mr}=0.35 and f_{cr}= 0.65. The computed current trace [11], [15] agrees very well with the measured trace through all the phases; axial and radial, right down to the bottom of the current dip indicating the end of the pinch phase as shown in Figure 1.

This agreement confirms the model parameters for the PF1000. Once the model parameters have been fitted to a machine for a given gas, these model parameters may be used with some degree of confidence when operating parameters such as the voltage are varied [9]. With no measured current waveforms available for the higher megajoule numerical experiments, it is reasonable to keep the model parameters that we have got from the PF1000 fitting.

This series of numerical experiments is carried out at 35 kV, 10 torr deuterium, inductance L_0= 33.5 nH, stray resistance r_0=6.1 mΩ (damping factor $RESF= r_0/(L_0/C_0)^{0.5}$=1.22). The ratio $c=b/a$ is retained at 1.39. The numerical experiments were carried out for C_0 ranging from 14 μF to 39960 μF corresponding to energies from 8.5 kJ to 24 MJ [12]. For each C_0, anode length z_0 is varied to find the optimum. For each z_0, anode radius a_0 is varied so that the end axial speed is 10 cm/μs.

For this series of experiments we find that the Y_n scaling changes from $Y_n \sim E_0^{2.0}$ at tens of kJ to $Y_n \sim E_0^{0.84}$ at the highest energies (up to 25MJ) investigated in this series. This is shown in Figure 2.

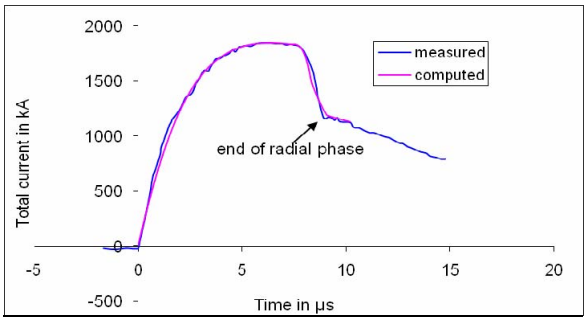

Figure 1. Current fitting of computed current to measured current traces to obtain fitted parameters f_m = 0.13, f_c = 0.7, f_{mr} = 0.35 and f_{cr}= 0.65

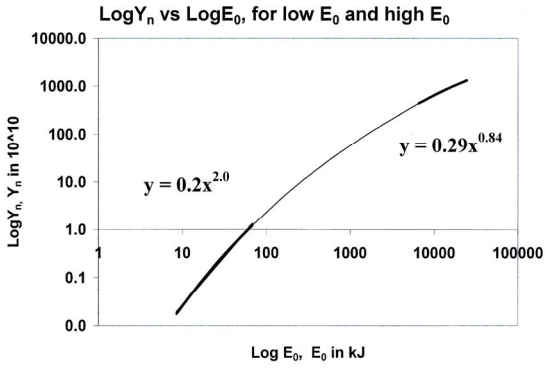

Figure 2. Y_n plotted as a function of E_0 in log-log scale, showing Y_n scaling changes from $Y_n \sim E_0^{2.0}$ at tens of kJ to $Y_n \sim E_0^{0.84}$ at the highest energies (up to 25MJ). The scaling deterioration observed in this Figure is discussed in the Conclusion section

The scaling of Y_n with I_{peak} and I_{pinch} over the whole range of energies investigated up to 25 MJ (Figure 3) is as follows:

$$Y_n = 3.2\text{x}10^{11} I_{pinch}^{4.5} \text{ and}$$

$$Y_n = 1.8\text{x}10^{10} I_{peak}^{3.8}$$

where I_{peak} ranges from 0.3 to 5.7 MA and I_{pinch} ranges from 0.2 to 2.4 MA.

This compares to an earlier study carried out on several machines with published current traces with Y_n yield measurements, operating conditions and machine parameters including the PF400, UNU/ICTP PFF, the NX2 and Poseidon providing a slightly higher scaling laws: $Y_n \sim I_{pinch}^{4.7}$ and $Y_n \sim I_{peak}^{3.9}$. The slightly higher value of the scaling is because those machines fitted are of mixed '*c*' mixed bank parameters, mixed model parameters and currents generally below 1MA and voltages generally below the 35 kV [11].

3.2 Scaling Laws for Neon SXR from Numerical Experiments over a Range of Energies from 0.2 kJ to 1 MJ

We next use the Lee model code to carry out a series of numerical experiments to obtain the soft x-ray yield in neon for bank energies from 0.2 kJ to 1 MJ [36]. In this case we apply it to a proposed modern fast plasma focus machine with optimised values for *c* the ratio of the outer to inner electrode radius and L_0 obtained from our numerical experiments.

The following parameters are kept constant: 1) the ratio $c=b/a$ (kept at 1.5, which is practically optimum according to our preliminary numerical trials; 2) the operating voltage V_0 (kept at 20 kV); 3) static inductance L_0 (kept at 30 nH, which is already low enough to reach the I_{pinch} limitation regime [13,14] over most of the range of E_0 we are covering) and; 4) the ratio of stray resistance to surge impedance *RESF* (kept at 0.1, representing a higher performance modern capacitor bank). The model parameters [8-14] f_m, f_c, f_{mr}, f_{cr} are also kept at fixed values 0.06, 0.7, 0.16 and 0.7. We choose the model parameters as they represent the average values from the range of machines that we have studied. A typical current waveform is shown in Figure 4.

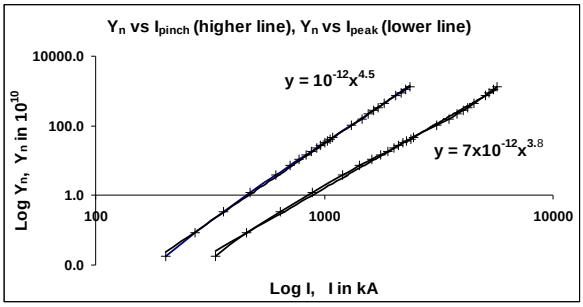

Figure 3. Log(Y_n) scaling with Log(I_{peak}) and Log(I_{pinch}), for the range of energies investigated, up to 25 MJ

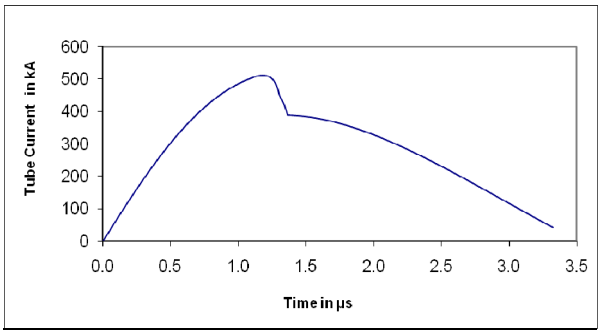

Figure 4. Computed total curent versus time for L_0=30 nH and V_0 = 20 kV, C_0 = 30 uF, *RESF* = 0.1, *c* = 1.5 and model parameters f_m, f_c, f_{mr}, f_{cr} are fixed at 0.06, 0.7, 0.16 and 0.7 for optimised *a* = 2.285cm and z_0 = 5.2cm

The storage energy E_0 is varied by changing the capacitance C_0. Parameters that are varied are operating pressure P_0, anode length z_0 and anode radius '*a*'. Parametric variation at each E_0 follows the order; P_0, z_0 and *a* until all realistic combinations of P_0, z_0 and *a* are investigated. At each E_0, the optimum combination of P_0, z_0 and *a* is found that produces the biggest Y_{sxr}. In other words at each E_0, a P_0 is fixed, a z_0 is chosen and *a* is varied until the largest Y_{sxr} is found. Then keeping the same values of E_0 and P_0, another z_0 is chosen and *a* is varied until the largest Y_{sxr} is found. This procedure is repeated until for that E_0 and P_0, the optimum combination of z_0 and *a* is found. Then keeping the same value of E_0, another P_0 is selected. The procedure for parametric variation of z_0 and *a* as described above is then carried out for this E_0 and new P_0 until the optimum combination of z_0 and *a* is found. This procedure is repeated until for a fixed value of E_0, the optimum combination of P_0, z_0 and *a* is found.

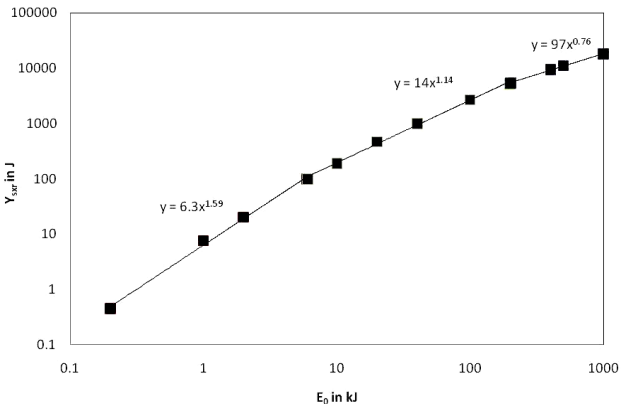

Figure 5. Y_{sxr} vs E_0. The parameters kept constants are: RESF=0.1, c=1.5, L_0=30nH and V_0=20 kV and model parameters f_m, f_c, f_{mr}, f_{cr} at 0.06, 0.7, 0.16 and 0.7 respectively. The scaling deterioration observed in this Figure is discussed in the Conclusion section

The procedure is then repeated with a new value of E_0. In this manner after systematically carrying out some 2000 runs, the optimized runs for various energies are obtained. A plot Y_{sxr} against E_0 is shown in Figure 5.

We then plot Y_{sxr} against I_{peak} and I_{pinch} and obtain SXR yield scales as Y_{sxr}~$I_{pinch}^{3.6}$ and Y_{sxr}~$I_{peak}^{3.2}$. The I_{pinch} scaling has less scatter than the I_{peak} scaling. We next subject the scaling to further test when the fixed parameters *RESF*, c, L_0 and V_0 and model parameters f_m, f_c, f_{mr}, f_{cr} are varied. We add in the results of some numerical experiments using the parameters of several existing plasma focus devices including the UNU/ICTP PFF (*RESF* =0.2, c =3.4, L_0=110 nH and V_0=14 kV with fitted model parameters f_m= 0.05, f_c= 0.7, f_{mr}= 0.2, f_{cr}= 0.8) [7-9], [23], the NX2 (*RESF* = 0.1, c = 2.2, L_0= 20 nH and V_0= 11 kV with fitted model parameters f_m= 0.06, f_c = 0.7, f_{mr}= 0.16, f_{cr}= 0.7) [7–10,24] and PF1000 (*RESF* = 0.1, c = 1.39, L_0= 33 nH and V_0= 27 kV with fitted model parameters f_m= 0.1, f_c= 0.7, f_{mr}= 0.15, f_{cr}= 0.7) [7–9,14]. These new data points (unblackened data points in Figure 6) contain wide ranges of c, V_0, L_0 and model parameters. The resulting Y_{sxr} versus I_{pinch} log-log curve remains a straight line, with the scaling index 3.6 unchanged and with no more scatter than before. However the resulting Y_{sxr} versus I_{peak} curve now exhibits considerably larger scatter and the scaling index has changed.

We would like to highlight that the consistent behaviour of I_{pinch} in maintaining the scaling of Y_{sxr}~ $I_{pinch}^{3.6}$ with less scatter than the Y_{sxr}~$I_{peak}^{3.2}$ scaling particularly when mixed-parameters cases are included, strongly support the conclusion that I_{pinch} scaling is the more universal and robust one. Similarly conclusions on the importance of I_{pinch} in plasma focus performance and scaling laws have been reported [11–15].

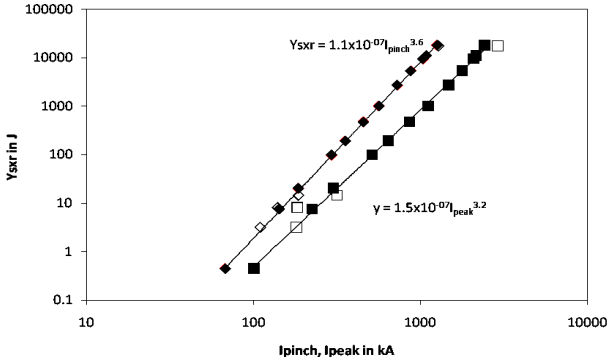

Figure 6. Y_{sxr} is plotted as a function of I_{pinch} and I_{peak}. The parameters kept constant for the black data points are: *RESF* = 0.1, c = 1.5, L_0 = 30nH and V_0 = 20 kV and model parameters f_m, f_c, f_{mr}, f_{cr} at 0.06, 0.7, 0.16 and 0.7 respectively. The unblackened data points are for specific machines which have different values for the parameters c, L_0, V_0 and *RESF*

It may also be worthy of note that our comprehensively surveyed numerical experiments for Mather configurations in the range of energies 0.2 kJ to 1 MJ produce an I_{pinch} scaling rule for Y_{sxr} not compatible with Gates' rule [37]. However it is remarkable that our I_{pinch} scaling index of 3.6, obtained through a set of comprehensive numerical experiments over a range of energies 0.2 kJ to 1 MJ, on Mather-type devices is within the range of 3.5to4 postulated on the basis of sparse experimental data, (basically just two machines one at 5 kJ and the other at 0.9 MJ), by Filippov [6], for Filippov configurations in the range of energies 5 kJ to 1 MJ.

It must be pointed out that the results represent scaling for comparison with baseline plasma focus devices that have been optimized in terms of electrode dimensions. It must also be emphasized that the scaling with I_{pinch} works well even when there are some variations in the actual device from L_0= 30 nH, V_0= 20 kV and c = 1.5. However there may be many other parameters which can change and could lead to a further enhancement of x-ray yield.

4. Conclusions

Numerical experiments carried out using the universal plasma focus laboratory facility based on the Lee model code gives reliable scaling laws for neutrons production and neon SXR yields for plasma focus machines. The scaling laws obtained:

For neutron yield:
Y_n= 3.2x10^{11} $I_{pinch}^{4.5}$; Y_n= 1.8x10^{10} $I_{peak}^{3.8}$; I_{peak} (0.3 to 5.7), I_{pinch} (0.2 to 2.4) in MA.
Y_n~$E_0^{2.0}$ at tens of kJ to Y_n~$E_0^{0.84}$ at MJ level (up to 25MJ).

For neon soft x-rays:
Y_{sxr}= 8.3x10^3 $I_{pinch}^{3.6;}$ Y_{sxr}= 6x10^2 $I_{peak}^{3.2}$; I_{peak} (0.1 to 2.4), I_{pinch} (0.07 to1.3) in MA.
Y_{sxr}~$E_0^{1.6}$ (kJ range) to Y_{sxr}~$E_0^{0.8}$ (towards MJ).

These laws provide useful references and facilitate the understanding of present plasma focus machines. More importantly, these scaling laws are also useful for design considerations of new plasma focus machines particularly if they are intended to operate as optimized neutron or neon SXR sources. More recently, the scaling of Y_n versus E_0 as shown above has been placed in the context of a global scaling law [38] with the inclusion of available experimental data. From that analysis, the cause of scaling deterioration for neutron yield versus energy as shown in Figure 2 (which has also been given the misnomer 'neutron saturation') has been uncovered as due to a current scaling deterioration caused by an almost constant axial phase 'dynamic resistance' interacting with a reducing bank impedance as energy storage is increased at essentially constant voltage. Solutions suggested include the use

of ultra-high voltages and circuit enhancement techniques such as current-steps [39,40]. It is suggested here that the deterioration of soft x-ray yield with storage energy as shown in Figure 5 could also be ascribed to the same axial phase 'dynamic resistance' effect as described in that reference [38].

5. Acknowledgement

The authors acknowledge the contributions of Paul Lee and Rajdeep Singh Rawat to various parts of this paper.

REFERENCES

[1] S. Lee, "Twelve years of UNU/ICTP PFF-A review," IC/98/231 Abdus Salam ICTP, Miramare, Trieste, pp. 5–34, ICTP Open Access Archive, 1998, http://eprints.ictp.it/31/.

[2] Y. Kato and S. H. Be, Applied Physics Letters, No. 48, pp. 686, 1986

[3] E. P. Bogolyubov, V. D. Bochkov, V. A. Veretennikov, L. T. Vekhoreva, V. A. Gribkov, A. V. Dubrovskii, P. Ivanov Yu, A. I. Isakov, O. N. Krokhin, P. Lee, S. Lee, V. Ya Nikulin, A. Serban, P. V. Silin, X. Feng, and G. X. Zhang, "A powerful soft x-ray source for x-ray lithography based on plasma focusing," Physica Scripta, Vol. 57, pp. 488–494, 1998.

[4] S. Lee, P. Lee, G. Zhang, X. Feng, V. A. Gribkov, L. Mahe, A. Serban, and T. K. S. Wong, IEEE Transactions on Plasma Science, No. 26, pp. 1119, 1998.

[5] N. V. Filippov, T. I. Filippova, M. A. Karakin, V. I. Krauz, V. P. Tykshaev, V. P. Vinogradov, Y. P. Bakulin, V. V. Timofeev, V. F. Zinchenko, J. R. Brzosko, and J. S. Brzosko, IEEE Transactions on Plasma Science, No. 24, pp. 1215–1223, 1996.

[6] N. V. Filippov, T. I. Filippova, I. V. Khutoretskaia, V. V. Mialton, and V. P. Vinogradov, "Megajoule scale plasma focus as efficient X-ray source," Physics Letters A, Vol. 211, No. 3, pp. 168–171, 1996.

[7] Institute for Plasma Focus Studies, http://www.plasmafocus.net.

[8] Internet Workshop on Plasma Focus Numerical Experiments (IPFS-IBC1), April 14–May 19, 2008, http://www.plasmafocus.net/IPFS/Papers/IWPCAkeynote2ResultsofInternet-basedWorkshop.doc.

[9] S. Lee, "Radiative dense plasma focus computation package: RADPF," http://www.intimal.edu.my/school/fas/UFLF/File1RADPF.htm, http://www.plasmafocus.net/IPFS/modelpackage/File1RADPF.htm.

[10] S. Lee, R. S. Rawat, P. Lee, and S. H. Saw, "Soft x-ray yield from NX2 plasma focus-correlation with plasma pinch parameters," (to be published).

[11] S. Lee and S. H. Saw, "Neutron scaling laws from numerical experiments," Journal of Fusion Energy, No. 27, pp. 292–295, 2008.

[12] S. Lee, "Current and neutron scaling for megajoule plasma focus machine," Plasma Physics and Controlled Fusion, No. 50, 105005, (14pp), 2008.

[13] S. Lee, S. H. Saw, P. C. K. Lee, R. S. Rawat, and H. Schmidt, "Computing plasma focus pinch current from total current measurement," Applied Physics Letters, No. 92, 111501, 2008.

[14] S. Lee and S. H. Saw, "Pinch current limitation effect in plasma focus," Applied Physics Letters, No. 92, 021503, 2008.

[15] S. Lee, P. Lee, S. H. Saw, and Rawat R S, "Numerical experiments on plasma focus pinch current limitation," Plasma Physics and Controlled Fusion, No. 50, 065012 (8pp), 2008.

[16] S. Lee, "Plasma focus model yielding trajectory and structure" in Radiations in Plasmas, B. McNamara, ed., World Scientific Publishing Co, Singapore, ISBN 9971-966-37-9, Vol. 2, pp. 978–987, 1984.

[17] S. Lee, *et al*, "A simple facility for the teaching of plasma dynamics and plasma nuclear fusion," American Journal of Physics, No. 56, pp. 62–68, 1988.

[18] T. Y. Tou, S. Lee, and K. H. Kwek, "Non perturbing plasma focus measurements in the run-down phase," IEEE Transactions on Plasma Science, No. 17, pp. 311–315, 1989.

[19] S. Lee, "A sequential plasma focus," IEEE Transactions on Plasma Science, Vol. 19, No. 12, pp. 912–919, 1991.

[20] J. B. Ali, "Development and studies of a small Plasma focus," PhD thesis, Universiti Teknologi Malaysia, Malaysia, 1990.

[21] D. E. Potter, "The formation of high density z-pinches," Nuclear Fusion, Vol. 18, pp. 813–823, 1978.

[22] S. Lee and A. Serban, "Dimensions and lifetime of the plasma focus pinch," IEEE Transactions on Plasma Science, Vol. 24, No. 3, pp. 1101–1105, 1996.

[23] M. H. Liu, "Soft X-rays from compact plasma focus," PhD thesis, NIE, Nanyang Technological University, Singapore, 2006, ICTP Open Access Archive: http://eprints.ictp.it/327/.

[24] S. Bing, "Plasma dynamics and x-ray emission of the plasma focus," PhD Thesis, NIE, Nanyang Technological University, Singapore, 2000, ICTP Open Access Archive: http://eprints.ictp.it/99/.

[25] A. Serban and S. Lee, "Experiments on speed-enhanced neutron yield from a small plasma focus," Journal of Plasma Physics, Vol. 60, Part 1, pp. 3–15, 1998.

[26] M. H. Liu, X. P. Feng, S. V. Springham, and S. Lee, "Soft x-ray measurement in a small plasma focus operated in neon," IEEE Transactions on Plasma Science, No. 26, pp. 135–140, 1998.

[27] D. Wong, P. Lee, T. Zhang, A. Patran, T. L. Tan, R. S. Rawat, and S. Lee, "An improved radiative plasma focus model calibrated for neon-filled NX2 using a tapered anode," Plasma Sources Science and Technology, No. 16, pp. 116–123, 2007.

[28] S. Lee, 2000–2007, http://ckplee.myplace.nie.edu.sg/plas-

maphysics/.

[29] S. Lee, 2005, ICTP Open Access Archive: http://eprints.ictp.it/85/.

[30] M. A. Mohammadi, S. Sobhanian, C. S. Wong, S. Lee, P. Lee, and R. S. Rawat, "The effect of anode shape on neon soft x-ray emissions and current sheath configuration in plasma focus device," Journal of Physics D: Applied Physics, 42, 2009, 045203 (10pp).

[31] Springham S V, Lee S and Rafique M S, "Correlated deuteron energy spectra and neutron yield for a 3 kJ plasma focus," Plasma Physics Controlled Fusion, Vol. 42, pp. 1023–1032, 2000.

[32] S. Lee, P. Lee, G. Zhang, X. Feng, V. A. Gribkov, M. Liu, A. Serban, and T. Wong "High rep rate high performance plasma focus as a powerful radiation source," IEEE Transactions on Plasma Science, Vol. 26, No. 4, pp. 1119–1126, 1998.

[33] V. Siahpoush, M. A. Tafreshi, S. Sobhanian, and S. Khorram, "Adaptation of Sing Lee's model to the Filippov type plasma focus geometry," Plasma Physics Controlled Fusion, No. 47, pp. 1065–1072, 2005.

[34] V. A. Gribkov, A. Banaszak, B. Bienkowska, A. V. Dubrovsky, I. Ivanova-Stanik, L. Jakubowski, L. Karpinski, R. A. Miklaszewski, M. Paduch, M. J. Sadowski, M. Scholz, A. Szydlowski, and K. Tomaszewski, "Plasma dynamics in the PF-1000 device under full-scale energy storage: II, Fast electron and ion characteristics versus neutron emission parameters and gun optimization perspectives," Journal of Physics D: Applied Physics, No. 40, pp. 3592–3607, 2007.

[35] J. D. Huba, Plasma Formulary page, No. 44, 2006.

[36] S. Lee, S. H. Saw, P. Lee, and R. S. Rawat, "Numerical experiments on plasma focus neon soft x-ray scaling," Plasma Physics and Controlled Fusion, No. 51, 105013 (8pp), 2009,
Available at http://stacks.iop.org/PPCF/51/105013.

[37] D. C. Gates, Proceedings of the 2nd International Conference on Energy Storage, Compression and Switching, Venice, No. 2, pp. 3239, Plenum Press, New York, 1983.

[38] S. Lee, "Neutron yield saturation in plasma focus-A fundamental cause," Applied Physics Letters, No. 95, 151503, First online 15 October 2009.

[39] S. H. Saw, "Experimental studies of a current-stepped pinch," PhD Thesis Universiti Malaya, Malaysia, 1991.

[40] S. Lee, "A current-stepping technique to enhance pinch compression," Journal of Physics D: Applied Physics, No. 17, pp. 733–739, 1984.

Energy and Power Engineering, 2010, 1-72
Published Online February 2010 in SciRes (http://www.scirp.org/journal/epe).

TABLE OF CONTENTS

Volume 2, Number 1, February 2010

ISSN: 1949-243X
977194924300X 03